Dissertation
submitted to the
Combined Faculties for the Natural Sciences and for Mathematics
of the Ruperto-Carola University of Heidelberg, Germany
for the degree of
Doctor of Natural Sciences

put forward by
Diplom-Physiker Robert Fleischhaker
born in Limburg an der Lahn, Germany
Oral examination: October 28th, 2009

Light propagation in dense and chiral media

Referees: Priv.-Doz. Dr. J. Evers

Prof. Dr. M. Weidemüller

Zusammenfassung

Die elektromagnetischen Eigenschaften von Licht werden in der Quantenoptik meist auf die elektrische Komponente reduziert. Ein Medium, das sowohl mit der elektrischen als auch mit der magnetischen Komponente wechselwirkt, wäre jedoch aus technologischer Sicht sehr interessant. Ein vor kurzem vorgeschlagener Ansatz, um die magnetische Antwort zu verstärken, basiert auf hoher Dichte sowie induzierter Chiralität. Eine Kombination von beidem ist jedoch experimentell zur Zeit nicht umsetzbar.

Diese Arbeit untersucht Lichtpropagation in dichten und in chiralen Medien, wobei beide Konzepte getrennt und in experimentell zugänglichen Parameterbereichen behandelt werden. Im Einzelnen analysieren wir ein sog. Closed-Loop System, demonstrieren ein Schema zur Kontrolle der Gruppengeschwindigkeit im UV-Bereich, zeigen, wie parametrische Prozesse in der Lichtpropagation verwendet werden können und erläutern den Einfluss hoher Gasdichte auf einen verlangsamten Lichtpuls. Wir leiten die Wellengleichung für Medien mit induzierter Chiralität her und lösen sie auf Basis der allgemeinen Mediumsantwort. In einem konkretes Beispiel verwenden wir die erarbeiteten Konzepte, um Lichtpropagation mit chiraler Wechselwirkung zu untersuchen. Dabei stellen wir fest, dass ein chirales Medium die optimale Umsetzung eines Closed-Loop Phasenkontrollschemas ermöglicht und so die Dynamik eines verlangsamten Lichtpulses während der Propagation kontrolliert werden kann. Außerdem zeigen unsere Ergebnisse, dass bereits mit heutigen experimentellen Methoden Parameter erreichbar sind, bei denen die magnetische Komponente des Probefelds relevant wird.

Abstract

In quantum optics, the electromagnetic character of light is mostly reduced to its electric component. Technologically interesting, a medium interacting with both the electric and magnetic component has recently been proposed. But the suggested combination of high density and induced chirality to enhance the magnetic response is beyond the limits of current experiments.

This thesis studies light propagation in dense and chiral media, assessing both concepts separately and in more accessible parameter ranges. In this context, we analyze a so-called closed-loop system, demonstrate a scheme for group velocity control in the UV range, show how to utilize parametric processes for light propagation, and explain effects due to high density on a slow light pulse. We derive the wave equation for media with induced chirality and solve it on the level of general medium response coefficients. This is then followed by a specific example, in which the developed concepts are applied to study light propagation with chiral interactions. We find that a chiral medium is an ideal implementation of a closed-loop-phase control scheme and show that the dynamics of a slow light pulse can be controlled throughout propagation time. Furthermore, our results demonstrate that the magnetic probe field component can become relevant for parameters achievable in current experiments.

Within the framework of this thesis, the following articles were published in refereed journals:

- M. Mahmoudi, R. Fleischhaker, M. Sahrai, and J. Evers,
  Group velocity control in the ultraviolet domain via interacting dark-state resonances,
  J. Phys. B: At. Mol. Opt. Phys. **41**, 025504 (2008).
- R. Fleischhaker and J. Evers,
  Nonlinear effects in pulse propagation through Doppler-broadened closed-loop atomic media,
  Phys. Rev. A. **77**, 043805 (2008).
- R. Fleischhaker and J. Evers,
  Four-wave mixing enhanced white-light cavity,
  Phys Rev. A **78**, 051802(R) (2008).

Articles submitted for publication in refereed journals:

- R. Fleischhaker and J. Evers,
  Light propagation in chiral media,
  arXiv:0906.5301 [quant-ph] (2009),
  submitted to Phys. Rev. A.

Articles in preparation:

- R. Fleischhaker, T. N. Dey, and J. Evers,
  Phase modulation induced by cooperative effects in electromagnetically induced transparency,
  arXiv:0902.0752 [quant-ph] (2009).
- R. Fleischhaker and J. Evers,
  Maxwell-Bloch equations in chiral media: A numerical integration scheme,
  in preparation.

Contents

Introduction

Since the work of J. C. Maxwell [1] and H. R. Hertz [2] we know that light is a form of electromagnetic radiation. As such it can be described as an electromagnetic wave composed of oscillating electric and magnetic field components. According to Maxwell's equations [3], these two components continually generate each other while the electromagnetic wave propagates. A change of the electric field induces a magnetic field, and in the same way a change of the magnetic field induces an electric field. Hence, both field components are an integral part of the electromagnetic wave. Also the relativistic perspective shows that electric and magnetic fields are intimately connected. Lorentz invariance of Maxwell's equations guarantees the freedom to choose any inertial frame of reference to describe a physical system. Changing the frame of reference however, can transform a purely electric or magnetic field into a mixture of both fields [3].

From the above considerations, we recognize that in the electromagnetic description of light, the electric and magnetic component play an equal role. Thus, at first sight, it is suprising that this is not the case in the description of light-matter interaction in quantum optics. Studying the corresponding literature shows that in the vast majority of quantum optical systems only the electric component is taken into account [4, 5]. A closer look reveals that in almost all cases such a simplified treatment is sufficient, because usually the magnetic field component couples much weaker to matter than the electric field component. This does not exclude the influence of static magnetic fields which leads to energy shifts due to the Zeeman effect and which is also used to magnetically trap atoms. However, it raises the question, whether quantum optical systems exist, in which both components of a probing electromagnetic wave couple to a medium simultaneously. And if such systems existed, what would be the differences or advantages compared to usual quantum optical systems? It turns out that such systems can indeed be realized and open up a new and exciting research area with an enormous potential both for fundamental questions and applications.

An early theoretical investigation was performed by V. G. Veselago [6]. He studied the electrodynamic properties of a medium characterized by a simultaneously negative electric and magnetic response. In such a medium both components of an electromagnetic wave interact with matter and Veselago concluded that there are no fundamental contradictions to this concept. Instead, he showed that such a medium would have remarkable properties unlike those of any known materials in nature. Based on his analysis, it was realized later that some properties would have immediate applications. For example, J. Pendy and others recently presented the idea to build a so-called superlens [7–10]. The image resolution of a standard lens is limited to distances of the order of half the wavelength. This is due to the fact that the sub-wavelength information is encoded in the evanescent wave modes which are damped away in conventional media and cannot contribute to the image. But in a medium as described by Veselago, evanescent waves are exponentially amplified instead [6]. As a consequence, the image resolution for a corresponding lens is in principle not limited by the wavelength. In general, the ability to influence both the electric and magnetic component, considerably extends the possibilities to control electromagnetic wave propagation. One can show that a change of both the electric permittivity ε and the magnetic permeability μ is equivalent to a coordinate transformation of the electromagnetic field configuration [11]. This equivalence can be used to design a medium which continuously guides the electromagnetic field in its propagation. For example, a configuration is possible in which the electromagnetic field is made to avoid a certain region of space, flowing around it, and returning to its original direction of propagation as if there had been no disturbance of the propagation at all. Fascinating applications such as a cloaking device making macroscopic objects invisible, have been suggested [11, 12].

That these concepts are not only of theoretical interest was first demonstrated in experiments with metamaterials [13–20]. These are artificially manufactured composites with a periodic lattice structure. The lattice constant is much smaller than the wavelength of the incident radiation and the structural features are designed to exhibit a capacitive and an inductive resonance which are close to each other. With this design, effectively homogeneous media with a simultaneous electric and magnetic response over a certain frequency range have been accomplished. A prime example is given by the realization of a negative refractive index. In benchmark experiments Veselago's prediction is tested that for a medium with $\varepsilon < 0$ and $\mu < 0$, Snell's law still holds, but for an index of refraction which is negative, $n = -\sqrt{\varepsilon\mu} < 0$. Compared to a medium with a positive refractive index, a ray of light is bend in the opposite direction when refracted at an interface with vacuum which was impressively confirmed in planar setups with metamaterials [15, 20].

Over the past years metamaterials of different design have proved the idea to realize a medium with a simultaneous electric and magnetic response over a wide range of frequencies. The success of this concept lead to the suggestion to implement similar schemes with atomic systems [21, 22]. Compared to metamaterials, these have some intrinsic advantages. For example, they are an effectively homogeneous medium for wavelength in the optical and below and coherent preparation techniques developed in quantum optics could be applied to minimize losses which are inevitable in metamaterials. However, a problem in atomic systems is the usually weak magnetic response. This can already be seen in a classical estimate of the Lorentz electromagnetic force exerted on a charged particle. For a bound electron exposed to an electromagnetic wave in vacuum, the part of the Lorentz force due to the magnetic component is weaker by about a factor of the fine structure constant

α than the part due to the electric component [3]. In the same way, a typical magnetic dipole coupling is weaker by a factor of about α than a typical electric dipole coupling. Consequently, the magnetic permeability is suppressed by a factor of α^2 compared to the electric susceptibility, such that the magnetic response becomes negligibly small. Therefore, a key challenge in realizing atomic media with a coupling to both components of light, lies in enhancing the magnetic response. Mainly, two suggestions regarding this issue have been made.

One possibility is to use an unusually high atomic density as electric and magnetic response are directly proportional to the number of atoms per unit volume. Current proposals to implement such a scheme rely on a rather simple model for dense atomic gases [21, 22]. In contrast, dense gas physics is an interesting but highly nontrivial research area of its own. From simple Doppler and pressure broadening [25,26] in hot atomic vapors to more involved dense gas effects such as dipole-dipole interaction, quantum statistical effects [27], sub- and superradiance [28], multiple scattering of photons and radiation trapping [29], a variety of different phenomena can be important. Therefore, it is not clear whether these proposals are realizable.

A qualitatively different approach to enhance the magnetic response is based on the idea of using a chiral medium [30–33]. Effects due to chirality are most familiar from the optical activity of chiral molecules [34] which have the ability to rotate the polarization direction of linearly polarized light. Indeed, one possible mechanism underlying optical activity is quite indicative for the concept of enhancing the magnetic response with chirality [35]. In a chiral molecule the asymmetric electron distribution can permit a single optical transition to be both electric and magnetic dipole allowed. On the one hand, due to the fixed spatial orientation of the corresponding electric and magnetic dipole moments, this results in a different interaction energy with left- and right-circularly polarized light. On the other hand, this enhances the magnetic response by a factor of α. Due to the coupling of both field components to the same transition, the electric component can induce a magnetic dipole moment and vice versa, leading to a cross coupling. Because the magnetic response due to a cross coupling induced dipole moment is suppressed only by a factor of α, compared to α^2 for the direct magnetic response, this results in an effective enhancement.

In contrast to chiral molecules, in atoms the symmetry properties usually prevent optical transitions to be both electric and magnetic dipole allowed. Here, a cross-coupling has to be induced which can be achieved by a closed-loop system. In these systems the laser-driven transitions form a closed interaction loop such that photon emission and absorption can take place in a cycle [36, 37]. Furthermore, quantum mechanical interference of different possible transition pathways can render the system phase dependent which can provide an additional control parameter. To take advantage of this scheme, the idea is to form a closed interaction loop out of a magnetic and a separate, (nearly) degenerate electric dipole transition and additional transitions driven by auxiliary laser fields. The probe field should be resonant with both the electric and the magnetic dipole transition. In such a configuration, one probe field component can induce a dipole moment in the other probe field transition via the closed interaction loop. As a result, the desired cross coupling between the two probe field components arises [32, 38]. A magnetic dipole transition nearly degenerate to an optical electric dipole transition is a demanding requirement. Quantum mechanical selection rules imply that magnetic dipole transitions can only occur between states of the same angular momentum whereas electric dipole transitions connect states of different angular momentum [39]. As a consequence, magnetic dipole transitions are mostly found in a much lower frequency range [40]. Nevertheless, atomic species with magnetic dipole transitions in the optical domain do exist. For example, noble gases or rare earth elements with a large angular momentum ground state can exhibit a strong spin-orbit splitting such that the transition frequency between states of the same angular momentum is lifted into the optical domain.

Present proposals which aim to realize negative refractive index media, rely on a closed-loop configuration to induce chirality [32, 33]. Based on the requirements for negative refraction, they assume parameters which are currently not realistic. Thus, it is not supprising that no experiments have been performed so far which implement such a scheme. Here, we follow a different approach and study the aspects of chirality and high density starting from a currently accessible parameter range. On the one hand, this may lead to the goal of negative refraction and from a broader perspective, addresses the question whether effects due to the magnetic field component are important in quantum optics. But on the other hand, we will show that chirality and high density are interesting in their own right.

In this thesis, we put forward a number of ideas and concepts related to light propagation in dense and chiral media. With respect to both dense media and chiral media, we aim to improve the understanding of physical processes at the level of current or near future experiments. We organize the analysis into different parts and address the relevant aspects step by step. Furthermore, all partial results are illustrated independently by potential applications.

In **Part I**, we deal with aspects accessible in a single atom picture. This implies that the spatial dependence of the fields is neglected or assumed homogeneous. More specifically, in **Chapter 1**, we study the response of a closed-loop system to a pulsed probe field. This is a necessary prerequisite for the analysis of chiral media because a closed interaction loop is at the heart of the mechanism that induces chirality. In the analysis, the closed interaction loop in combination with the finite frequency width of the probe pulse, gives rise to an explicit time dependence in the equations of motion. We use Floquet theory to calculate the different response coefficients. A physical interpretation of these coefficients in terms of scattering processes into the probe field mode makes it possible to identify the parts of the solution leading to a linear and nonlinear response. Analyzing the nonlinear response, we find that the system can exhibit a strong intensity-dependent refractive index with small absorption. This is the basis for applications such as beam focussing, pulse compression, and self-phase or cross-phase modulation.

In **Chapter 2**, we investigate a setup suitable for controlling the group velocity. We chose mercury as our model system, where the probe field transition is in the ultraviolet domain. This is motivated by the ultimate goal to replace standard optical elements that become harder to produce with increasing frequency. Indeed, a level scheme suitable for UV-lasing has been proposed in mercury, but due to its ladder structure it is not ideal for light propagation and concepts such as electromagnetically induced transparency are not directly applicable. Instead, we use an additional control field to induce so-called interacting dark state resonances that provide a high-contrast resonance structure in the dispersion. We find that this resonance structure alone leads to superluminal light propagation, albeit with absorption. When an additional incoherent field is applied to the probe field transition, the resonance structure can be altered such that sub- and superluminal light propagation as well as a negative group velocity can be achieved without absorption. We show that this result can be preserved under realistic conditions with Doppler averaging which makes the system suitable for applications like a controllable pulse delay line in the ultraviolet domain.

Based on the methods developed in the first part, it is possible to predict light propagation dynamics in atomic media. However, as soon as the spatial dependence of the applied fields starts to play a role, the single atom picture is not sufficient anymore and we have to take into account the propagation dynamics explicitly. This is the case in the setups we address in **Part II**. Here, we extend our theoretical description by using the Maxwell-Bloch equations. In this framework, it becomes considerably harder to obtain analytical solutions. Consequently, we employ a suitable algorithm (see **Appendix**) to integrate the equations of motion numerically. The combination of the numerical solution together with analytical considerations make it possible to gain physical insight also in these setups.

First, in **Chapter 3**, we analyze light propagation in a system where strong propagation dynamics can be expected. Naively one might think that using a non-standard level scheme beyond EIT only leads to strong absorption of the control fields. However, it turns out that an additional field is generated via a four-wave-mixing process as soon as the probe field is applied. We find that the newly generated field gives rise to scattering processes into the probe field mode via a closed interaction loop and thus changes the probe field response. We calculate an effective medium response including this dynamics by numerically propagating a continuous wave probe field for different detunings. Surprisingly, we find a relatively smooth and controllable result with a negative dispersion and slight gain for the probe field. As an application we propose to use such a medium to implement a so-called white-light cavity. Here, the negative dispersion is used in a phase-compensation mechanism that leads to a broader cavity resonance profile without decreasing the intensity buildup. We show that our medium fulfills the corresponding dispersion requirements and counterintuitively, the in-medium dynamics causes an additional enhancement of the cavity bandwidth.

Then, in **Chapter 4**, we study light propagation in a dense medium. In particular, we focus on an EIT setup and densities at the onset of cooperative effects. We derive an analytic solution for the propagation dynamics of a weak pulse and we find that the dipole-dipole interaction of neighboring atoms strongly modulates the phase of the pulse. We show that this phase modulation is distinctively different from the nonlinear self-phase modulation a strong field experiences in a medium with an intensity dependent index of refraction. It leads to a linear frequency chirp over the total extent of the pulse. In addition, we give an intuitive explanation of the underlying physical mechanism which causes the phase modulation. Analyzing the effects of using higher densities in EIT is important because it directly improves key quantities such as the group velocity reduction, the related spatial compression of a pulse, and the time-delay bandwidth product characterizing slow light systems. Furthermore, understanding the influence of dipole-dipole interaction on light propagation dynamics is a first step towards experiments in the regime of even higher density as needed, for example, in negative refractive index media.

In **Part III**, we address light propagation in chiral media. In **Chapter 5**, we first define a chiral medium by the electrodynamic response coefficients. Then, on the basis of the macroscopic Maxwell equations, we derive the wave equation for a probe field propagating in a chiral medium. We solve this equation in Fourier space using the slowly-varying envelope approximation. The solution is expressed in terms of the general medium response coefficients and elucidates the different influences of the direct and chiral response on the propagation dynamics. At the end of the chapter, we discuss the conditions necessary to implement a chiral atomic medium.

In **Chapter 6**, we turn to a specific level scheme suitable for implementing light propagation in a chiral system. On the one hand, this serves as an example to apply the wave equation derived in the fifth chapter. On the other hand, it allows us to demonstrate how the different concepts we discussed separately in the other chapters work together in a single system. The key ingredient of the system is to employ a closed interaction loop containing both the magnetic and the electric probe field transition. As expected, the medium response becomes phase dependent and a chiral cross coupling arises. To investigate the actual propagation dynamics, we derive analytic solutions for the different medium response coefficients. We find that the magnetic response already becomes relevant at low densities. We show that already in the dilute gas regime, the propagation dynamics of a slow light pulse can be controlled throughout propagation time by the closed-loop phase. Furthermore, the closed-loop phase depends only on the relative phase of the control fields. It is independent of the probe field phase which one might not be able to control in applications. Thus, the system constitutes an ideal implementation of a closed-loop-phase control scheme and demonstrates that the magnetic probe field component can be of significant influence in a parameter regime accessible to current experiments.

Part I

Coherent control in a dilute atomic vapor

Chapter 1

Nonlinear effects in pulse propagation through closed-loop atomic media

Nonlinear effects in pulse propagation through a medium consisting of four-level double-Λ-type systems are studied theoretically. We apply three continuous-wave driving fields and a pulsed probe field such that they form a closed interaction loop. Due to the closed loop and the finite frequency width of the probe pulses the multiphoton resonance condition cannot be fulfilled, such that a time-dependent analysis is required. By identifying the different underlying physical processes we determine the parts of the solution relevant to calculate the linear and nonlinear response of the system. We find that the system can exhibit a strong intensity dependent refractive index with small absorption over a range of several natural linewidths. For a realistic example we include Doppler and pressure broadening and calculate the nonlinear selfphase modulation in a gas cell with Sodium vapor and Argon buffer gas. We find that a selfphase modulation of π is achieved after a propagation of few centimeters through the medium while the absorption and pulse shape distortion in the corresponding spectral range is small.

1.1 Introduction

A main interest in laser driven atomic media is the study of their coherence properties. Coherence effects like electromagnetically induced transparency (EIT) [23,24], coherent population trapping [41,42], lasing without inversion [43], and others [4,44] are examples where the optical properties of an atomic medium are influenced with coherent fields. The interference of different excitation channels is the main underlying principle here. A particular class of systems in which quantum mechanical interference plays a major role are the so-called closed-loop systems [36,37,45–55].

In these systems the laser-driven transitions form a closed interaction loop such that photon emission and absorption can take place in a cycle. This leads to interference of indistinguishable transition pathways between different states. One consequence of this is that it can render the system dependent on the relative phase of the driving fields. At the same time, however, the investigation of closed-loop systems is made difficult by the fact that the interfering pathways typically prevent the system from reaching a time-independent steady state. Such a stationary state in general is only reached when the so-called multiphoton resonance condition on the detunings of the different driving field is fulfilled, which was therefore assumed in most previous studies. For general laser field detunings, a time-dependent analysis is mandatory [46, 52].

Laser driven atomic media are also known to exhibit significant nonlinear optical properties [26, 46–50, 53–67]. A particular example is the occurrence of an intensity dependent refractive index, with applications such as beam focussing, pulse compression, selfphase- or cross-phase modulation or optical switching [60–67]. Here, the connection to coherence properties is the following. While an atomic resonance can greatly enhance nonlinear effects in atomic media, the accompanying linear absorption of the same resonance typically renders the medium opaque to the probe field. This can be overcome by tailoring the response via coherence and interference effects. An advantageous situation arises, e.g., if the linear absorption vanishes due to destructive interference while the nonlinear effect is enhanced by constructive interference.

Motivated by this, we investigate nonlinear effects in pulse propagation through a closed-loop atomic medium. In particular, we study a four-level atomic system where the four dipole-allowed transitions form a double-Λ type scheme (see Fig. 1.1). Three of the fields are assumed to be continuous-wave coupling laser fields, while the fourth field is a pulsed probe field. We use a time-dependent analysis, as the multiphoton resonance condition cannot be applied due to the finite frequency spectrum of the probe pulses. The medium is modelled as a dilute gas vapor including Doppler and pressure broadening and an additional buffer gas using realistic parameters. Our main observable is the nonlinear index of refraction of the medium. We find that our system exhibits a high nonlinear index of refraction with small linear and nonlinear absorption over a spectral range of several natural linewidths. In this spectral region of interest, group velocity dispersion is low, such that pulse shape distortions are minimized. For Sodium atoms with Argon buffer gas, we obtain a nonlinear selfphase modulation of π after 6.4 cm of passage through the medium.

This chapter is organized as follows. In the following Sec. 1.2.1 we present our model. In Sec. 1.2.3, we solve for the time-dependent long-time limit arising from the closed interaction loop in the form of a series. The interpretation of the series coefficients with respect to their physical meaning (Sec. 1.2.4) will enable us to identify the quantities necessary to calculate the linear and nonlinear susceptibility for the probe field of our system (Sec. 1.2.5). Doppler and pressure broadening are discussed in Secs. 1.2.6 and 1.2.7. Our results are presented in Sec. 1.3, both with and without broadening. Finally, Sec. 1.4 discusses and summarizes our results.

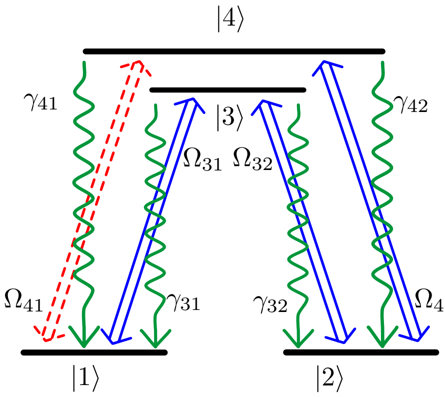

Figure 1.1: The four-level atomic system with the four dipole-allowed transitions forming a closed-loop double-Λ type scheme. Three transitions are driven by continuous-wave control fields indicated by the solid blue double arrows. The fourth transition couples to the pulsed probe field indicated by the dashed red double arrow. The coupling strengths are given by the Rabi frequencies Ω_{jk}. The spontaneous decays with rates γ_{jk} are denoted by the wiggly green lines ($j \in \{3,4\}$, $k \in \{1,2\}$).

1.2 Theoretical analysis

1.2.1 Hamiltonian

In this section we present the Hamiltonian for the four-level system and the interaction with the coupling fields in a suitable interaction picture. We write the field coupling to transition $|j\rangle \leftrightarrow |k\rangle$ ($j \in \{3,4\}$, $k \in \{1,2\}$) as

$$\boldsymbol{E}_{jk} = \frac{E_{jk}}{2}\left(\hat{\boldsymbol{e}}_{jk} e^{-i\omega_{jk}t} + \text{ c.c.}\right) , \tag{1.1}$$

with amplitude E_{jk}, unit polarization vector $\hat{\boldsymbol{e}}_{jk}$, and frequency ω_{jk}. For better readability we suppress the space-dependence of the fields. The Hamiltonian in dipole and rotating-wave approximation reads [4, 44]

$$H = \sum_{j=1}^{4} \hbar\omega_j A_{jj} - \sum_{j=3}^{4}\sum_{k=1}^{2} \frac{\hbar\Omega_{jk}}{2}\left\{e^{-i(\omega_{jk}t-\phi_{jk})} A_{jk} + \text{ H.c.}\right\} . \tag{1.2}$$

The energy of level $|j\rangle$ is denoted by $\hbar\omega_j$ and we have introduced Rabi frequencies $\Omega_{jk} = E_{jk}|\hat{\boldsymbol{e}}_{jk}\,\boldsymbol{d}_{jk}|/\hbar$ with $\boldsymbol{d}_{jk}$ being the dipole matrix element of transition $|j\rangle \leftrightarrow |k\rangle$ ($j \in \{3,4\}$, $k \in \{1,2\}$). The complex phase of the Rabi frequencies was included into the exponential function where $\phi_{jk} = \arg(\hat{\boldsymbol{e}}_{jk}\,\boldsymbol{d}_{jk})$. The atomic transition operator is defined as $A_{jk} = |j\rangle\langle k|$.

The canonical approach with a Hamiltonian of the sort we have just introduced would be to transform it into an interaction picture where the time dependence fully vanishes. Unfortunately, this is not possible in our case. Due to the closed interaction loop, in general a residual time dependence in the Hamiltonian remains. Physically, this means that we cannot expect the system to reach a true stationary state in the long time limit. The best we can do is to use a unitary transformation that gathers all the time dependence in a single exponential factor in front of the probe field Rabi frequency. In this interaction picture we obtain

$$\begin{aligned} H_I =& \hbar(\Delta_{32}-\Delta_{31})A_{22} - \hbar\Delta_{31}A_{33} + \hbar(\Delta_{32}-\Delta_{31}-\Delta_{42})A_{44} \\ & - \frac{\hbar}{2}\left(\Omega_{31}A_{31} + \Omega_{32}A_{32} + \Omega_{42}A_{42} + \Omega_{41}A_{41}e^{-i(\Delta t-\phi)} + \text{ H.c.}\right) , \end{aligned} \tag{1.3}$$

where the detunings are defined as $\Delta_{jk} = \omega_{jk} - (\omega_j - \omega_k)$. We have also defined the so-called multiphoton detuning and an equivalent combination of the dipole phases

$$\Delta = \Delta_{41} + \Delta_{32} - \Delta_{31} - \Delta_{42} , \tag{1.4a}$$

$$\phi = \phi_{41} + \phi_{32} - \phi_{31} - \phi_{42} . \tag{1.4b}$$

The multiphoton detuning is a typical quantity characterizing a system with a closed interaction loop. Its significance will become more apparent in Sec. 1.2.4.

1.2.2 Master equation

We now set up the master equation for the atomic density matrix ϱ. We include the unitary evolution due to the Hamiltonian in the interaction picture and relaxation dynamics due to spontaneous decay in Born-Markov approximation. The collision induced dynamics will be considered in Sec. 1.2.7. The unitary evolution is given by the Von-Neumann equation and the spontaneous decay can be written in Lindblad form [44]. The master equation in the interaction picture then reads

$$\partial_t \varrho^I = \frac{1}{i\hbar}\left[H_I, \varrho^I\right] - \sum_{j=3}^{4}\sum_{k=1}^{2}\frac{\gamma_{jk}}{2}\left\{\left[\varrho^I A_{jk}, A_{kj}\right] + \text{ H.c.}\right\} , \tag{1.5}$$

where ϱ^I is the density matrix in the interaction picture and γ_{jk} is the radiative decay rate of transition $|j\rangle \leftrightarrow |k\rangle$. For the further analysis we rewrite the master equation in a matrix-vector form. Because the trace of the density matrix is conserved we use the corresponding condition

$$\mathrm{Tr}\,\varrho^I = \sum_{j=1}^{4} \varrho^I_{jj} = 1 \tag{1.6}$$

to eliminate the diagonal element ϱ_{44}. Here, $\varrho^I_{jk} = \langle j|\varrho^I|k\rangle$. Introducing the vector $R = (\varrho^I_{11}, \varrho^I_{12}, \varrho^I_{13}, \dots, \varrho^I_{43})^T$ containing the remaining fifteen elements of the density matrix we find

$$\partial_t R + \Sigma = MR , \tag{1.7}$$

with an inhomogeneous part Σ that stems from the elimination of ϱ_{44} and a coefficient matrix M. Both Σ and M can be directly derived from the master Eq. (1.5) and contain the explicit time dependence arising from the time dependent Hamiltonian Eq. (1.3). The explicit form of M and Σ is given in the appendix.

1.2.3 Time-dependent solution

To treat the explicit time dependence of the equation of motion we first separate Σ and M into the time independent part and the explicitly time dependent part. For this, we define

$$\Sigma = \Sigma_0 + \Sigma_{-1}\Omega_{41}e^{i(\Delta t-\phi)} + \Sigma_1\Omega_{41}e^{-i(\Delta t-\phi)}\,, \tag{1.8a}$$

$$M = M_0 + M_{-1}\Omega_{41}e^{i(\Delta t-\phi)} + M_1\Omega_{41}e^{-i(\Delta t-\phi)}\,, \tag{1.8b}$$

with time-independent Σ_j and M_j ($j \in \{0, \pm 1\}$). We see that under the condition $\Delta = 0$ the explicit time dependence vanishes. This is the so-called multiphoton resonance condition. For fixed coupling field frequencies this condition can only be fulfilled for a single probe field detuning Δ_{41}. But we want to investigate probe fields consisting of pulses with finite temporal length, which due to the Fourier relations implies that a whole spectrum of probe field frequencies interacts with the medium at the same time. Thus, we cannot assume the multiphoton resonance condition to be fulfilled [52]. Instead, we have to solve Eq. (1.7) including the explicit time dependence. To do so, we expand R as a power series in Ω_{41},

$$R = \sum_{n=0}^{\infty} R_n \Omega_{41}^n\,. \tag{1.9}$$

If we assume that the probe field strength is small compared to the control fields this series will converge. Inserting Eqs. (1.8) and (1.9) in Eq. (1.7), we can derive equations of motion for the individual coefficients R_n. In order $\mathcal{O}[\Omega_{41}^n]$ we find

$$\begin{aligned}\partial_t R_n = & M_0 R_n \\ & + \delta_{n,1}\left(\Sigma_{-1}e^{i(\Delta t-\phi)} + \Sigma_1 e^{-i(\Delta t-\phi)}\right) \\ & + \left(M_{-1}e^{i(\Delta t-\phi)} + M_1 e^{-i(\Delta t-\phi)}\right) R_{n-1}\,.\end{aligned} \tag{1.10}$$

This is an equation for R_n where the coefficient matrix M_0 is time independent and only the inhomogeneous part is time dependent. This time dependence is twofold, first again explicitly because of the exponential functions and second because of the dependence on R_{n-1}. Thus, we make an ansatz for the solution and write R_n in a Fourier series,

$$R_n = \sum_{m=-\infty}^{\infty} R_n^{(m)} e^{-im(\Delta t-\phi)}\,. \tag{1.11}$$

Projecting on the Fourier basis functions we derive a hierarchy of time independent equations for the coefficients $R_n^{(m)}$. Up to order $\mathcal{O}[\Omega_{41}^3]$ we find

$$R_0^{(0)} = M_0^{-1}\Sigma_0\,, \tag{1.12a}$$

$$R_1^{(\pm1)} = (M_0 \pm i\Delta\mathbb{1})^{-1}\left(\Sigma_{\pm1} - M_{\pm1}R_0^{(0)}\right)\,, \tag{1.12b}$$

$$R_2^{(0)} = -M_0^{-1}\left(M_{-1}R_1^{(1)} + M_1R_1^{(-1)}\right)\,, \tag{1.12c}$$

$$R_2^{(\pm2)} = -\left(M_0 \pm 2i\Delta\mathbb{1}\right)^{-1} M_{\pm1}R_1^{(\pm1)}\,, \tag{1.12d}$$

$$R_3^{(\pm1)} = -\left(M_0 \pm i\Delta\mathbb{1}\right)^{-1}\left(M_{\pm1}R_2^{(0)} + M_{\mp1}R_2^{(\pm2)}\right)\,, \tag{1.12e}$$

$$R_3^{(\pm3)} = -\left(M_0 \pm 3i\Delta\mathbb{1}\right)^{-1} M_{\pm1}R_2^{(\pm2)}\,, \tag{1.12f}$$

where $\mathbb{1}$ is the unit matrix and all other $R_n^{(m)}$ up to this order vanish. In general we find that

$$R = \sum_{n=0}^{\infty}\sum_{\substack{m=-n,\\ -n+2,\ldots}}^{n} R_n^{(m)}\,\Omega_{41}^n\,e^{-im(\Delta t-\phi)}\,. \tag{1.13}$$

Since Fourier coefficients $R_n^{(m)}$ in Eq. (1.12) only depend on Fourier coefficients $R_{n-1}^{(m)}$ of the next lower order, the full solution can be calculated recursively.

1.2.4 Physical interpretation

To physically interpret the meaning of the different coefficients we study the influence of the different parts of the solution on the probe field. First, we write down the expansion series for the relevant probe field coherence in the Schrödinger picture ϱ_{41} using the explicit transformation relation connecting the Schrödinger picture with our interaction picture. We find

$$\varrho_{41} = \varrho_{41}^I\,e^{-i(\omega_{41}t-\phi_{41})}\,e^{i(\Delta t-\phi)}. \tag{1.14}$$

With ϱ_{41}^I given as component of the solution for R we find

$$\varrho_{41} = \sum_{n=0}^{\infty}\sum_{\substack{m=-n,\\ -n+2,\ldots}}^{n}\left[R_n^{(m)}\right]_{13}\Omega_{41}^n e^{-i[\omega_{41}+(m-1)\Delta]t}\,e^{i[\phi_{41}+(m-1)\phi]}\,, \tag{1.15}$$

where $[R_n^{(m)}]_{13}$ refers to the thirteenth component of vector $R_n^{(m)}$. Thus, coefficient $[R_n^{(m)}]_{13}$ gives a contribution at the probe field frequency ω_{41} plus a frequency shift of $(m-1)\Delta$. The corresponding physical process can be identified as follows. A combination of dipole phases $\phi = \phi_{41} - \phi_{42} + \phi_{32} - \phi_{31}$ indicates a full evolution through a loop which extends from state $|1\rangle$ to $|4\rangle$ and via $|2\rangle$ and $|3\rangle$ back to state $|1\rangle$. The transition direction is given by the sign of the corresponding dipole phase. The evolution around the interaction loop is also the physical reason for the frequency shift Δ of such a process. Altogether, $[R_n^{(m)}]_{13}$ represents a process with $m-1$ loop cycles where the sign of $m-1$ defines the direction, clockwise for positive or counter-clockwise for negative sign. The remaining of the n probe transitions can be interpreted as direct transitions.

1.2.5 Linear and nonlinear susceptibility

With the above interpretation we can easily identify the parts of the solution leading to the linear and nonlinear susceptibility in the probe field. Because both contributions should oscillate at the probe field frequency we see that $m = 1$ must be fulfilled in Eq. (1.15). The order of Ω_{41} enables one to identify

$$\chi^{(1)}(\omega_{41}) \propto \left[R_1^{(1)}\right]_{13} \quad \text{at} \quad \mathcal{O}\left[\Omega_{41}^1\right] \; , \tag{1.16a}$$

$$\chi^{(3)}(\omega_{41}) \propto \left[R_3^{(1)}\right]_{13} \quad \text{at} \quad \mathcal{O}\left[\Omega_{41}^3\right] \; . \tag{1.16b}$$

There is no second order contribution to the susceptibility as it should be for an isotropic medium [26]. By comparing the microscopically calculated value for the polarization [4, 44]

$$\boldsymbol{P}_{41} = N\left(\boldsymbol{d}_{14}\varrho_{41} + \text{ c.c.}\right) \; , \tag{1.17}$$

with the definition of the susceptibility [26]

$$\boldsymbol{P}_{41} = \varepsilon_0 \frac{E_{41}}{2}\left(\chi^{(1)} + \frac{3}{4}E_{41}^2\chi^{(3)}\right)\hat{\boldsymbol{e}}_{41}e^{-i\omega_{41}t} + \text{ c.c.} \, , \tag{1.18}$$

we find

$$\chi^{(1)}(\omega_{41}) = \frac{3}{8\pi^2}\lambda_{41}^3 N\gamma_{41}\left[R_1^{(1)}\right]_{13} \, , \tag{1.19}$$

$$\frac{3}{4}E_{41}^2\chi^{(3)}(\omega_{41}) = \frac{3}{8\pi^2}\lambda_{41}^3 N\gamma_{41}\Omega_{41}^2\left[R_3^{(1)}\right]_{13} \, , \tag{1.20}$$

with ε_0 being the permittivity of free space, λ_{41} the wave length of the probe field transition, and N the density of atoms in the gas.

We remark that $\chi^{(3)}(\omega_{41}) = \chi^{(3)}(\omega = \omega_{41} - \omega_{41} + \omega_{41})$ is the lowest order nonlinear contribution at the probe field frequency. It leads to an intensity dependent refractive index that also depends on ω_{41} and can be different for each respective frequency of the probe pulse spectrum. This is not the case for other contributions to $\chi^{(3)}$. For example, $[R_0^{(0)}]_{13}$ oscillates at the frequency $\omega = \omega_{41} - \Delta$ and leads to a contribution $\chi^{(3)}(\omega = \omega_{31} - \omega_{32} + \omega_{42})$ (four-wave mixing). Here, the resulting frequency is independent of ω_{41}. Nevertheless, in principle those processes can influence the result for the linear and third-order susceptibility at certain probe field frequencies. For example, light can be scattered into the probe field mode via different processes. Whether this or similar contributions change the probe pulse depends on the pulse's frequency width compared to the multiphoton detuning Δ and more generally also on the propagation direction of the probe field relative to the control fields. A definite answer to these questions requires an analysis of the full pulse propagation dynamics through a medium which we will not turn to until part II.

1.2.6 Doppler broadening

A typical experimental setup to investigate the coherence properties of a laser driven atomic gas would be a gas cell with a dilute alkali-atom vapor. For a dilute atomic gas theoretical predictions for the linear and nonlinear susceptibility can be made on the basis of a single atom analysis. This greatly facilitates the theoretical analysis. However, in a dilute gas at room temperature or above the atoms move at velocities where the frequency shift due to Doppler effect cannot be neglected compared to the natural line width given by the radiative decay rate γ. To calculate the Doppler effect for a single field, we assume a Maxwell-Boltzmann velocity distribution in laser propagation direction with a most probable velocity given by [25]

$$v_m = \sqrt{\frac{2k_BT}{m}} \tag{1.21}$$

with k_B the Boltzmann constant, T the temperature, and m the mass of the atom. The non-relativistic Doppler frequency shift is given by

$$\omega_{\text{eff}} = \omega\left(1 - \frac{v}{c}\right), \tag{1.22}$$

where ω_{eff} is the shifted frequency seen by the moving atom, ω is the lab frame laser frequency, v is the velocity of the atom in laser propagation direction, and c is the speed of light. The Doppler shift effectively leads to an additional detuning Δ_{Dop} with a Gaussian distribution [25]

$$f(\Delta_{\text{Dop}})\, d\Delta_{\text{Dop}} = \frac{1}{\sqrt{\pi} k v_m}\, e^{-\left(\frac{\Delta_{\text{Dop}}}{k v_m}\right)^2}\, d\Delta_{\text{Dop}}\,, \tag{1.23}$$

where k is the wave number. The corresponding line width (FWHM) is then given by

$$\delta\omega = k\sqrt{\ln(2)\frac{8k_BT}{m}}\,. \tag{1.24}$$

To actually calculate the linear and nonlinear susceptibility for a Doppler broadened medium, for each propagation direction, we have to add Δ_{Dop} to the detuning of the fields propagating in this direction and then average the resulting susceptibility over the velocity distribution Eq. (1.23).

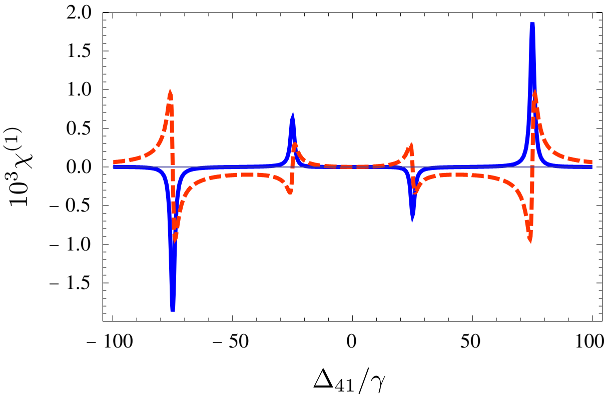

Figure 1.2: Real part (solid blue line) and imaginary part (dashed red line) of the linear susceptibility of the probe field. Due to strong control fields $\Omega_{42} = 100\gamma$ and $\Omega_{31} = 50\gamma$ the probe field resonance is split into four different resonances. Further, $\Omega_{32} = \Delta_{31} = \Delta_{32} = \Delta_{42} = 0$, and all spontaneous decay rates γ_{jk} have been set to γ. The susceptibility is plotted in units of $3/8\pi^2\lambda_{41}^3 N_s$.

1.2.7 Buffer gas and pressure broadening

Introducing a buffer gas to the gas cell leads to more frequent collisions between the atoms. This has two main consequences. First of all it causes pressure broadening. For moderate densities, a collision between two atoms disturbs the level energies for a short time which results in the loss of phase coherence. In a simple approach this can be modeled by an additional decay rate γ_c for the coherences. This collisional decay rate consists of a contribution due to the studied gas itself and a contribution due to the buffer gas. Both depend linearly on the respective densities N_s and N_b [26],

$$\gamma_c = C_s N_s + C_b N_b \,, \tag{1.25}$$

with gas specific constants C_s for the studied gas and C_b for the buffer gas.

A second major effect of a buffer gas is closely connected to Doppler broadening. Due to the higher density the mean free path of a single atom moving in the gas is reduced. If it is reduced below the transition wavelength an averaging over different velocities during a single emission or absorption process can effectively re-narrow a Doppler broadened line. This phenomenon is known as Dicke narrowing [68].

1.3 Results

In principle, Eqs. (1.12) can be used to calculate analytical results for the desired $\chi^{(1)}$ and $\chi^{(3)}$. But in our situation of interest where all four electromagnetic fields, possibly all with different detuning, interact with the atom, these are usually to lengthy to give any physical insight. Therefore, we proceed with a numerical study of the linear and nonlinear susceptibility.

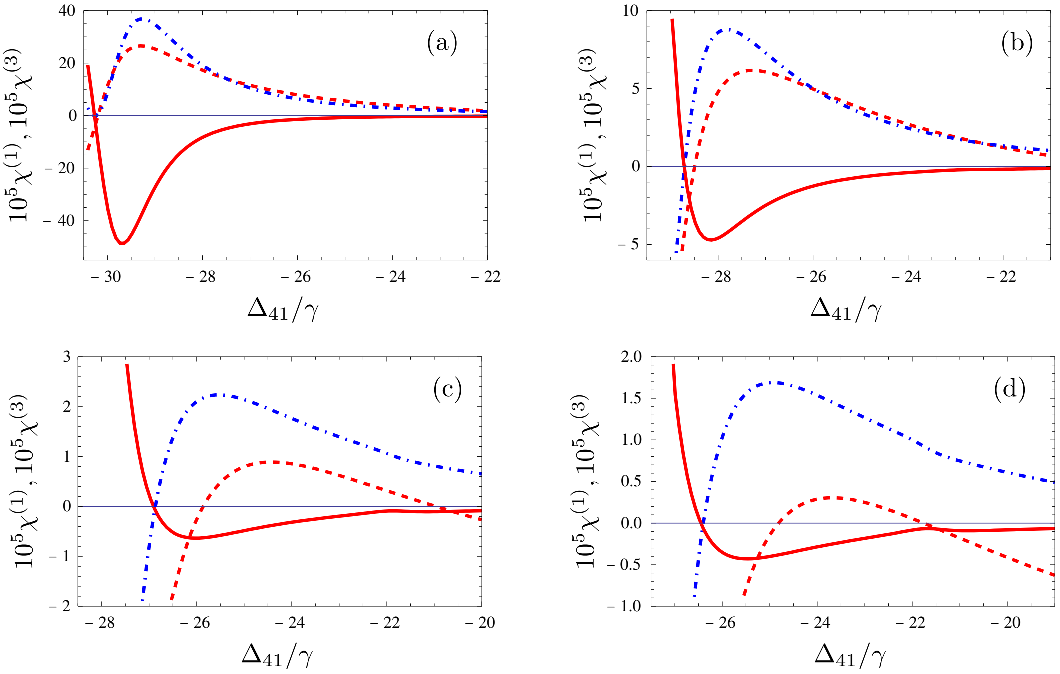

Figure 1.3: Real part (dash-dotted blue line) and imaginary part (solid red line) of the nonlinear susceptibility together with the imaginary part of the linear susceptibility (dashed red line). All figures show the resonance around $\Delta_{41} = -25\gamma$. The susceptibility is plotted in units of $3/8\pi^2\lambda_{41}^3 N$ and for comparability $\chi^{(3)}$ has been scaled with $3/4E_{41}^2$. The parameters are $\Delta_{32} = \Delta_{42} = 0$, $\Omega_{31} = 50\gamma$, $\Omega_{32} = 34\gamma$, and $\Omega_{42} = 100\gamma$. The probe field strength is assumed to be one tenth of the weakest control field in all cases. The detuning Δ_{31} is chosen as (a) $\Delta_{31} = 0$, (b) $\Delta_{31} = 0.7\gamma$, (c) $\Delta_{31} = 1.5\gamma$, and (d) $\Delta_{31} = 1.7\gamma$. Note the different axis scales in the four subpanels.

1.3.1 Without Doppler broadening

Here, our primary goal is to find a set of parameters where the intensity dependent refractive index is large enough to cause an appreciable amount of nonlinear selfphase modulation while the attenuation of a light pulse due to absorption is small. To achieve a high non-linear index of refraction with low linear and non-linear loss all in the same spectral region is challenging because resonances that enhance the nonlinear response typically come with strong absorption. Still, we find such a suitable parameter set by manipulating the linear and nonlinear susceptibility of the probe field as described next.

We first split the unperturbed resonance of the probe field transition by a strong coupling field Ω_{42} and again about half as much by the second coupling field Ω_{31}. This gives rise to four resonance structures in the linear response, see Fig. 1.2.

In this figure, the linear absorption of the resonance at $\Delta_{41} \approx -25\gamma$ can be lowered by a small detuning Δ_{31}, which modifies the dressed state populations.

Finally, optimizing the result with the third coupling Ω_{32}, we can tune one half of the resonance to a small linear and nonlinear absorption while still maintaining a substantial nonlinear real part. In Fig. 1.3 it is shown how gradually introducing a detuning Δ_{31} influences the linear absorption, the nonlinear gain, and the real part of the nonlinear susceptibility. It decreases the linear absorption and the nonlinear gain faster than the real part and thereby improves their ratio. Interestingly, the imaginary parts of the linear and the nonlinear parts of the susceptibility can have opposite signs in this spectral region . The linear response induces absorption, while the nonlinear response leads to gain. Absorption could in this spectral region therefore be reduced even further by a partial cancelling of linear absorption and nonlinear gain. However, these results are preliminary in the sense, that no effects due to Doppler and pressure broadening have been included yet.

1.3.2 Including Doppler broadening

Using our considerations from Secs. 1.2.6 and 1.2.7 we now want to calculate the linear and nonlinear susceptibility in a Doppler broadened atomic gas. As a realistic example we want to assume a Sodium vapor with a density of $N_s = 1.0 \times 10^{20}\,\mathrm{m}^{-3}$. To reach a vapor pressure that corresponds to this density the gas cell must be heated to a temperature of $T = 547.6$ K [69]. At this temperature the Doppler linewidth is $\delta\omega = 2\pi \times 1.78$ GHz which is very broad compared to the natural linewidth of the Sodium D_1 transition of $\gamma = 2\pi \times 9.76$ MHz. In a pure Sodium vapor the spectral features we found in Sec. 1.3.1 would be averaged out by the Doppler effect. But if we introduce a buffer gas strong pressure broadening can preserve them. For Sodium and Argon, the gas parameters in Eq. (1.25) are given by $C_s = 1.50 \times 10^{-13}\,\mathrm{m}^3\,\mathrm{s}^{-1}$ and $C_b = 2.53 \times 10^{-15}\,\mathrm{m}^3\,\mathrm{s}^{-1}$ [26]. We want to assume a collision-induced coherence loss rate of $\gamma_c = 1.0$ GHz which corresponds to a buffer gas density of $N_b = 3.95 \times 10^{23}\mathrm{m}^{-3}$. At such a density the mean free path is of order $\Lambda = 10^{-5}$ m. This is much larger than the transition wavelength $\lambda = 589.2 \times 10^{-9}$ m such that the limit of Dicke narrowing is not reached.

We now try to recover results similar to the unbroadened case shown in Fig. 1.3. Because of the strong broadening we have to apply correspondingly stronger control fields. For $\Omega_{42} = 60.0$ GHz and $\Omega_{31} = 30.0$ GHz, we find the resonance studied in the unbroadened case at around $\Delta_{41} = -15.0$ GHz. The third control field is set to $\Omega_{32} = 25.0$ GHz and the detuning to $\Delta_{31} = 1.6$ GHz. For the Doppler averaging we have assumed all fields to be co-propagating. The different subpanels in Fig. 1.4 correspond to different Doppler linewidths, and thus via Eq. (1.24) to different temperatures. In Fig. 1.4(a), the Doppler linewidth is chosen below the natural linewidth of the probe transition, and as expected we finds results that are similar in shape to the unbroadened case (see Fig. 1.3(d)). Differences are mainly due to pressure broadening. In Fig. 1.4 (b) - (d) we gradually increase the Doppler linewidth up to the full Doppler width expected for the gas parameters discussed above. We find that while the shapes of the different curves change, our main result of high nonlinear index of refraction with small linear and nonlinear

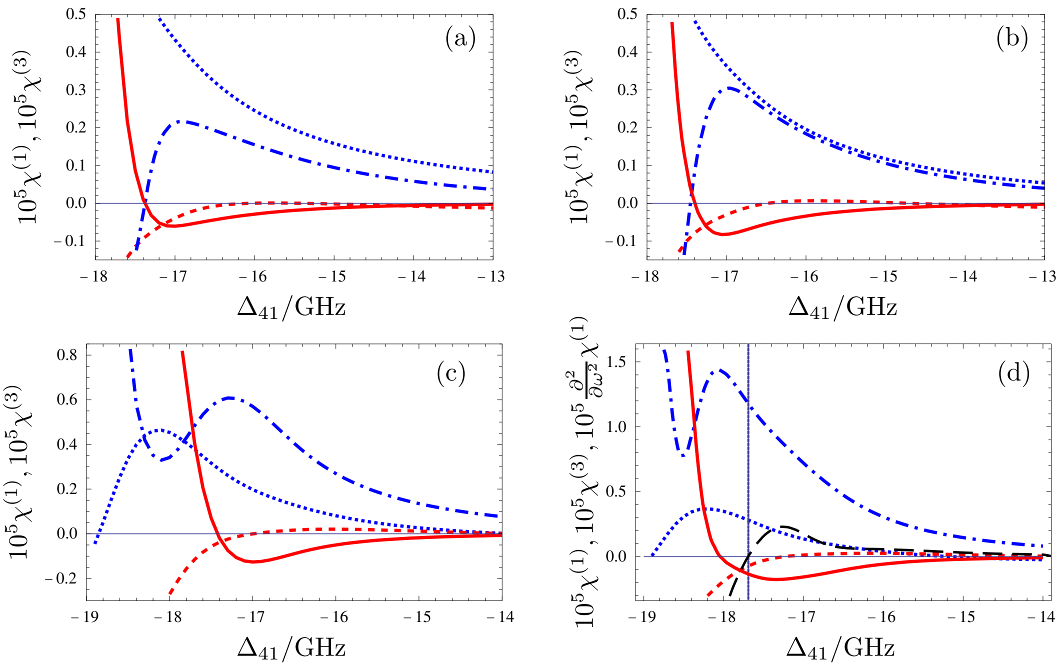

Figure 1.4: Real part (dash-dotted blue line) and imaginary part (solid red line) of the nonlinear susceptibility together with the real part (blue dotted line) and the imaginary part of the linear susceptibility (dashed red line) at the resonance around $\Delta_{41} = -15.0$ GHz. The control fields have Rabi frequencies $\Omega_{42} = 60$ GHz, $\Omega_{31} = 30$ GHz, $\Omega_{32} = 25$ GHz, and the detunings are $\Delta_{31} = 1.6$ GHz, $\Delta_{32} = \Delta_{42} = 0$. The medium parameters described in the main text correspond to Sodium as the active medium with Argon as a buffer gas. The four different plots show Doppler averaged results with a Doppler linewidth of (a) below the natural linewidth, (b) 50%, (c) 90%, and (d) 100% of the full Doppler linewidth of $\delta\omega = 2\pi \times 1.78$ GHz. In plot (d) we also included the second derivative of the real part of the linear susceptibility (long-dashed black line).

absorption persists with Doppler broadening. Also in the broadened case, a partial cancelling of linear absorption and nonlinear gain could be possible. Note that since the averaging process affects not only the probe field detuning but all four detunings at the same time the results cannot be explained in terms of a simple smoothing of the curves without Doppler effect.

We also considered different laser geometries, such as control fields propagating perpendicular to the probe field, or one or two control field propagating in opposite directions, and found the co-propagating case to be the most advantageous one. This is similar to the case of Doppler broadening in standard electromagnetically induced transparency setups where co-propagating lasers typically are preferable.

We finally use our results to calculate the required optical length for a nonlinear selfphase modulation of π at a probe field frequency with vanishing group velocity dispersion. The group velocity dispersion is given by [44]

$$\beta_2 = \frac{k}{4}\frac{\partial^2 Re[\chi^{(1)}]}{\partial\omega^2}, \tag{1.26}$$

where the wave vector k gives the characteristic length scale. The frequency of vanishing group velocity dispersion is thus given by the condition

$$\frac{\partial^2 Re[\chi^{(1)}]}{\partial\omega^2} = 0\,, \tag{1.27}$$

which for the considered gas parameters yields

$$\Delta_{41}^{\mathrm{min}} = 17.63 \text{ GHz}. \tag{1.28}$$

This probe field frequency is indicated by the vertical solid blue line in Fig. 1.4(d).

The nonlinear selfphase modulation is given by [26]

$$\Delta\Phi_{\mathrm{Nl}} = n_2\, I\, k\, L\,, \tag{1.29}$$

with n_2 the intensity dependent refractive index, I the probe field intensity, k the wavevector, and L the propagation length. We assume a probe field strength one tenth of the smallest control field and find at frequency $\Delta_{41}^{\mathrm{min}}$

$$L_\pi = 6.4 \text{ cm}\ . \tag{1.30}$$

From Fig. 1.4(d) we see that at $\Delta_{41}^{\mathrm{min}}$ the magnitude of the imaginary parts of the linear and nonlinear susceptibility are more than one order of magnitude smaller than the real part of the nonlinear susceptibility. Therefore, the equivalent characteristic length scale is more than one order of magnitude larger. Furthermore, both linear and nonlinear part, give rise to small gain rather than absorption.

To asses the frequency range in which the calculated nonlinear selfphase modulation length can be archived without significant pulse shape distortion we in addition studied the group velocity dispersion. It is related via Eq. (1.26) to the second derivative of the real part of the linear susceptibility which is shown as the long-dashed black curve in Fig. 1.4(d). Figure 1.5 shows a magnification of Fig. 1.4(d) around $\Delta_{41}^{\mathrm{min}}$. We see that in a spectral range of several natural linewidth the second derivative of the real part of the linear susceptibility is about one order of magnitude smaller than the real part of the nonlinear susceptibility that is responsible for the nonlinear selfphase modulation. This suggests that a pulse with a bandwidth of up to several natural linewidth would suffer only little from group velocity dispersion on the calculated nonlinear selfphase modulation length.

For a more quantitative measure, we calculate the ratio of time spread to temporal width of a pulse with a bandwidth of x times the natural line width γ. The corresponding temporal width of the pulse is

$$\tau = \frac{2\pi}{x\gamma}\,. \tag{1.31}$$

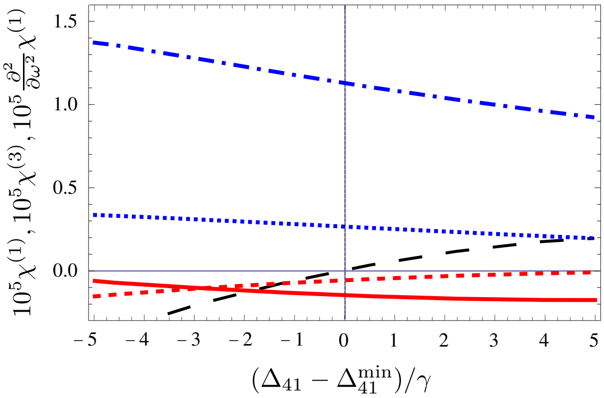

Figure 1.5: A magnification of Fig. 1.4 (d) around the probe field frequency $\Delta_{41}^{\rm min}$ with vanishing group velocity dispersion [see Eq. (1.28)] is shown. The frequency axis is shown in units of the natural decay rate γ, which for the considered Sodium D1 transition is $2\pi \times 9.76$ MHz. The parameters are the same as for Fig. 1.4 (d).

The time spread of such a pulse is related to the parameter β_2 given by Eq. (1.26) in the following way [44],

$$\Delta\tau = L\,\beta_2\, x\gamma\,. \tag{1.32}$$

From Fig. 1.5, we estimate an average value of the second derivative of the real part of the linear susceptibility around $\Delta_{41}^{\rm min}$ of 0.2 (scaled quantity). For the ratio of $\Delta\tau$ and τ after a propagation length of L_π we find

$$\begin{aligned}\frac{\Delta\tau}{\tau} &= \frac{1}{2\pi}\, L_\pi\, \beta_2\, \gamma^2\, x^2 && (1.33)\\ &= 0.042\, x^2\,. && (1.34)\end{aligned}$$

Thus, the pulse doubles its temporal width for $x = 4.9$. For longer pulses, x becomes smaller, and this ratio improves with x^2.

Our results show that in a spectral range of several natural line width a nonlinear selfphase modulation of π can be achieved on a realistic laboratory lengthscale. We showed that in the same spectral range group velocity dispersion is low such that pulse shape distortions can be expected to be small. Interestingly, the real part of the linear susceptibility has a negative slope in the considered frequency region, in contrast to a positive slope typically found in an electromagnetically induced transparency window.

1.4 Conclusion

We have studied nonlinear effects in pulse propagation through a laser-driven medium where the applied fields form a closed interaction loop. Such loop systems in general only allow for a time-independent treatment at a single probe field frequency, where the so-called multiphoton resonance condition is fulfilled. As a probe field pulse has a finite frequency width, this condition which allows for a straightforward theoretical treatment could not be applied. Instead, we treated the time-dependent problem by turning it into a hierarchy of equations that describe the various physical processes occurring in the medium. We have included Doppler and pressure broadening as well as a buffer gas in our analysis and have used realistic parameters for a medium consisting of Sodium vapor. We could show that the studied system can exhibit a high non-linear refractive index with small absorption or gain over a spectral range of several natural line widths. For the chosen parameters, group velocity dispersion is low, such that pulse shape distortions are minimized, and the slope of the linear dispersion is negative. A non-linear selfphase modulation of π is obtained after 6.4 cm propagation through the medium.

1.A Appendix

The explicit form of the coefficient matrix M and the inhomogeneous part Σ can be derived from Eq. (1.7). Here, we list all nonzero elements $M_{j,k}$ and Σ_j, which are given by

$$
\begin{aligned}
M_{1,1} &= M_{1,6} = M_{6,6} = \frac{1}{2}M_{11,11} = \Sigma_1 = \Sigma_6 = -\gamma_r \,, \\
M^*_{1,3} &= M_{1,9} = M_{2,10} = M_{3,4} = M_{4,12} = M^*_{5,7} = M_{9,11} = M^*_{13,15} = \frac{i}{2}\Omega_{31} \,, \\
M^*_{2,3} &= M_{5,9} = M^*_{6,7} = M_{6,10} = M_{7,11} = M_{8,12} = M^*_{10,11} = M^*_{14,15} = \frac{i}{2}\Omega_{32} \,, \\
M^*_{1,4} &= M_{1,13} = M_{2,14} = M_{3,15} = \frac{1}{2}M^*_{4,1} = M^*_{4,6} = M^*_{4,11} = M^*_{5,8} \\
&= M^*_{9,12} = \frac{1}{2}M_{13,1} = M_{13,6} = M_{13,11} = \Sigma^*_4 = \Sigma_{13} = \frac{i}{2}\Omega_{41}e^{-i(\Delta t-\phi)} \,, \\
M^*_{2,4} &= M_{5,13} = M^*_{6,8} = M_{6,14} = M_{7,15} = M^*_{8,1} = \frac{1}{2}M^*_{8,6} = M^*_{8,11} \\
&= M^*_{10,12} = M_{14,1} = \frac{1}{2}M_{14,6} = M_{14,11} = \Sigma^*_8 = \Sigma_{14} = \frac{i}{2}\Omega_{42} \,, \\
M_{3,3} &= M^*_{9,9} = -\gamma_r - i\Delta_{31} \,, \\
M_{4,4} &= M^*_{13,13} = -\gamma_r - i(\Delta_{31} + \Delta_{42} - \Delta_{32}) \,, \\
M_{7,7} &= M^*_{10,10} = -\gamma_r - i\Delta_{32} \,, \\
M_{7,8} &= M_{10,10} = -\gamma_r - i\Delta_{32} \,, \\
M_{12,12} &= M^*_{15,15} = -2\gamma_r - i(\Delta_{42} - \Delta_{32}) \,, \\
M_{2,2} &= M^*_{5,5} = -i(\Delta_{31} - \Delta_{32}) \,, \\
M_{6,4} &= M_{11,4} = M_{6,13} = M_{11,13} = M_{1,8} = M_{11,8} = M_{1,14} = M_{11,14} = 0 \,,
\end{aligned}
$$

where $M_{j,k} = M_{k,j}$ holds if not noted otherwise and by $M^*_{j,k}$ we indicate the complex conjugate of $M_{j,k}$.

Chapter 2

Group velocity control via interacting dark-state resonances

The propagation of a weak probe field in a laser-driven four-level atomic system is investigated. We choose mercury as our model system, where the probe transition is in the ultraviolet region. A high-resolution peak appears in the optical spectra due to the presence of interacting dark resonances. We show that this narrow peak leads to superluminal light propagation with strong absorption, and thus by itself is only of limited interest. But if in addition a weak incoherent pump field is applied to the probe transition, then the peak structure can be changed such that both sub- and superluminal light propagation or a negative group velocity can be achieved without absorption, controlled by the incoherent pumping strength. A suitable choice of laser propagation directions allows to preserve these results under Doppler averaging.

2.1 Introduction

Optical properties of an atomic medium can be substantially modified by the application of external fields. In particular, atomic coherence induced by laser fields plays an important role in light-matter interaction and has found numerous implementations in optical physics [44]. One prominent application is the modification of the propagation of a light pulse through an atomic medium, which depends on the dispersive properties of the medium. The study of such pulse propagation phenomena has been triggered by a series of papers by Sommerfeld and Brillouin [70,71] and continues to be of much interest [23,56,72–80]. It is well known that the group velocity of a light pulse can be slowed down [81–83], can become faster than its value c in vacuum, or can even become negative [50,52,84–100]. Note that superluminal light propagation with group velocity larger than c cannot transmit information faster than the vacuum speed of light, such that it is not at odds with causality [101,102]. Superluminal light propagation has been investigated for many potential uses, not only as a tool for studying a very peculiar state of matter, but also for developing quantum computers, high speed optical switches and communication systems [103].

Both experimental and theoretical studies have been performed to realize super- and subluminal light propagation in a single system. For example, speed control in atomic systems has been achieved by changing the frequencies, amplitudes or phase differences of the applied fields. It has been shown that switching from subluminal to superluminal pulse propagation can be achieved by the intensity of the coupling fields [89–92], and the relative phase between two weak probe fields [93]. Morigi et al. [50] have compared the phase-dependent properties of the $\diamond$ (diamond) four level system with those of the double Λ system. In Ref. [94], gain-assisted superluminal light propagation was observed in a cesium vapor cell while in most other studies, superluminal light propagation is accompanied by considerable absorption. Sub- and superluminal light propagation together with nonlinear optical gain or losses were observed in [96]. In [97], subnatural absorption resonances with positive and negative dispersion were demonstrated in a standing wave field. Steep negative dispersion is also possible in atomic media exhibiting electromagnetically induced absorption [98]. Two of the present authors suggested to use an incoherent pump field to control light propagation from subluminal to superluminal [99, 100]. Recently, we have studied the light propagation of a probe pulse in a four-level double lambda system, where the applied laser fields form a closed interaction loop [52]. In such systems, the finite frequency width of a probe pulse requires a time dependent treatment of the light propagation. We have found both sub- and superluminal light propagation without absorption or with gain, controlled by the Rabi frequency of one of the coupling fields.

All these effects depend on the modification of the dispersive and absorptive properties of the atomic medium. A particular class of systems that allows to modify the optical response to a great extend are those with so-called interacting dark resonances [104]. A characteristic feature of such systems is the appearance of very sharp, high-contrast structures in the optical spectra. Resonances associated with double dark states can be made absorptive or transparent and their optical properties such as width and position can be manipulated by applying suitable coherent interactions. It was also shown that very weak incoherent excitation of the atoms can be sufficient to turn absorptive features into optical gain structures. This has been proposed as a model system to obtain strong laser gain in the ultraviolet and vacuum ultraviolet regime by Fry et al. [105].

In this chapter we consider probe pulse propagation through a system which exhibits interacting dark resonances. The level configuration of our four-level scheme is based on the lasing system proposed in [105], and consists of three atomic states in ladder configuration, with an additional fourth perturbing state coupled by a laser field to the upper state of the ladder system. The lower transition of the ladder system acts as the probe transition. This system can be realized, e.g., in mercury, where the probe transition has a low wavelength of 253.7 nm, i.e., in the ultraviolet

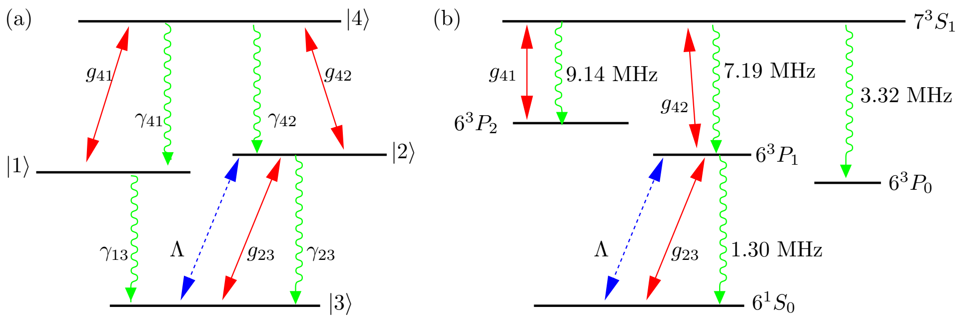

Figure 2.1: (a) Energy scheme of the four level atomic system considered. Transition $|2\rangle \leftrightarrow |4\rangle$ is driven by a strong laser field, transition $|1\rangle \leftrightarrow |4\rangle$ by a weak coupling field, and the probe field interacts with transition $|2\rangle \leftrightarrow |3\rangle$. In addition, a weak incoherent field is applied to the probe field transition. (b) A possible realization of the scheme in mercury. Population transfer to state 6^3P_0 has to be compensated via a repump field.

region. We find that the medium susceptibility in dependence on the probe field detuning exhibits high-contrast structures characteristic of interacting dark states. These structures typically lead to superluminal probe field propagation with high absorption, and thus as such are of limited interest. If, however, a weak incoherent pumping is applied in addition to the probe field transition, then we find that in the region around a narrow structure both sub- and superluminal propagation as well as negative group velocities are possible without absorption, controlled by the incoherent pumping strength.

The chapter is organized as follows. In the next section (Sec. 2.2) we present our model scheme, the corresponding equations of motion, and derive analytic expressions for the response of the atomic medium. In Sec. 2.3 we then present numerical results for the different cases without interacting dark state resonance, with interacting dark state resonance, and with incoherent pumping. We interpret these results in the dressed state picture and also study the influence of Doppler averaging.

2.2 Analytical considerations

2.2.1 The model system

We consider an atomic four level system as shown in figure 2.1(a). Transition $|2\rangle \leftrightarrow |4\rangle$ is driven by a strong coherent field with frequency ω_{42} and Rabi frequency g_{42}. A weak coupling field with frequency ω_{41} and Rabi frequency g_{41} is applied to transition $|1\rangle \leftrightarrow |4\rangle$. The weak probe field with frequency ω_{23} and Rabi frequency $g_{23} = g_p$ couples to transition $|2\rangle \leftrightarrow |3\rangle$. Finally, an incoherent driving field with pump strength Λ is applied to the probe transition. We further include spontaneous decay with rates γ_{41}, γ_{42}, γ_{23}, and γ_{13}, respectively, on the dipole-allowed transitions. The atomic transition frequencies are denoted by $\bar{\omega}_{ij}$, and the laser field detunings with respect to the atomic transition frequencies are $\Delta_{ij} = \omega_{ij} - \bar{\omega}_{ij}$ $(i, j \in 1, \ldots, 4)$. A realization of our level scheme can be found, e.g., in mercury, see figure 2.1(b).

The density matrix equations of motion, in the rotating wave approximation, are

$$\dot{\rho}_{11} = -\, 2\gamma_{13}\rho_{11} + 2\gamma_{41}\rho_{44} - ig_{41}^{*}\rho_{14} + ig_{41}\rho_{41}\,, \tag{2.1a}$$

$$\begin{aligned}\dot{\rho}_{22} = &-\, 2\gamma_{23}\rho_{22} + 2\gamma_{42}\rho_{44} - 2\Lambda\rho_{22} + 2\Lambda\rho_{33} \\ &+ ig_{p}^{*}\rho_{32} - ig_{p}\rho_{23} - ig_{42}^{*}\rho_{24} + ig_{42}\rho_{42}\,,\end{aligned} \tag{2.1b}$$

$$\dot{\rho}_{33} = 2\gamma_{13}\rho_{11} + 2\gamma_{23}\rho_{22} + 2\Lambda\rho_{22} - 2\Lambda\rho_{33} - ig_{p}^{*}\rho_{32} + ig_{p}\rho_{23}\,, \tag{2.1c}$$

$$\dot{\rho}_{12} = -\,(\Gamma_{12} + i\Delta_{41} - i\Delta_{42} + \Lambda)\rho_{12} - ig_{42}^{*}\rho_{14} - ig_{p}\rho_{13} + ig_{41}\rho_{42}\,, \tag{2.1d}$$

$$\dot{\rho}_{13} = -\,(\Gamma_{13} + i\Delta_{41} - i\Delta_{42} - i\Delta_{p} + \Lambda)\rho_{13} - ig_{p}^{*}\rho_{12} + ig_{41}\rho_{43}\,, \tag{2.1e}$$

$$\dot{\rho}_{14} = -\,(\Gamma_{14} + i\Delta_{41})\rho_{14} - ig_{41}\rho_{11} + ig_{41}\rho_{44} - ig_{42}\rho_{12}\,, \tag{2.1f}$$

$$\dot{\rho}_{23} = -\,(\Gamma_{23} - i\Delta_{p} + 2\Lambda)\rho_{23} - ig_{p}^{*}\rho_{22} + ig_{p}^{*}\rho_{33} + ig_{42}\rho_{43}\,, \tag{2.1g}$$

$$\dot{\rho}_{24} = -\,(\Gamma_{24} + i\Delta_{42} + \Lambda)\rho_{24} - ig_{42}\rho_{22} + ig_{42}\rho_{44} + ig_{p}^{*}\rho_{34} - ig_{41}\rho_{21}\,, \tag{2.1h}$$

$$\dot{\rho}_{34} = -\,(\Gamma_{34} + i\Delta_{p} + i\Delta_{42} + \Lambda)\rho_{34} + ig_{p}\rho_{24} - ig_{41}\rho_{31} - ig_{42}\rho_{32}\,, \tag{2.1i}$$

$$\rho_{44} = 1 - \rho_{11} - \rho_{22} - \rho_{33}\,. \tag{2.1j}$$

In the above equations, $\Gamma_{ij} = (2\gamma_i + 2\gamma_j)/2$ are the damping rates of the coherences with γ_i being the total decay rate out of state $|i\rangle$, and $\Delta_p = \Delta_{23}$ is the probe field detuning.

Our main observable is the response of the atomic medium to the probe field. As will be discussed in Sec. 2.2.2, the linear susceptibility of the weak probe field is determined by the probe transition coherence ρ_{23}. We therefore proceed by solving the above equations (2.1a)-(2.1i) in the steady state under the assumption of specific parameter relations.

First, in the absence of the incoherent pump field ($\Lambda = 0$), an expansion of the steady state coherence ρ_{23} to the leading order in the probe field Rabi frequency g_p yields

$$\rho_{23} = \frac{-g_p(|g_{41}|^2 - C_{13}\cdot C_{34})}{|g_{41}|^2 C_{23} + C_{13}(|g_{42}|^2 - C_{23}\cdot C_{34})}\,, \tag{2.2a}$$

$$C_{13} = \Delta_p - \Delta_{41} + \Delta_{42} + i\,\Gamma_{13}\,, \tag{2.2b}$$

$$C_{34} = \Delta_p + \Delta_{42} + i\,\Gamma_{34}\,, \tag{2.2c}$$

$$C_{23} = \Delta_p + i\,\Gamma_{23}\,. \tag{2.2d}$$

It will turn out that an interesting parameter range for the present study is given by

$$\Delta_{41} = \Delta_{42} = 0\,, \tag{2.3a}$$

$$\Delta_p \ll \gamma_{31}, \gamma_{41}, \gamma_{42}\,, \tag{2.3b}$$

$$g_{41} \ll g_{42}\,, \tag{2.3c}$$

$$\gamma_{13} = 0\,. \tag{2.3d}$$

In this limit, equation (2.2a) becomes

$$\rho_{23} = \frac{-g_p(|g_{41}|^2 - i\Delta_p\Gamma_{34})}{|g_{42}|^2\Delta_p + i[|g_{41}|^2\Gamma_{23} - \Delta_p^2(\Gamma_{34} + \Gamma_{23})]}\,. \tag{2.4}$$

An inspection of equation (2.4) reveals that the imaginary part is strictly positive, and the half width of the absorption peak around $\Delta_p = 0$ is determined by

$$w \simeq \left(\frac{g_{41}}{g_{42}}\right)^2 \Gamma_{23} = \left(\frac{g_{41}}{g_{42}}\right)^2 \gamma_{23}\,. \tag{2.5}$$

Next, we seek the corresponding steady state solution for ρ_{23} with incoherent pump field with pump intensity Λ. The parameters are chosen to satisfy equations (2.3a)-(2.3d) as well as the new condition on the pump field

$$\Lambda_0 \ll \Lambda \ll \gamma_{41}, \gamma_{42}\,. \tag{2.6}$$

Further, we assume the Rabi frequencies g_{ij} to be real in the following. We obtain in leading order of the probe field coupling g_p

$$\rho_{23} = \frac{g_{41}^2\, g_p\, \gamma_{23}}{(g_{42}^2\, \gamma_{23} + 2\Lambda\, \Gamma_{24}\, \gamma_{42})} \frac{\Delta_p - i\Lambda}{\Delta_p^2 + \Lambda^2}\,. \tag{2.7}$$

Here the parameter Λ_0 is defined by

$$\Lambda_0 = \frac{g_{41}\, \gamma_{23}\, (\gamma_{41} + \gamma_{23})}{g_{42}^2\, \gamma_{41} + \gamma_{23}\, \Gamma_{34}\, (\gamma_{41} + \gamma_{23})} \simeq \left(\frac{g_{41}}{g_{42}}\right)^2 \gamma_{23}\,. \tag{2.8}$$

Since $|g_{41}/g_{42}|^2\gamma_{23}$ can be made small, for a suitable combination of the Rabi frequencies g_{41} and g_{42} the condition $\Lambda \gg \Lambda_0$ can be fulfilled even for incoherent pump strengths which are orders of magnitude smaller than those required, e.g., to saturate the optical transition.

We find that the imaginary part of equation (2.7) is negative if the condition $\Lambda \gg \Lambda_0$ is fulfilled. Thus Λ_0 indicates the incoherent pumping rate at which the absorption peak turns into a gain structure, if the conditions in equations (2.3a)-(2.3d) and (2.6) are fulfilled.

2.2.2 Observables

Our main observable is the response of the atomic medium to the probe field. The linear susceptibility of the weak probe field can be written as [4]

$$\chi(\omega_p) = \frac{N\eta_p}{\epsilon_0 E_p}\rho_{23}(\omega_p)\,, \tag{2.9}$$

where N is the atom number density in the medium, η_p is the probe transition dipole moment and $\chi = \chi' + i\chi''$. The susceptibility $\chi(\omega_p)$ is related to the index of refraction $n = n' + in''$ via $n^2(\omega_p) = 1 + \chi(\omega_p)$, and the real and imaginary parts of $\chi(\omega_p)$ correspond to the dispersion and the absorption, respectively.

The slope of the dispersion with respect to the probe detuning has a major role in the calculation of the group velocity. We introduce the group index, $n_g = c/v_g$, where the group velocity v_g of the probe field for vanishing absorption is given by [81, 94]

$$v_g = \frac{c}{n'(\omega_p) + \omega_p/[2n'(\omega_p)]\,\frac{\partial \chi'(\omega_p)}{\partial \omega_p}}\,. \tag{2.10}$$

Equation (2.10) implies that, for a negligible real part $\chi'(\omega_p)$, the group velocity can be significantly reduced via a steep positive dispersion. Strong negative dispersion, on the other hand, can lead to an increase in the group velocity and even to a negative group velocity.

Substituting equations (2.7) and (2.9) in equation (2.10), the group index of the probe field evaluates to

$$n_g - 1 = \frac{g_{41}^2\, g_p\, \gamma_{23}}{(g_{42}^2\, \gamma_{23} + 2\,\Lambda\,\Gamma_{24}\,\gamma_{42})}\,\frac{\Delta_p^2 - \Lambda^2}{(\Delta_p^2 + \Lambda^2)^2}\,. \tag{2.11}$$

It can be expected from equation (2.11) that for suitable parameters, the group index around $\Delta_p = 0$ is negative and accompanied by gain, and this is indeed what we find below.

The relation between coherence and susceptibility equation (2.9) can be rewritten as

$$\chi(\omega_p) \;=\; \frac{N\eta_p}{\epsilon_0 E_p}\rho_{23}(\omega_p) = \frac{3N\lambda_p^3}{8\pi^2}\,\frac{\gamma_{23}}{\gamma}\,\frac{\rho_{23}(\omega_p)}{g_p/\gamma}\,, \tag{2.12}$$

where we have used $\gamma_{23} = (\eta_p^2 \bar{\omega}_{23}^3)/(3\pi\epsilon_0\hbar c^3)$ and $g_p = \eta_{23}E_p/\hbar$ as well as $\omega_{23} = 2\pi c/\lambda_{23}$ with the probe transition wavelength λ_{23}. For mercury probe wavelength 253.7 nm, particle density $N = 10^{12}\text{cm}^{-3}$ and $\gamma_{23}/\gamma = 0.14$ as found in mercury one finally obtains

$$\chi(\omega_p) = 8.7 \times 10^{-5}\,\frac{\rho_{23}(\omega_p)}{g_p/\gamma}\,. \tag{2.13}$$

Throughout our discussion of numerical results, we will assume these parameters in order to evaluate the susceptibility.

2.3 Results

2.3.1 Without interacting dark state resonance

In figure 2.2 we show the real (blue dashed) and imaginary (red solid) part of the probe field susceptibility χ versus the probe detuning Δ_p, which correspond to the dispersive and absorptive properties of the medium, respectively. In this figure, the perturbing laser field is switched off, $g_{41} = 0$. The other parameters are $\gamma_{41} =$

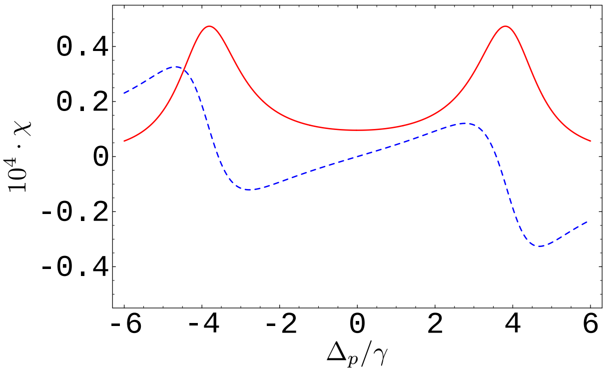

Figure 2.2: Real (blue dashed) and imaginary (red solid) parts of the susceptibility χ as a function of the probe detuning Δ_p for the parameters $\gamma_{41} = \gamma$, $\gamma_{23} = 0.14\,\gamma$, $\gamma_{42} = 0.79\,\gamma$, $\gamma_{13} = 0.01\,\gamma$, $g_p = 10^{-4}\,\gamma$, $g_{41} = 0$, $g_{42} = 4\,\gamma$, $\Lambda = 0$, $\Delta_{42} = \Delta_{41} = 0$.

$\gamma, \gamma_{23} = 0.14\,\gamma$, $\gamma_{42} = 0.79\,\gamma$, $\gamma_{13} = 0.01\,\gamma$, $g_p = 10^{-4}\,\gamma, g_{42} = 4\,\gamma$, $\Lambda = 0$, $\Delta_{42} = \Delta_{41} = 0$. Note that the ratios of the decay rates correspond to the case found in mercury, see figure 2.1(b). We have added a weak decay rate γ_{13}, since otherwise in the steady state all population is trapped in $|1\rangle$. The driving field with Rabi frequency g_{42} leads to an Autler-Townes doublet with a dip in the absorption at zero detuning, i.e., partial electromagnetically induced transparency (EIT). The slope of the real part of the susceptibility in the region of reduced absorption is positive. We thus find that subluminal light propagation occurs around zero detuning with reduced absorption as it is common for EIT. If the state $|4\rangle$ was long-lived, then the EIT leading to the partial transparency would be more pronounced such that the absorption would vanish at zero detuning.

2.3.2 With interacting dark state resonance

In figure 2.3, in addition we apply the weak perturbing field with Rabi frequency $g_{41} = 0.04\,\gamma$, and assume negligible decay on transition $|3\rangle \leftrightarrow |1\rangle$, since a trapping in this state is now avoided by the additional laser field. The results are identical to figure 2.2 except for a narrow absorption spike at around zero detuning. The shape and width of the absorption spike are determined by equation (2.2a) and equation (2.5), respectively. In particular, the width is much less than the natural linewidth. Again, for a long-lived state $|4\rangle$, the transparency regions on each side of the absorption spike would become two points of EIT, i.e., a double dark state [104]. In terms of the light propagation, the slope of the real part of the susceptibility around zero detuning is negative such that superluminal light propagation could be observed, albeit with high absorption.

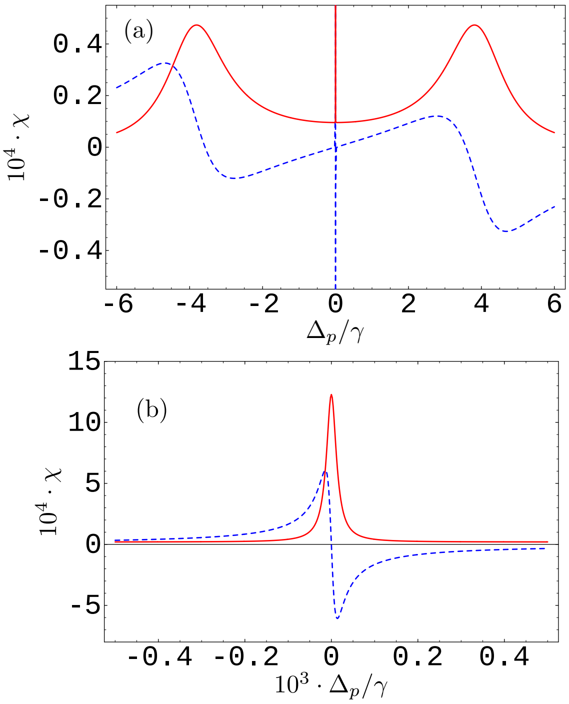

Figure 2.3: Real (blue dashed) and imaginary (red solid) parts of the susceptibility χ as a function of the probe detuning for $\gamma_{13} = 0$ and $g_{41} = 0.04\,\gamma$. The other parameters are the same as in figure 2.2. (b) is a closeup on the central part of (a).

2.3.3 With interacting dark state resonance and incoherent pumping

We now in addition apply a weak incoherent pumping field on the probe transition $|2\rangle - |3\rangle$. Figure 2.4 shows the corresponding results. The incoherent pump field rate is chosen as $\Lambda = 4 \times 10^{-5}\gamma$. In this case, the superluminal light propagation found in figure 2.3 at $\Delta_p = 0$ switches to subluminal propagation, and the absorption spike at zero detuning becomes a gain spike. The shape of the gain spike is determined by the imaginary part of equation (2.7) which is Lorentzian with halfwidth equal to Λ. A dressed-state analysis of the transition to an amplifying medium will be given in section 2.3.4. It can be seen from figure 2.4 that at $\Delta_p \approx \pm 3.1 \times 10^{-4}\gamma$ (indicated by the purple vertical lines), the imaginary part of the susceptibility vanishes together with a negative slope of the real part. At these probe field detunings, the real part of the susceptibility itself is non-zero, and is negative (positive) for $\Delta_p \approx -3.1 \times 10^{-4}\gamma$ ($\Delta_p \approx -3.1 \times 10^{-4}\gamma$). In the following, we discuss the two cases of interest with resonant or non-resonant probe field separately.

We start with the resonant case $\Delta_p = 0$. In figure 2.5(a), we study the effect of the incoherent pumping strength Λ on the magnitude of the imaginary part of the susceptibility χ at resonance $\Delta_p = 0$. It can be seen that depending on the

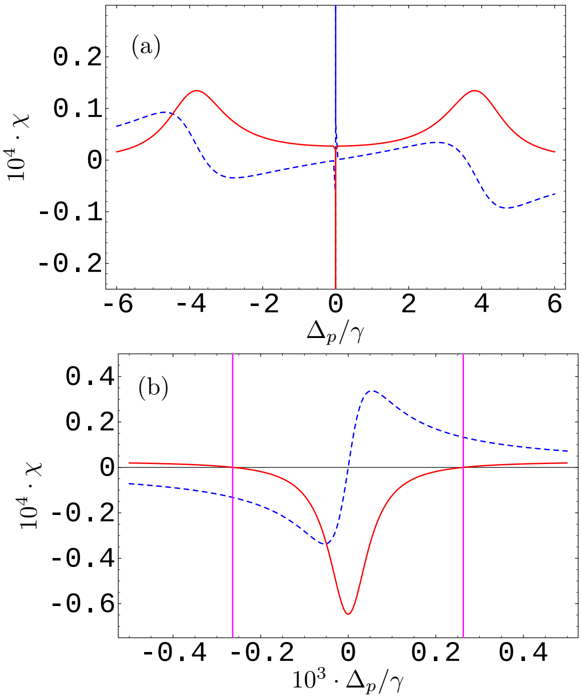

Figure 2.4: Real (blue dashed) and imaginary (red solid) parts of the susceptibility χ as a function of the probe detuning for $\Lambda = 4 \times 10^{-5}\,\gamma$. The other parameters are the same as in figure 2.3. (b) is a closeup on the central part of (a). The purple vertical lines indicate the roots of the imaginary part.

coupling field Rabi frequency g_{42}, the transition from absorption to gain occurs at different values of the incoherent pumping. For the parameters of figure 2.3, which correspond to the long-dashed green curve in figure 2.5(a), the transition is at about $\Lambda \approx 2 \times 10^{-5}\,\gamma$. This explains why gain could be observed for the parameters in figure 2.4. On increasing the incoherent pumping further, the imaginary part approaches zero again.

After the discussion of the absorption, we now turn to a discussion of our main observable, the group velocity. Since the real part of χ itself vanishes at $\Delta_p = 0$, the group velocity is determined by the slope of the real part of the susceptibility at $\Delta_p = 0$, see equation (2.10). This quantity is shown in figure 2.5(b). It can be seen that, for no or small incoherent pumping, the system exhibits a negative slope, which leads to a superluminal or even negative group velocity. On increasing Λ, the slope can be adjusted to large positive values, where subluminal light can be expected. Thus in principle the system allows for a wide range of group velocities, controlled via the incoherent pump rate Λ. But from a comparison of figures 2.5 (a) and (b) it can be seen that typically negative slopes are accompanied by absorption, while positive slopes occur together with gain. Thus at $\Delta_p \approx 0$, only a reduction of the group velocity is accessible in experiments without absorption. The different curves

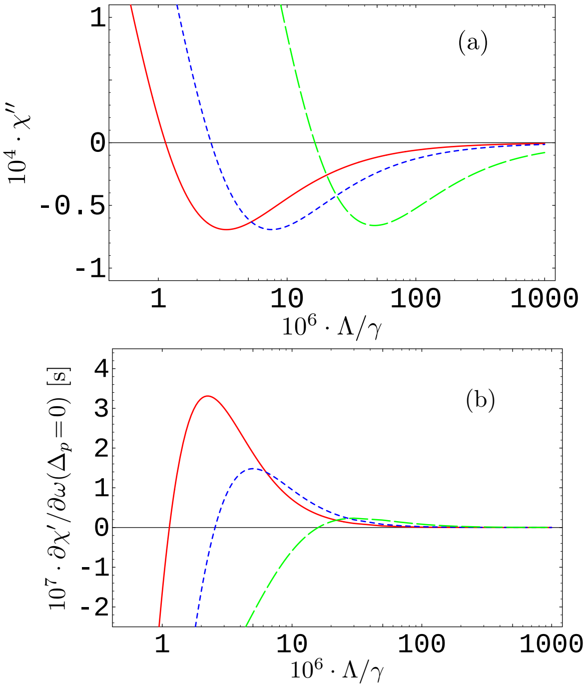

Figure 2.5: (a) Imaginary part χ'' of the susceptibility as a function of the pumping field strength Λ. The parameters are as in figure 2.3 with $\Delta_p = 0$, and $g_{42} = 15\gamma$ (solid red), 10γ (short-dashed blue), 4γ (long-dashed green). (b) Slope of the real part χ' of the susceptibility at zero probe field detuning $\Delta_p = 0$ for parameters as in (a).

in figure 2.5 further show that the precise response of the system to the incoherent pumping can be controlled by varying the coupling field Rabi frequency g_{42}. In particular, stronger coupling fields g_{42} may be favorable, since then the range of possible slopes is increased, as can be seen from figure 2.5(b).

We now turn to a discussion of the non-resonant case, $\Delta_p \neq 0$, and focus on the regions with vanishing absorption, such as $\Delta_p \approx \pm 3.1 \times 10^{-4}\gamma$ in figure 2.4. It can be seen that around these probe field detunings, the imaginary part of the susceptibility vanishes, such that the probe field passes unattenuated through the medium. At the same time, the real part of the susceptibility is non-zero, and has a negative slope. Therefore, at these frequencies, superluminal or negative group velocities are accessible without absorption. In order to study this result in more detail, in figure 2.6(a) we show the probe field detuning Δ_0 at which the imaginary part of the susceptibility vanishes as a function of the incoherent pumping rate Λ. It can be seen that for no or small incoherent pumping Λ, there is always absorption such that no Δ_0 can be found. Once Λ is large enough for a root in the imaginary part of the susceptibility to occur, the position of the root first increases rapidly with Λ, and then saturates. The required value of Λ also depends on the strength

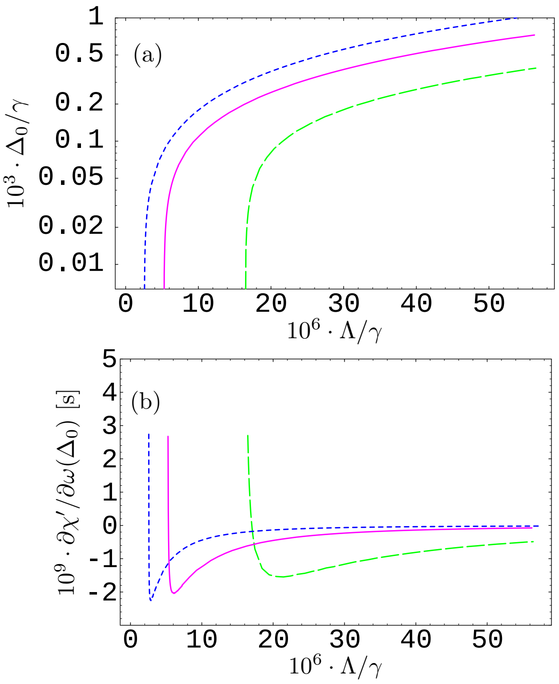

Figure 2.6: (a) Position Δ_0 of the root of the imaginary part of the susceptibility χ as a function of the pumping field strength Λ. At this frequency, light passes unattenuated through the medium. (b) Slope of the real part χ' of the susceptibility at the detuning Δ_0 with vanishing absorption. The parameters are as in figure 2.3 but with $g_{42} = 10\gamma$ (short-dashed blue), $g_{42} = 7\gamma$ (solid purple), and $g_{42} = 4\gamma$ (long-dashed green).

of the coupling field g_{42} as can be seen from figure 2.6(a).

The corresponding figure 2.6(b) depicts the slope of the real part of the susceptibility as a function of Λ. It can be seen that by varying the pump field strength Λ, both positive and negative slopes can be achieved at frequencies where the medium absorption is zero. After passing through a maximum positive slope, the slope drops to a minimum negative slope and then slowly increases again towards vanishing slope. For every value of the coupling field Rabi frequency g_{42}, optimum values of Λ can be identified where the slope is steepest and either positive or negative. The maximum absolute values of the slope are of order 10^{-9} s^{-1}, such that the term proportional to $\partial\chi'/\partial\omega$ in the denominator of equation (2.10) for our probe transition varies between approximately -10^7 and $+10^7$. Therefore, strongly sub- and superluminal propagation as well as a large range of negative group velocities occur without absorption in our sample, controlled by the magnitude of the incoherent pumping. It should be noted that only very weak incoherent pumping is required, as can be seen from the scaling of the x-axes in figures 2.6.

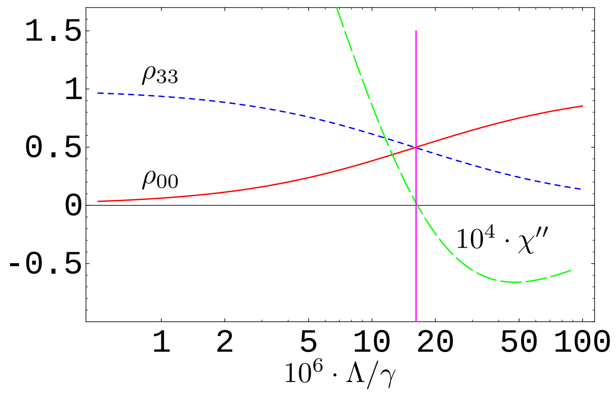

Figure 2.7: Populations of dressed state $\rho_{00} = \langle\, |0\rangle\langle 0|\,\rangle$ defined in equation 2.14a (solid red), bare state $\rho_{33} = \langle\, |3\rangle\langle 3|\,\rangle$ (short-dashed blue), and imaginary part of the susceptibility (long-dashed green) as a function of the pumping field strength Λ. The parameters are as in figure 2.3 with $\Delta_p = 0$. The vertical purple line indicates the transition from absorption to gain.

2.3.4 Dressed-state analysis

We now introduce the dressed states generated by the strong driving field acting on transition $|2\rangle \leftrightarrow |4\rangle$ and the coupling field acting on transition $|1\rangle \leftrightarrow |4\rangle$, in order to demonstrate the presence of interacting dark resonances due to the perturbing field with Rabi frequency g_{41} [105]. In the absence of the incoherent pump field, the dressed states are

$$|0\rangle = -\frac{g_{42}}{\sqrt{g_{41}^2+g_{42}^2}}\,|1\rangle + \frac{g_{41}}{\sqrt{g_{41}^2+g_{42}^2}}\,|2\rangle\,, \tag{2.14a}$$

$$|\pm\rangle = \frac{g_{41}}{\sqrt{2(g_{41}^2+g_{42}^2)}}\,|1\rangle + \frac{g_{42}}{\sqrt{2(g_{41}^2+g_{42}^2)}}\,|2\rangle \mp \frac{1}{\sqrt{2}}\,|4\rangle\,, \tag{2.14b}$$

with energies

$$\lambda_0 \;=\; 0\,, \qquad \lambda_\pm = \pm\hbar\sqrt{g_{41}^2+g_{42}^2}. \tag{2.15}$$

The two dressed states $|\pm\rangle$ correspond, in the limit of vanishing driving field g_{41}, to the usual Autler-Townes dressed components split by $2\hbar g_{42}$. The third dressed state $|0\rangle$ coincides in this limit with the bare state $|1\rangle$ and hence is decoupled from the fields. This is no longer so in the presence of a second weak driving field g_{41}. In this case the dressed state $|0\rangle$ contains an admixture of $|2\rangle$ and thus has a nonzero dipole matrix element with the state $|3\rangle$. As a result of this coupling, there are transitions between $|0\rangle$ and $|3\rangle$. In the bare state picture, these transitions correspond to three photon resonances $|1\rangle \rightarrow |4\rangle \rightarrow |2\rangle \rightarrow |3\rangle$ [105].

The transition from absorption to gain under the influence of the incoherent pump field Λ can be interpreted in terms of transitions between the different bare and dressed states. As explained above, the narrow double dark state resonance arises due to transitions from dressed state $|0\rangle$ to bare state $|3\rangle$. In figure 2.7, we show the populations of these two states together with the imaginary part of the susceptibility for parameters as in figure 2.3. The probe field detuning is chosen as $\Delta_p = 0$, i.e., we look at the center of the narrow structure. It can be seen that, as expected, virtually all population is in bare state $|3\rangle$ for vanishing pumping field. The reason for this is that the weak probe field can only transfer a very small amount of population into the other states. With increasing pumping field Λ, however, the population transfers out of state $|3\rangle$ into dressed state $|0\rangle$. The population in $|0\rangle$ dominates among the different dressed states because it contains a large contribution of bare state $|1\rangle$, which is populated by spontaneous emission, but emptied only by the weak perturbing field g_{41}. Together with this population transfer, the absorption decreases, until the imaginary part of the susceptibility vanishes where the populations of $|3\rangle$ and $|0\rangle$ are equal. A further increase of the incoherent pumping generates a population inversion on transition $|0\rangle \rightarrow |3\rangle$, such that the medium amplifies. Thus, the absorption or amplification properties of the narrow double dark resonance can be directly explained by the population difference between the initial and the final state. A modification of this difference via the incoherent pump field allows to control the medium absorption.

2.3.5 Doppler averaging

Finally, we discuss the influence of Doppler broadening on the results obtained so far. One might be tempted to judge that the narrow structure arising from the interacting dark resonances will be washed out if broadening is taken into account. In order to clarify this question, we averaged our results for the susceptibility over a Maxwellian velocity distribution (Eq. 1.23 of the atoms in order to simulate a Doppler broadened gas. The distribution is characterized by the mean absolute velocity of the atoms (Eq. 1.21). In the following numerical analysis, we assume a particle density of 10^{12} cm^{-3}. For mercury, this corresponds to a temperature of about 256 K [106], a mean velocity $v_m = 145.68$ m/s, and a Doppler width of 3.6 GHz. All laser fields are co-propagating in the same direction.

In figure 2.8(a), we compare the susceptibility with and without Doppler averaging for parameters as in figure 2.4(b). Without averaging, for this set of parameters the medium exhibits gain, and the real part of the susceptibility has positive slope around $\Delta_p = 0$. Moving away from the resonance, the real part approaches zero. A comparison with the averaged results shows that, interestingly, the width of the narrow double dark state resonance is largely unaffected by the broadening. But the averaged medium absorbs, and the slope of the real part of the susceptibility is negative. Away from the resonance, the real part tends to a positive value. It turns out that due to the Doppler broadening, the two wide resonances at $\Delta_p \approx \pm 4\gamma$ shown in figure 2.4(a) move together. This causes an increase of the baseline of the imaginary part of the susceptibility around $\Delta_p = 0$. It is possible to counter this effect by increasing the Rabi frequency g_{42}, which is responsible for most of the

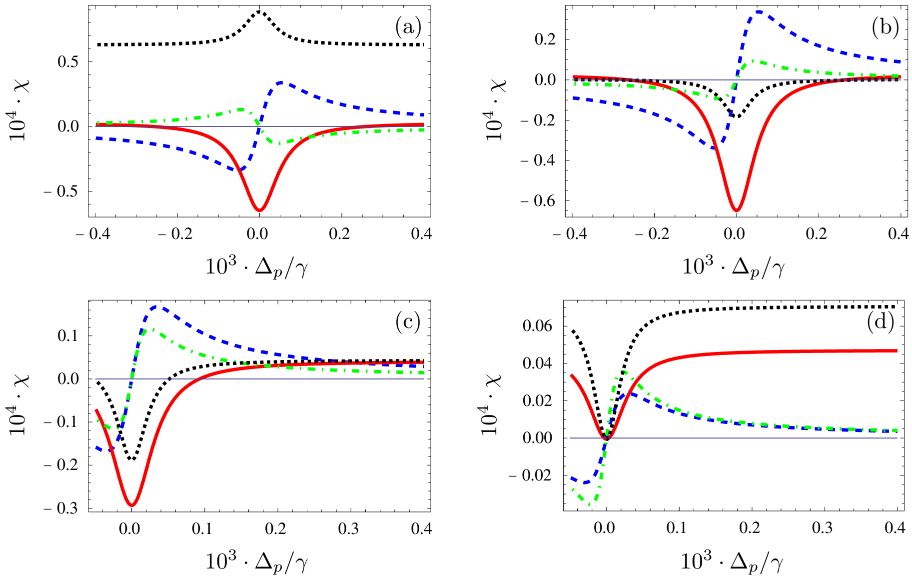

Figure 2.8: Doppler averaged susceptibilities. The particle density is 10^{12} cm^{-3}, which corresponds to a temperature of about 256 K. The short-dashed blue and the solid red curves are the real and imaginary part of unbroadened reference data. The dotted black and the dash-dotted green curve are corresponding Doppler averaged results. (a) Parameters are as in figure 2.4(b). (b) As in (a), but with $g_{42} = 12\,\gamma$ for the Doppler averaged susceptibility. (c) Reference: Parameters as in (a) except for $\Lambda = 21.0 \cdot 10^{-6}\,\gamma$, which corresponds to the largest negative slope of the corresponding long-dashed green curve in figure 2.6(b). The averaged curves are drawn for the same parameters except for $g_{42} = 8\,\gamma$. (d) Reference: Parameters as in (a) except for $\Lambda = 16.45 \cdot 10^{-6}\,\gamma$, which corresponds to the largest positive slope of the corresponding long-dashed green curve in figure 2.6(b). The averaged curves are drawn for the same parameters except for $g_{42} = 7.32\,\gamma$.

splitting of these two resonances. In figure 2.8(b), we show unbroadened curves as in subfigure (a) together with curves for the Doppler averaged case with $g_{42} = 12\,\gamma$. It can be seen that qualitatively similar results can be obtained in the averaged case simply by increasing g_{42}, even though in this particular case the magnitude of the response of the averaged medium is smaller than in the reference case. In subfigures (c,d), we turn to parameters where in the unaveraged case the slope of the real part of the susceptibility has maximum positive or negative values, as these are the most interesting points in terms of group velocity control. In (c), the parameters of the reference curves are as in (a), except for the incoherent pumping rate $\Lambda = 21.0 \cdot 10^{-6}\,\gamma$, which is the rate at which the largest negative slope is obtained for the corresponding long-dashed green curve in figure 2.6(b). The Doppler averaged curves are drawn for the same parameters except for an increase of g_{42} to $g_{42} = 8\,\gamma$, as explained above. It can be seen that, both for the averaged and the unaveraged case, the medium absorption vanishes at a certain probe field frequency together with negative dispersion of comparable slope. In (d), the parameters are as in (a) except for $\Lambda = 16.45 \cdot 10^{-6}\,\gamma$. At this pumping rate, the largest positive slope of the corresponding long-dashed green curve in figure 2.6(b) occurs. The averaged curves are drawn for the same parameters except for $g_{42} = 7.32\,\gamma$. For these parameters, comparable negative dispersion is achieved at the point of transparency.

In figure 2.8(d), the slope of the dispersion around the point of vanishing absorption is almost constant over a frequency range roughly given by the width of the narrow resonance. This is an important requirement in order to achieve undistorted pulse propagation through the medium [24]. The case of maximum negative dispersion in figure 2.8(c) has a small curvature of the dispersion in the transparency region. This curvature can be minimized by moving the transparency region to a suitable position via a change of the incoherent pump rate Λ.

It should be noted that we only modified the coupling field Rabi frequency g_{42} in order to recover large positive or negative dispersion without absorption depending on the applied incoherent pump rate Λ. This change was motivated by the need to compensate the shifting of the broad resonances due to the Doppler averaging. An additional optimization of the other system parameters may further improve the result. A different setup of the laser propagation directions was discussed in [105]. Experimental observations of narrow double dark resonances in Doppler broadened media were reported, e.g., in [107–109].

2.3.6 Numerical verification of the analytical results

Throughout this section, the figures 2.2-2.8 have been obtained from a numerical solution of the full density matrix equations (2.1a)-(2.1i). In the following, we verify our approximate analytical expressions, equations (2.2a)-(2.7), by a comparison to the exact numerical calculations. The result is shown in figure 2.9, where the solid red curves correspond to the approximate analytical solutions, whereas the blue dashed curves represent our numerical results. The approximate result equation (2.4) for the case without incoherent pump field is shown in comparison to the numerical data in figure 2.9(a,b). It turns out that in this case, the results from equation (2.4) are virtually identical to the corresponding numerical results. Equation (2.7) for the case with incoherent pumping is compared to the numerical results in figure 2.9(c,d). Here, the analytic results only describe the qualitative behavior of the curves. The reason for this is that in this figure, we chose parameters for which the condition $\Lambda \gg \Lambda_0$ in equation (2.6) is not well satisfied. If the incoherent pumping Λ is increased, the agreement of the approximate results with the numerical calculation improves. Thus we conclude that our analytical results describe the system well enough to allow for an optimization of the parameters towards a desired peak structure, as long as the conditions on the parameters are satisfied.

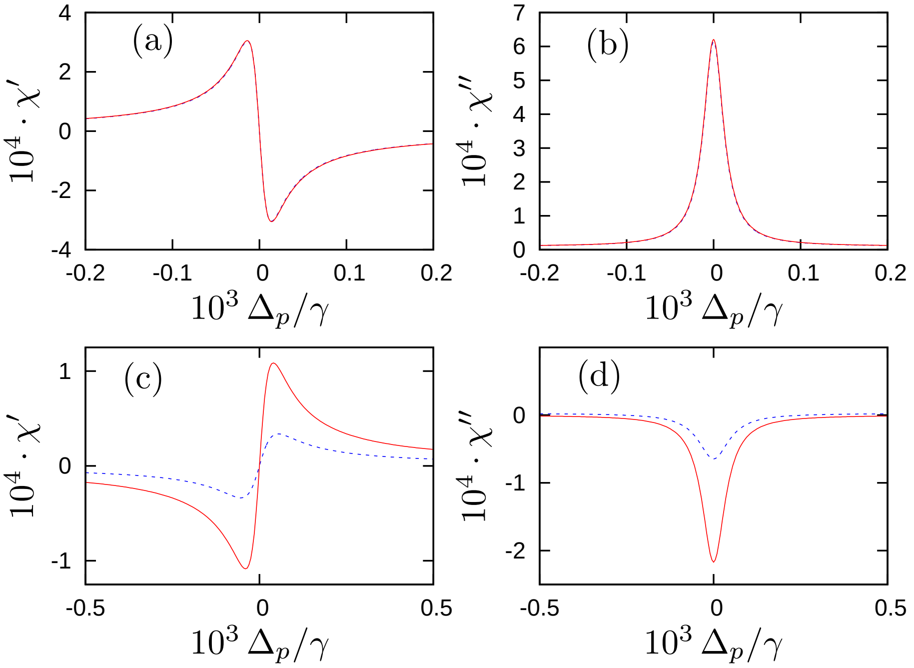

Figure 2.9: Real (a,c) and imaginary (b,d) parts of the susceptibility χ as a function of the probe detuning. The analytical results are shown as solid red lines, whereas our numerical results are shown as dashed blue lines. The parameters in (a,b) are as in figure 2.3, and equation (2.4) is shown as the analytical result. The parameters in (c,d) are as in figure 2.4, with equation (2.7) as analytical result.

2.4 Conclusion

We have discussed the dispersive and absorptive properties of a four-level atomic medium that exhibits interacting dark-state resonances. In our numerical analysis, we have focused on mercury atoms with an ultraviolet probe field wavelength of 243.7 nm. Due to the interacting resonances, a high-resolution structure appears in both the absorption and the dispersion spectra. A weak probe field tuned to this resonance usually experiences superluminal propagation with absorption. But if in addition a weak incoherent pump field is applied to the probe transition, then the superluminal light propagation changes to subluminal light propagation accompanied by no absorption or gain. Slightly off resonance, the probe field experiences a vanishing imaginary part of the susceptibility. At these off-resonant frequencies, the real part of the susceptibility itself is non-zero and has a slope depending on the incoherent pumping strength. Thus both sub- and superluminal light propagation as well as negative group velocities can be achieved without absorption. The control via the incoherent pump fields suggests potential applications, e.g., in optical switching devices or in controllable pulse delay lines for the ultraviolet frequency region.

Part II

Parametric processes and cooperative effects in light propagation

Chapter 3

Four-wave mixing enhanced white-light cavity

We discuss bandwidth enhancement of a cavity without reducing its maximum intensity buildup in a regime where the light propagation dynamics is crucial. The enhancement relies on a frequency-dependent phase compensation via negative dispersion provided by a coherently prepared atomic medium in the cavity. We analyze the spatiotemporal dynamics in such a white light cavity with a full simulation of the field propagation. We find that the probe field dispersion is in addition changed by a coherent field which is generated within the medium via four-wave mixing. Counter intuitively, this in-medium dynamics leads to a further enhancement of the cavity bandwidth.

3.1 Introduction

In an optical cavity, the bandwidth of supported frequencies and the intensity buildup are inversely proportional [110]. Increasing the cavity's finesse, e.g., via the reflectivity of the mirrors, leads to a higher buildup for a smaller range of frequencies and vice versa. The reason is that frequencies away from the cavity resonance correspond to different wavelengths which do not exactly fulfill the resonance condition. Thus, they acquire a phase shift with respect to the resonance frequency and experience loss at the mirrors. In terms of applications, this inverse dependence is a limiting factor for a number of schemes. Perhaps most prominently, gravitational wave detectors (GWD) aim at detecting tiny oscillations that ideally could be amplified by the power buildup in a high-quality cavity with large bandwidth [111]. To overcome this problem, the concept of a so-called white-light cavity (WLC) was developed [112]. Its basic idea is to employ a mechanism inside the cavity that cancels the phase shift for off-resonant frequencies, thereby improving the bandwidth of a cavity without the drawback of reducing its maximum buildup. In the case of GWD one could increase sensitivity without restricting detection bandwidth.

It may seem that the simplest implementation of a WLC would be to insert a pair of plain parallel gratings into the cavity such that their diffraction leads to a frequency dependent path length [113]. However, this scheme is not feasible because of the additional position dependent phase shift caused by diffraction at a grating [114].

A different implementation of WLC uses a medium with negative dispersion inside the cavity. In such a medium, phase shifts due to wavelength mismatch can be compensated by suitable phase shifts generated via a frequency-dependent index of refraction. Proposed systems include a strongly driven double-Λ system with incoherent pumping [112], a strongly driven two-level atomic resonance, and a Λ-system off-resonantly driven by two strong fields [115]. In the latter case, the negative dispersion occurs between two gain lines. This has also been used in an experiment to demonstrate negative group velocity [116], a closely connected phenomenon, and recently the first experimental demonstration of a WLC was accomplished in such a system [117]. In a different experiment the nonlinear negative dispersion occurring in a standard Λ-system at higher probe field intensities was used [118]. In this case, however, the cavity bandwidth becomes dependent on the probe field intensity. Complementary to the original WLC approach, recently a high-quality white-light cavity was demonstrated with a whispering gallery mode resonator [119], which relies on an effectively continuous mode spectrum, however, with rather low input and output coupling.

The experimental results show that the concept of a cavity bandwidth enhancement with a negative dispersion medium is promising. But whether a real benefit in applications beyond proof of principle will be possible with this concept will depend on the flexibility of the level scheme, scalability of its parameters, and the influence of competing or disturbing processes on the performance. Advancing to more complex level schemes than standard electromagnetically induced transparency (EIT) based setups motivated by the desire for better control over the WLC, however, typically leads to absorption in the probe or control field amplitudes throughout the propagation, severely degrading the performance in the required extended media.

In this chapter, we discuss such propagation effects in WLC media with strong control field absorption, and show that instead, the WLC bandwidth enhancement can be improved due to an electromagnetic field that is generated and sustained by the atomic medium itself via four-wave mixing (4WM). In particular, we study light propagation through an atomic four-level medium in double-Λ configuration as depicted in Fig. 3.1. The medium is prepared by two control fields coupling to the transitions $|1\rangle \leftrightarrow |3\rangle$ and $|2\rangle \leftrightarrow |4\rangle$, while the probe field is applied to the $|1\rangle \leftrightarrow |4\rangle$ transition. This configuration is well known to exhibit 4WM [58,120–122], resonantly enhanced to a high conversion efficiency by the double-Λ scheme. If the probe field is present, an additional field is generated within the medium on the transition $|2\rangle \leftrightarrow |3\rangle$ which in turn changes the probe field dispersion. This backaction of the probe field onto itself is a processes occurring during the propagation of the light through the medium and cannot be captured in a standard treatment in terms of a single atom susceptibility analysis. Also, the two coupling fields are absorbed

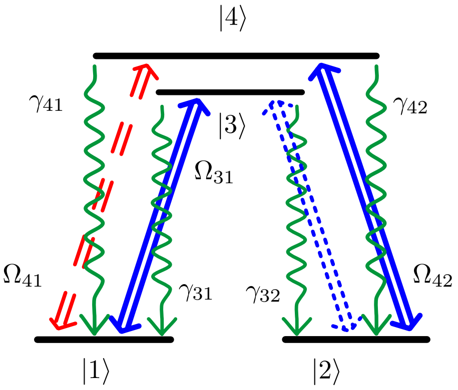

Figure 3.1: The considered double-Λ level scheme. Thick solid blue lines indicate strong continuous-wave driving fields. The probe field is shown as dashed red arrow. The dotted blue arrow represents a field generated within the medium via four-wave mixing. Ω_{jk} are Rabi frequencies. The spontaneous decays with rates γ_{jk} are denoted by the wiggly green lines ($j \in \{3,4\}$, $k \in \{1,2\}$).

such that their intensity changes substantially throughout the medium, at the same time preparing the medium in a position-dependent initial state. Therefore, apart from theoretical modelling, we numerically study the full propagation dynamics of all fields through the medium in order to determine their influence on the performance of a WLC.

The chapter is organized as follows. In the following section (Sec. 3.2), we review the resonance profile of an empty cavity. We explain the enhancement scheme for the cavity bandwidth and derive the condition for phase compensation in a white-light cavity. In Sec. 3.3, we then turn to the analysis of light propagation effects in our system. We discuss the relation of the phase-compensation condition to negative group velocity and study the influence of parametric processes on the propagation dynamics. Then, we define an effective medium susceptibility that includes all light propagation effects and can be calculated numerically. In the next section (Sec. 3.4), we present results for the effective susceptibility and the enhanced cavity bandwidth. Here, the influence of the 4WM process and its backaction on the probe field become apparent. We also discuss issues such as under- or overcompensation, influence of the transverse beam profile of the control fields, and the dependence of the enhancement factor on different initial cavity linewidth. Finally, we draw some conclusions regarding the implementation of our scheme (Sec. 3.5) and summarize our results.

3.2 Bandwidth of an optical cavity

3.2.1 Empty cavity

The resonance profile of an optical cavity is given by [110]

$$I = \frac{I_{max}}{1 + (2\mathcal{F}/\pi)^2 \sin^2(\varphi/2)}\,, \tag{3.1}$$

where $I_{max} = I_0/(1-r)^2$ is the maximum intensity buildup, $\mathcal{F} = \pi r^{1/2}/(1-r)$ is the cavity finesse, and $re^{i\varphi}$ is the round trip loss and phase shift. Without a medium the phase shift with respect to the resonance frequency is given by

$$\varphi_0 = \frac{2L\Delta}{c}\,, \tag{3.2}$$

with L the cavity length, $\Delta = \omega - \omega_0$ the detuning from the resonance frequency ω_0, and c the speed of light in vacuum. This phase shift leads to a cavity bandwidth (FWHM) of

$$\gamma_0 = \frac{\pi c}{L\mathcal{F}}. \tag{3.3}$$

3.2.2 White-light cavity condition

A medium of length $l < L$ and refractive index n inside the cavity leads to an additional phase shift

$$\varphi_1 = \frac{2l\omega_0}{c}(n-1)\,. \tag{3.4}$$

We assume that close to the resonance frequency n can be approximated as

$$n = 1 + \frac{n_g}{\omega_0}\Delta + n_3\Delta^3 + \mathcal{O}(\Delta^5)\,, \tag{3.5}$$

where $n_g = \omega_0 \frac{\partial n}{\partial \omega}\big|_{\omega_0}$ is the group index and $n_3 = \frac{1}{6}\frac{\partial^3 n}{\partial \omega^3}\big|_{\omega_0}$ is the third order correction term to a linear slope. The second and fourth order term vanish since the resonance frequency is an inflection point of the dispersion if probe field frequency and cavity resonance coincide. The condition for phase compensation $\varphi_0 + \varphi_1 = 0$ evaluates to (WLC condition)

$$n_g = -\frac{L}{l}. \tag{3.6}$$

Now the terms linear in frequency cancel and the enhanced cavity bandwidth is given by (FWHM)

$$\gamma_1 = \left(\frac{4\pi c}{l\omega_0 n_3 \mathcal{F}}\right)^{\frac{1}{3}}. \tag{3.7}$$

It is proportional to $n_3^{-1/3}$ which incorporates the width of the approximately linear part of the dispersion.

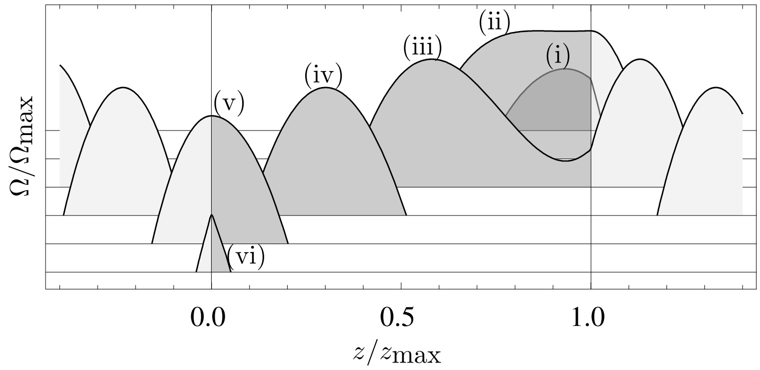

Figure 3.2: Peak of a probe field pulse for successive times (i)-(vi), scaled to the respective maximum in time. The peak leaves the medium before it enters and runs through the medium in reversed direction.

3.3 Light propagation effects

3.3.1 Relation to negative group velocity

From the WLC condition (Eq. 3.6) we see that a WLC requires a medium with negative group velocity. Therefore, in a first calculation, we propagate probe pulses of different bandwidths through the double-Λ medium and optimize parameters for a negative group index. For this, we derive the Maxwell-Schrödinger equations describing the light propagation through the medium using standard techniques [4], and solve the equations numerically on a grid using a Lax-Wendroff integration method [123]. We assume an $l = 0.3\,\mathrm{m}$ long medium with a density of $N = 6.6 \times 10^{15}\,\mathrm{m}^{-3}$ of Sodium atoms (optical depth ≈ 1) and initial control field strengths of $\Omega_{42} = 15.5\,\gamma$ and $\Omega_{31} = 16\,\gamma$. The weak probe field ($\Omega_{41} = 0.1\,\gamma$) is applied to transition $|1\rangle \leftrightarrow |4\rangle$.

For a Gaussian probe field envelope the peak of the pulse leaves the medium before it enters and runs through the medium in reversed direction (see Fig. 3.2). This behavior is typical for a medium with negative group velocity [116, 124]. From the advancement in time T_a of the pulse peak after passing the medium we calculate the group index, $n_g = -c\,T_a/l$.

3.3.2 Parametric processes

As we are most interested in propagation effects, we calculate the modification of the different field amplitudes throughout the medium. A typical evolution is shown in Fig. 3.3. The control fields are attenuated to about 60% of their initial value. At the same time, the control fields together with the probe field generate an additional field on the transition $|2\rangle \leftrightarrow |3\rangle$ via 4WM. This internally generated field and the externally applied fields form a closed interaction loop [36, 52], that in turn leads to light scattering into the probe field mode. By means of this backaction, the

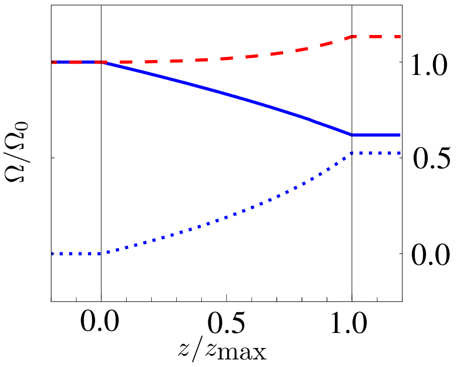

Figure 3.3: Attenuation or amplification of the control fields (solid blue line), probe field (dashed red line), and generated field (dotted blue line) over the medium. The generated field is scaled to the initial value of the probe field.

probe field dispersion is changed as we will see later. Furthermore, the probe field is amplified by about 10%, which allows to compensate for losses inevitable in an experimental realization.

3.3.3 Effective susceptibility

To evaluate the medium performance, in a second calculation, we extract the effective medium susceptibility by comparing amplitude and phase of a continuous wave probe field at the medium entry and exit after full numerical propagation, simulating an experimental measurement. For this, we relate the probe field at the medium exit $\Omega_{41}(l)$ to the initial field $\Omega_{41}(0)$ by

$$\Omega_{41}(l) = \Omega_{41}(0)e^{-kl\frac{\chi''}{2}}e^{ikl\frac{\chi'}{2}}, \tag{3.8}$$

where k is the respective wave number whereas χ' and χ'' are the real and imaginary part of the effective susceptibility. The obtained susceptibility describes a single pass of the probe field through the medium.

3.4 Results

3.4.1 Group index and effective susceptibility

Next, we discuss the results from the numerical analysis of the propagation dynamics. The group index and the effective susceptibility is shown in Fig. 3.4 against the probe field detuning. In addition to the case with full medium dynamics, we also show as dashed lines the corresponding susceptibility that is obtained if the medium backaction via 4WM and the closed-loop scattering is suppressed. This is achieved by artificially setting the generated field on transition $|2\rangle \leftrightarrow |3\rangle$ to zero throughout the numerical analysis. In the latter case, the effective susceptibility can perfectly

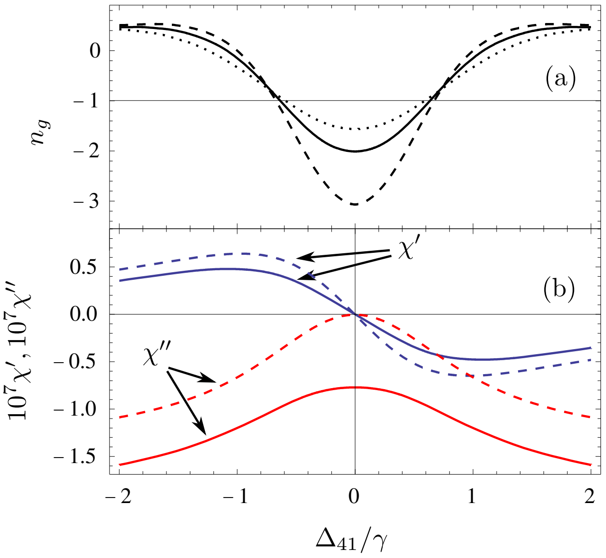

Figure 3.4: (a) Group index of a Gaussian probe pulse with bandwidth of 2γ (dotted line) and $\gamma/2$ (solid line). The dashed line shows bandwidth $\gamma/2$, but with field generation via 4WM suppressed. Bandwidth narrowing below $\gamma/2$ does not change the group index significantly. (b) Real part χ' (upper blue lines) and imaginary part χ'' (lower red lines) of the effective probe field susceptibility with (solid lines) and without (dashed lines) 4WM.

be explained by averaging the result of a single-atom analysis over the non-uniform control field intensities in the medium. In contrast, in the general case with 4WM and medium backaction present, a single-atom analysis combined with an averaging fails to give the correct results.

It can be seen from Fig. 3.4 that the probe field dispersion with 4WM has both smaller slope and group index than without backaction (Fig. 3.4 (a) and (b), solid lines). It may seem that a smaller group index deteriorates the bandwidth enhancement. But as long as the group index for a resonant pulse reaches values below $n_g = -1$, the WLC condition Eq. (3.6) can be fulfilled, if the ratio of medium length to cavity length is suitably adjusted. In our numerical calculation, we find $n_g \simeq -2$ which corresponds to a medium filling about half of the cavity.

3.4.2 Bandwidth enhancement

The results for the effective susceptibility show that the considered four-level medium is suitable to provide a negative dispersion for phase compensation in a WLC. In a quantitative example, we now calculate the cavity resonance profile including phase compensation by the medium. We assume a cavity finesse of $\mathcal{F} = 1000$ which corresponds to a mirror reflectivity of $r = 99.68\%$, and a cavity length of $L = 59.5\,\text{cm}$ for which the WLC condition is fulfilled in the case with 4WM. With 4WM suppressed,

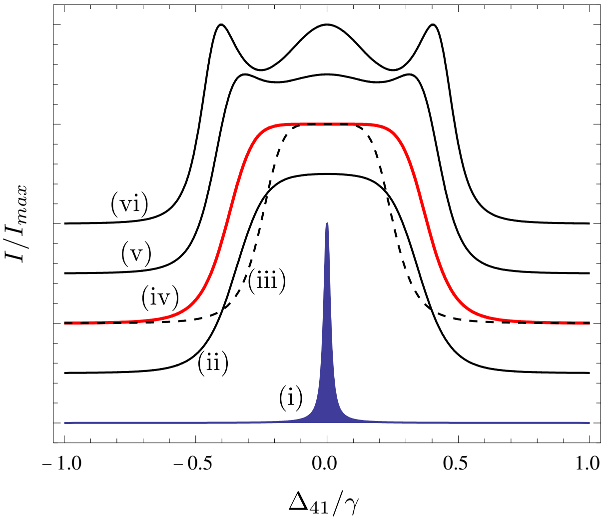

Figure 3.5: Intensity buildup for an $\mathcal{F} = 1000$ cavity without medium (i) and with the proposed WLC medium (iv). Curve (iii) shows the corresponding medium result with four-wave mixing artificially suppressed. The other three profiles show the general case with 4WM and a 2% (ii), a −2% (v), and a −4% (vi) mismatch of the cavity length with respect to the WLC condition. For better visibility the different profiles have been shifted by multiples of 0.25 with respect to each other. Profiles (iii) and (iv) have the same shift.

the negative group index is larger such that the WLC condition is violated for the same parameters. We compensate this by adjusting the medium length l suitably, but keep the cavity length L fixed such that the empty cavity bandwidth γ_0 remains equal. The corresponding cavity resonance profiles are shown in Fig. 3.5. Without 4WM, the cavity bandwidth is enhanced by about a factor of 20 (Fig. 3.5 (iii)). With 4WM, the enhancement is by a factor of about 30 (Fig. 3.5 (iv)). Thus, the in-medium dynamics enhances the desired bandwidth increase.

At the WLC condition, the enhanced bandwidth profiles become quadratically flat around the resonance frequency. Under- or overcompensating the frequency dependent phase shift leads to a less flat response, see Fig. 3.5. Similarly, the bandwidth enhancement depends on the control field intensity, and thus on the transverse distance x to the control field center axis. We assumed a Gaussian control field intensity profile with width σ_c and show the spatial enhancement variation in Fig. 3.6 (a). For comparison, intensity profiles of probe beams with widths $\sigma_c/3$ and $\sigma_c/10$ are shown as shaded areas. Full bandwidth enhancement is achieved up to about $x = 0.25\,\sigma_c$.

We also calculated the cavity bandwidth enhancement for different values of empty cavity bandwidth and for both cases, with and without 4WM. The result is shown in Fig. 3.6 (b) in a double-logarithmic plot. Both curves are indistinguishable from the theoretical power law $\gamma_1/\gamma_0 \propto (\gamma_0/\gamma)^{-\frac{2}{3}}$ that is evident from Eqs. (3.3) and

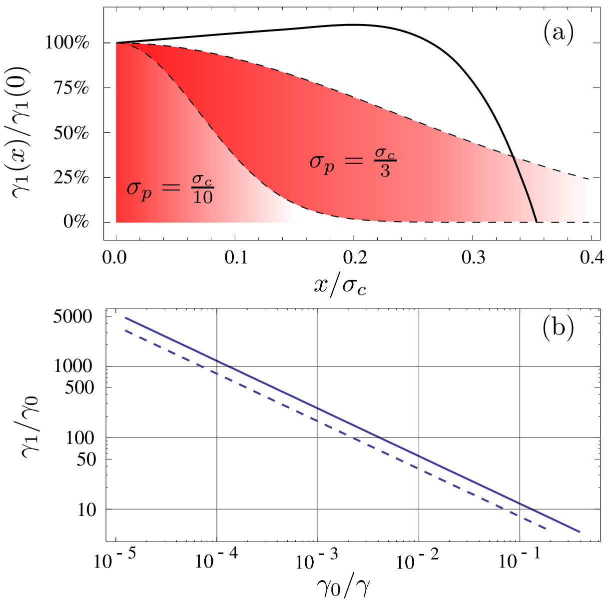

Figure 3.6: (a) Cavity bandwidth throughout a Gaussian transverse control field intensity profile with width σ_c (solid line). Shaded areas indicate probe beam intensity profiles with widths $\sigma_c/3$ and $\sigma_c/10$. (b) Enhancement factor with (solid line) and without (dashed line) the in-medium generated 4WM-field against empty cavity bandwidth γ_0.

(3.7). Again, in Fig. 3.6 (b), the bandwidth with full medium dynamics (solid line) is enhanced compared to the case without 4WM (dashed line).

From Fig. 3.6 (b), bandwidth enhancement factors above 10^3 are theoretically predicted for high quality cavities. This result, however, neglects practical issues common to light propagation setups with gases as follows. In an atomic gas medium suitable for the required phase compensation, typically Doppler effects need to be considered. In existing experiments (see, e.g., [116–118]), this issue could be overcome. As far as the propagation effects in our level scheme are concerned, the relevant processes are two-photon Raman transitions and four-photon closed-loop transitions. For these transitions the Doppler effect typically cancels to first order at the resonance frequency if the fields co-propagate. However, since the mechanism for a WLC relies on a frequency range around the resonance frequency, quantitative changes to our results can be expected. Second, an exact fulfilling of the WLC condition requires a stabilization of the different parameters such as the control field strengths and the cavity length. An accurate control of the cavity length e.g. via piezo elements could also be used to compensate fluctuations in the control field strengths. From Fig. 3.5(ii), (v), (vi) and Fig. 3.6 (a) it can be seen that a WLC condition mismatch on the few percent level typically is not critical.

3.5 Conclusion

As far as the application of a WLC in a GWD is concerned in principle the bandwidth enhancement factor should be directly convertible into a sensitivity enhancement of the same order. A question that has to be addressed, however, is how to actually implement a WLC into a GWD. Especially the larger scales of the cavity in the case of existing GWDs [111] consisting of the interferometer and a so-called signal recycling mirror pose a demanding task.

In summary, we have investigated a white-light cavity enhanced by in-medium propagation dynamics. The probe field generates an additional light field via four-wave mixing during the light propagation. The presence of the additional field in turn changes the probe field dispersion which leads to a further bandwidth enhancement.

Chapter 4

Phase modulation induced by cooperative effects in electromagnetically induced transparency

We analyze the influence of dipole-dipole interactions in an electromagnetically induced transparency setup for a density at the onset of cooperative effects. We show both analytically and numerically that the polarization contribution to the local field strongly modulates the phase of a weak pulse. We give an intuitive explanation for this local field induced phase modulation *and demonstrate that it distinctively differs from the nonlinear self-phase modulation a strong pulse experiences in a Kerr medium.*

4.1 Introduction

Electromagnetically induced transparency (EIT) stands out as one of the most useful coherence and interference phenomena (see [23, 24] and references therein). Current research focuses on dilute samples with $N\lambda^3 \ll 1$ (N density, λ transition wavelength), in which the atoms essentially act independently. Experimentally, an important reason for the restriction to low densities is detrimental decoherence induced, e.g., by atom collisions. This density restriction applies in particular to hot atomic vapors. More promising in this respect are ultracold gases [58, 109, 125–139], in which atomic collisions are much less frequent, leading to greatly improved coherence properties. However, most experiments still operate in the regime of a dilute gas, where cooperative effects do not play a role. But with recent advances in preparation techniques, now trapped ultracold gases at densities up to 10^{15} atoms/cm^3 with a linear extend of the gas in the μm range [137–139] have been reported. With such setups, dense gas light propagation experiments at the onset of cooperative effects seem within reach.

From the theoretical side, it is well-known that in the high density regime ($N\lambda^3 \gg 1$), a rigorous treatment of cooperative effects in general gives rise to an infinite hierarchy of polarization correlations [27, 140, 141]. Calculations of this type are demanding, such that concrete results for more complex model systems such as EIT have not been found yet. However, at the onset of cooperative effects, the infinite hierarchy can be truncated. A study of optical properties of a dense cold two-level gas found that in leading order of the density, three corrections with respect to a dilute gas occur [142]. First, the microscopic field E_{mic} driving the individual atom is no longer the externally applied field E_{ext} alone, but rather is corrected by the mean polarization P of the neighboring atoms. This local field correction (LFC) is described by the well-known Lorentz-Lorenz formula [143],

$$E_{mic} = E_{ext} + \frac{1}{3\epsilon_0} P \,. \tag{4.1}$$

The second correction in leading order of the density is due to the quantum statistics of atoms, and becomes relevant close to the phase transition to a Bose-Einstein condensate (BEC). The third correction arises due to the leading order of multiple scattering, which can be interpreted as a reabsorption of spontaneously emitted photons before they leave the sample. This radiation trapping [144–146] can be modeled as an additional incoherent pump rate, which for the case of EIT most dominantly affect the ground state coherence.

These results suggests that at the onset of cooperative effects, and at parameters away from the phase transition to BEC, the dominant cooperative correction arises from LFC, such that a macroscopic treatment is meaningful. Similar results were obtained in a recent calculation which for a two-level system explicitly compares a microscopic treatment based on a multiple-scattering approach including n-particle correlations with a macroscopic treatment based on LFC [147]. It was found that with densities of few particles per wavelength cubed ($N\lambda^3 \approx 5$), the two methods agree well, while at higher density ($N\lambda^3 \approx 124$) deviations occur, which however due to the numerical complexity could only be studied for rather small sample sizes. So far, LFC alone has been studied in a number of systems [148], including self-induced transparency [149], coherent population trapping [150] and lasing without inversion [151]. More recently, LFC was studied in the context of atomic gases with a negative refractive index (NRI) [21, 22, 32, 33, 152]. LFC effects have also been exploited to spectroscopically resolve the hyperfine structure of the Rb D_2 line in a dense gas [153].

But surprisingly, cooperative effects in EIT have received only little attention. In [144], effects of radiation trapping on EIT were studied. The propagation of two non-adiabatic propagating pulses is considered in [154]. Some effects such as a modification of the group velocity and a phase modulation are reported, but only numerical results are given without clear interpretation [1].

---

[1] Our results, however, do not show the dependence of the group velocity.

The recent theoretical proposals for NRI requiring high density already motivate a better study of the regime of higher densities in atomic gases. But also several aspects of EIT itself could benefit strongly from such an analysis. For example, the group velocity reduction in EIT and the related spatial compression of the pulse are directly proportional to the density [24]. Also, the time delay bandwidth product, a figure of merit for the overall performance of a slow light system, depends on density [155]. Finally, a higher density could facilitate a more efficient coupling of light and matter, e.g., for applications in quantum information science [156].

Therefore, we study light propagation in an EIT medium at the onset of cooperative effects, and reveal and interpret the underlying physical mechanisms. We show that LFC leads to a phase modulation of a probe pulse at densities achieved in current experiments. This phase modulation is distinctively different from nonlinear self phase modulation, as it leads to a linear frequency chirp across the whole probe pulse, and does not require high probe intensity. Our main aim is a physical understanding of the cooperative effects. For this, we include LFC, but assume parameters away from the crossover point to a Bose-Einstein condensate, such that corrections due to quantum statistics can be neglected. We further model the onset of multiple scattering via a modification of the EIT ground state decoherence rate. Under these approximations, we derive analytic solutions for the propagation dynamics of a slow light pulse and the medium polarization. All analytical results are verified with numerical solutions of the pulse propagation problem.

The chapter is organized as follows. In the following section (Sec. 4.2), we derive an analytical expression for the probe field susceptibility including LFC. From the probe field susceptibility, we find that LFC leads to a reshaping of the EIT transparency window. In the next section (Sec. 4.3), we then turn to the case of a slow light pulse. We derive an analytic solution for the propagation dynamics including the phase modulation the pulse experiences due to the influence of dipole-dipole interactions. In Sec. 4.4, we compare our analytic solution to results from a full numerical solution. We determine the scaling of the obtained phase modulation with density and decoherence. Based on our solution, we give an intuitive explanation of the phase modulation in terms of the energy exchange due to dipole-dipole interaction of neighboring atoms. In the end we compare our result to the nonlinear selfphase modulation a strong pulse obtains in a medium with an intensity dependent index of refraction. In Sec. 4.5 we summarize our results.

4.2 Susceptibility

4.2.1 Equations of motion including local field correction

We start from the well-known equations of motion (EOM) for an EIT system (see Fig. 4.1) [24]. In these equations, we replace the microscopic probe and control fields by their macroscopic counterparts using Eq. (4.1). Since the mean medium polarization P can be expressed in terms of a density matrix element, this leads to nonlinear EOM. Expanding the nonlinear EOM up to linear order in the external

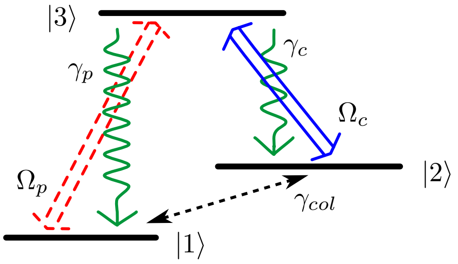

Figure 4.1: Probe (red dashed double arrow) and control field transition (blue solid double arrow)of the EIT system with Rabi frequencies Ω_p, Ω_c, decay rates γ_p, γ_c, and ground state decoherence γ_{col}.

probe field leaves us with just two EOM, one for the probe field coherence ρ_p and one for the Raman coherence ρ_r,

$$\partial_t\rho_p = -\Gamma_p\rho_p + \frac{i}{2}\Omega_p + \frac{i}{2}L\gamma_p\rho_p + \frac{i}{2}\Omega_c\rho_r\,, \tag{4.2a}$$

$$\partial_t\rho_r = -\Gamma_r\rho_r + \frac{i}{2}\Omega_c^*\rho_p\,. \tag{4.2b}$$

Here, $\Gamma_p = \gamma/2 - i\Delta_p$, $\Gamma_r = \gamma_{dec} - i\Delta$, $\Delta = \Delta_p - \Delta_c$, and $\gamma = \gamma_p + \gamma_c$ is the overall decay rate of the exited state. γ_{dec} is the ground state decoherence, and Ω_p, Δ_p, γ_p, Ω_c, Δ_c, γ_c are the Rabi frequency, the detuning, and the decay rate of the probe and control field transition. Due to LFC, a new term arises in Eq. (4.2a) as compared to the low-density case which is proportional to the dimensionless parameter

$$L = \frac{N\lambda^3}{4\pi^2}\,. \tag{4.3}$$

It is a measure for the strength of LFC, where a factor ensures that $L = 1$ corresponds to a density where the LFC induced frequency shift in a two-level atom is equal to half the natural linewidth. Formally, the new term can be interpreted as a frequency shift in an EIT system as well and can be included into the probe field detuning $\tilde{\Delta}_p = \Delta_p + L\gamma_p/2$. However, this frequency shift does not influence the two-photon detuning Δ. Solving for the steady state of Eqs. (4.2) leads to the following expression for the susceptibility χ,

$$\chi = \frac{3L\frac{\gamma_p}{2}(\Delta + i\gamma_{dec})}{\frac{\gamma}{2}\gamma_{dec} - \tilde{\Delta}_p\Delta + \frac{|\Omega_c|^2}{4} - i(\tilde{\Delta}_p\gamma_{dec} + \Delta\frac{\gamma}{2})}\,. \tag{4.4}$$

4.2.2 Transparency window

With an analytic expression at hand we can easily pinpoint the effect of LFC in the susceptibility. We find that a reshaping of the EIT transparency window takes place [150]. To illustrate this we show in Fig. 4.2 the real and imaginary part of χ for two different sets of parameters. In Fig. 4.2 (a) we set $L = 10^{-5}$ which results in

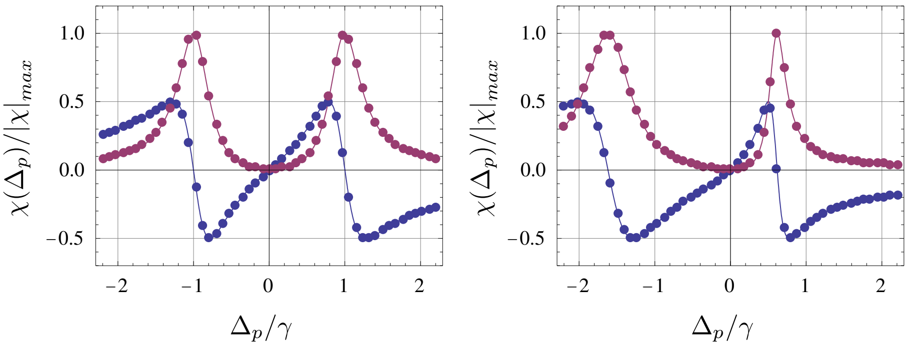

Figure 4.2: Real part (blue dashed line) and imaginary part (red solid line) of the EIT susceptibility given by Eq. 1.2.5 for (a) negligible LFC ($L = 10^{-5}$) and (b) strong LFC ($L = 4$). The small circles are numerically probed data (see text).

negligible LFC and the standart form of the EIT susceptibility is recovered. With $L = 4$ in Fig. 4.2 (b) a strong reshaping of the transparency window due to LFC is found. In both cases we set a control field Rabi frequency of $\Omega_c = 2\gamma$. To verify these results we also do a numerical integration of the full set of nonlinear EOM for EIT including LFC together with the wave equation and read off the attenuation and phase shift from a weak continuous wave probe field at the medium exit. This numerically probed susceptibility is shown as small filled circles in Fig. 4.2 and is in full agreement with the analytical form.

4.3 Pulse propagation dynamics

To analyze the influence on the propagation dynamics of a light pulse, we expand Eq. (4.4) around the center of the transparency window. From $k(\omega) = \omega[1 + \chi(\omega)]^{\frac{1}{2}}/c$, we find the frequency dependent wave number $k(\omega)$ up to second order in the probe field detuning. The solution for the positively rotating component of the probe field in Fourier space then follows from $E^{(+)}(z,\omega) = E^{(+)}(0,\omega)\exp[ik(\omega)z]$, where $E^{(+)}(0,\omega)$ is given by the initial condition and

$$k(\omega) = k_0 + i\frac{n_g\gamma_{dec}}{c} + \frac{\Delta_p}{v_g} + k_0(i\beta_1 + \beta_2)\Delta_p^2 + \mathcal{O}[\Delta_p^3]\,. \tag{4.5}$$

We neglected terms suppressed by a factor of $\gamma\gamma_{dec}/\Omega_c^2$, since $\gamma\gamma_{dec} \ll \Omega_c^2$ is required for low absorption, and of higher order in Δ_p. Each term in Eq. (4.5) can be clearly interpreted. k_0 is the wave number of the undisturbed carrier wave. The second term describes the decay due to the ground state decoherence γ_{dec} where $n_g = 3L\gamma_p\omega_0/\Omega_c^2$ is the group index and ω_0 is the probe field transition frequency. The third term leads to the reduced group velocity $v_g = c/(1+n_g)$. The fourth term is quadratic in Δ_p and thus associated with a change of width in the Fourier transformation of a Gaussian. The imaginary part proportional to $\beta_1 = 6L\gamma\gamma_p/\Omega_c^4$ leads to a broadening of the temporal width due to the finite spectral width of the transparency window. Finally, the real part proportional to $\beta_2 = 6L^2\gamma_p^2/\Omega_c^4$ results from LFC. Formally, it leads to an imaginary part in the temporal width which corresponds to a phase modulation of the pulse. When we assume a Gaussian pulse shape as the initial condition, the solution in the time domain can be obtained by Fourier transformation. Considering only the envelope defined by $E(z,t) = \frac{1}{2}\mathcal{E}(z,t)\exp[i(k_0 z - \omega_0 t)] + \text{c.c.}$, we find

$$\mathcal{E}(z,t) = \mathcal{E}_0 \frac{\sigma}{\tilde{\sigma}} \exp\left[-\gamma_{dec} z/v_g - (t - z/v_g)^2/(2\tilde{\sigma}^2)\right].$$

$\mathcal{E}_0$ and σ are the initial amplitude and temporal width. The LFC modified width after propagating a distance z is $\tilde{\sigma}^2 = \sigma^2 + 2k_0 z(\beta_1 - i\beta_2)$. The phase modulation can be well approximated by the parabola

$$\phi_{\text{LFC}}(t) = \frac{\beta_2 k_0 z}{\sigma^2}\left[1 - \frac{(t - z/v_g)^2}{\sigma^2}\right]. \tag{4.6}$$

4.4 Results

4.4.1 Numerical example

To compare our analytic solution to results obtained numerically, we chose parameters consistent with recent ultra cold gas setups [137–139]. We assume a medium with density $N \approx 10^{14}\text{cm}^{-3}$ and a length of $z \approx 40\mu\text{m}$. This corresponds to $N\lambda^3 \approx 50$ ($\lambda = 795\text{nm}$), and with a control field $\Omega_c = 2\gamma$, a probe pulse with initial width of $\sigma = 20/\gamma$ propagates a distance of $z = 150 v_g/\gamma$. Besides some broadening, the probe pulse is attenuated only by the ground state decoherence γ_{dec}. From results of a recent experiment with Rubidium atoms of density $N \approx 2\times10^{14}\text{cm}^{-3}$ in an anisotropic trap we estimate it to about 10^5 Hz [138]. This would attenuate the initial amplitude to about 67% over the chosen propagation distance. In Fig. 4.3(a) we show the propagated pulse together with the LFC induced phase modulation $\phi_{\text{LFC}}(t)$ and the corresponding instantaneous frequency defined by $\omega(t) = \omega_0 - \partial_t\phi_{\text{LFC}}(t)$. The numerical solution is virtually indistinguishable from the analytical one, and we only show the analytical solution. We see that the phase modulation has a negative parabola-like shape such that the instantaneous frequency is approximately linear over the total extend of the pulse.

4.4.2 Scaling of phase modulation

From our analytical results, we can determine the scaling of the LFC-induced phase modulation with the density and the ground state decoherence. As expected, the ground state decoherence attenuates the pulse as a whole. It thus restricts the maximum propagation distance, but otherwise does not influence the phase modulation. To determine the influence of the density, we calculated the phase shift at the center of the pulse assuming a density-dependent propagation length determined by a fixed

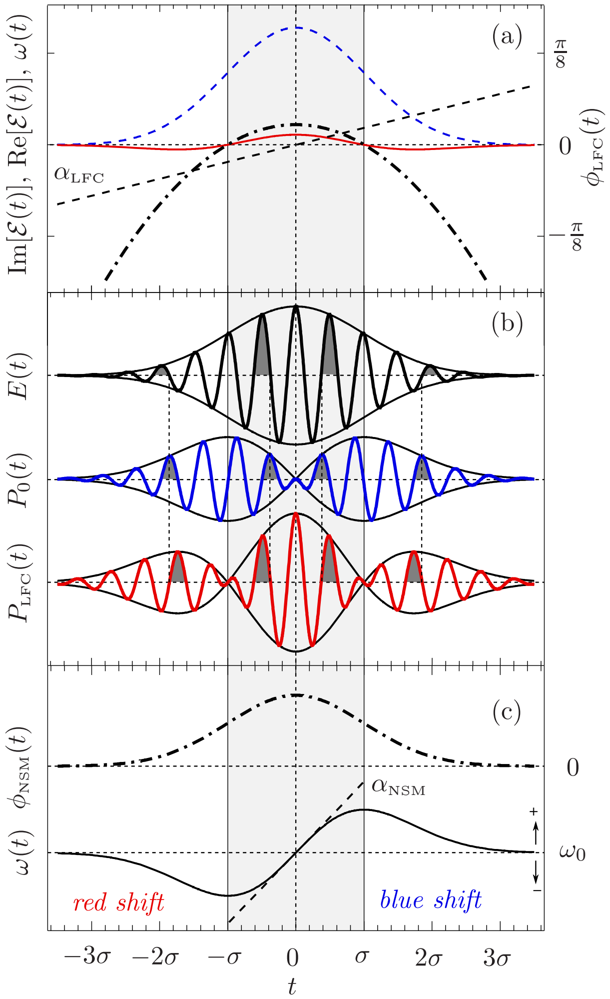

Figure 4.3: (a) Real part (blue dashed line) and imaginary part (red solid line) of a Gaussian pulse with LFC induced phase modulation. Both parts are scaled to arbitrary but equal units. The parabola (black dash-dotted line) shows the time dependent phase shift in radian measure (right axis) and the dashed straight line is the corresponding instantaneous frequency. It exhibits a linear frequency chirp with slope α_{LFC} over the total extend of the pulse. (b) Envelope and carrier wave of the pulse (black upper line), the polarization induced directly by the pulse (blue middle line), and the additional polarization induced by dipole-dipole interactions (red lower line). The amplitudes are not drawn to scale and the carrier wave length has been strongly exaggerated to make phase relations clearly visible. (c) The nonlinear self-phase modulation (black dash-dotted line) of a Gaussian pulse. The frequency chirp is approximately linear only in the pulse center (black dashed straight line) with slope α_{NSM}.

attenuation of the amplitude to $1/e$ of its initial value, and found a linear scaling with N:

$$\phi_{\rm LFC}^{\max} = \frac{N}{\gamma_{dec}} \frac{\lambda^3 \gamma_p}{2\pi^2 \sigma^2 \Omega_c^2} \,. \tag{4.7}$$

Thus at the onset of cooperative effects, the density and the ground state decoherence only affect the magnitude of the phase modulation. Since interferometric methods are very sensitive to phase changes, an experimental detection could already be possible at lower density and higher ground state decoherence.

4.4.3 Underlying mechanism of energy transfer

To explain the physical origin of the phase modulation, we explicitly calculate the relevant parts of the polarization using the relation $P^{(+)}(z,\omega) = \epsilon_0 \chi(\omega) E^{(+)}(z,\omega)$. Considering only the real part of χ up to quadratic order in Δ_p and Fourier transforming it into the time domain, we can distinguish two contributions,

$$P_0^{(+)}(z,t) = \frac{\epsilon_0 n_g}{\omega_0} \left[i\partial_t \mathcal{E}(z,t) \right] \exp[i(k_0 z - \omega_0 t)] \,, \tag{4.8a}$$

$$P_{\rm LFC}^{(+)}(z,t) = \epsilon_0 \beta_2 \left[i^2 \partial_t^2 \mathcal{E}(z,t) \right] \exp[i(k_0 z - \omega_0 t)] \,. \tag{4.8b}$$

The first contribution stems from the part linear in Δ_p and leads to the change of group velocity. The second contribution is due to the part quadratic in Δ_p which is related to the LFC induced phase modulation. In Fig. 4.3(b) we show the pulse together with these two contributions. In the first half of the pulse, $E(t)$ is ahead in phase by $\pi/2$ compared to $P_0(t)$, which indicates that energy is transferred from the pulse to the polarization $P_0(t)$. In the second half, the pulse is delayed by $\pi/2$, and energy is transferred back from the polarization $P_0(t)$ to the pulse. This energy exchange effectively reduces the group velocity of the pulse. Similarly, we can understand how the interaction of atoms with the collective dipole field of their neighbors proportional to $P_0(t)$ induces an additional polarization $P_{\rm LFC}(t)$. Before $t = -\sigma$, the polarization component $P_0(t)$ is $\pi/2$ ahead in phase compared to $P_{\rm LFC}(t)$, whereas at $-\sigma < t < 0$, it is delayed by $\pi/2$, again leading to an energy exchange. The same exchange takes place again for $0 < t < \sigma$ and $t > \sigma$. While the additional polarization $P_{\rm LFC}(t)$ is induced exactly by the same mechanism as $P_0(t)$, its back action on the probe pulse is different. At $t < -\sigma$ and $t > \sigma$, $P_{\rm LFC}(t)$ and $E(t)$ have opposite phase. This opposite phase has a dragging effect on $E(t)$, and reduces its phase. In the central part of the pulse ($-\sigma < t < \sigma$), $P_{\rm LFC}(t)$ is in phase with $E(t)$. This has a pushing effect on $E(t)$, and increases the phase of the pulse. This interpretation agrees with the phase modulation obtained from the calculation as shown in Fig. 4.3(a). We thus conclude that energy is exchanged between the atomic dipoles and the field of neighboring dipoles in exactly the same way as between the atomic dipoles and the external field $E(t)$. But the two polarization components act differently on the probe pulse, leading to the group velocity change and the phase modulation, respectively.

4.4.4 Comparison to nonlinear self-phase modulation

Finally, we compare the LFC induced phase modulation with nonlinear self-phase modulation (NSM) in a medium with an intensity dependent refraction. The NSM modulation is

$$\phi_{\mathrm{NSM}}(t) = n_2\, I(t)\, k_0\, z\,, \tag{4.9}$$

where n_2 is the intensity dependent index of refraction and $I(t)$ the intensity profile of the pulse. In Fig. 4.3(c) we show $\phi_{\mathrm{NSM}}(t)$ together with the corresponding instantaneous frequency for a Gaussian pulse. We see that the front of the pulse experiences a red shift whereas the back experiences a blue shift with an approximately linear frequency chirp in the center. Comparing the two chirps,

$$\alpha_{\mathrm{NSM}} = 2n_2 I_0 k_0 z/\sigma^2\,, \qquad \alpha_{\mathrm{LFC}} = 2\beta_2 k_0 z/\sigma^4\,, \tag{4.10}$$

we find that in the LFC case, $n_2 I_0$ is replaced by β_2/σ^2. Thus, the LFC modulation does not require a large intensity, and is approximately linear over the total extend of the pulse since it depends on the strength of the dipole-dipole interaction. This strength is given by β_2 in an EIT system and can be influenced by the density and the control field strength Ω_c.

4.5 Conclusion

In summary, we studied light propagation in an EIT system for densities at the onset of cooperative effects. We found a local field induced phase modulation that is distinctively different from non-linear self phase modulation, as it is linear across the whole pulse, and does not depend on the pulse intensity. The combination of analytical and numerical results enabled us to interpret the underlying physical mechanisms of the propagation dynamics.

Part III

Cross coupling of electric and magnetic laser field component: Chiral media

Chapter 5

Light propagation in chiral media

Light propagation in chiral media is discussed. We define chiral media in terms of a macroscopic electrodynamic description. Then, we derive the wave equations for a probe field propagating through a chiral medium, and solve them analytically in Fourier space using the slowly-varying envelope approximation. Our analysis reveals the influence of the different medium response coefficients on the propagation dynamics. Based on these results, we discuss conditions for a possible implementation.

5.1 Introduction

Quantum optics describes the interaction of matter and light at the quantum level [4, 5]. In many cases, the underlying principles can already be understood from a fairly simple analysis, focusing on single atoms interacting with the electric field component of the driving laser fields. But recently, motivated by the aim of achieving a negative index of refraction in atomic media [21, 22, 32, 33, 152], a qualitatively different class of setups received a considerable amount of interest. The key feature of these setups is that a probe beam interacts with the medium both with its electric and its magnetic field component at the same time. Only if both the magnetic and the electric response are suitable, a negative refractive index (NRI) can be achieved. Related to the need for a high magnetic response, these systems have two more distinct features in common. First, they operate at a high density, such that the different atoms in the medium are no longer independent [27, 140, 142]. Second, in order to enable a certain enhancement mechanism for the magnetic response, the laser fields couple to the medium in such a way that the system becomes chiral [30, 32, 157]. Unfortunately, an experimental implementation of these schemes to achieve atomic NRI media is very challenging. For example, suitable atomic species are rare, the required high density implies a number of problems such as Doppler broadening, radiation trapping [144, 145], dephasing or unwanted non-linear processes.

It is important to note, however, that these challenges to a large degree arise from the specific requirements for NRI media. But the two key ingredients, high density and chirality, are of interest in their own rights. This raises the question whether it is possible to study the effects of density or chirality individually at much more accessible parameter ranges. It turns out that the answer is affirmative. Regarding experiments at high density, we have see an example in chapter 4, where we studied dipole-dipole interactions in an electromagnetically induced transparency setup. Here, we turn to the second key ingredient of NRI schemes, and analyze light propagation in a sample of chiral atoms. Quantum optical setups routinely neglect the magnetic field components of the applied electromagnetic fields altogether. Generally, this is justified due to the weak interaction strength, and since magnetic transitions are typically off-resonant from the applied fields. Interestingly, a complete switch from electric to magnetic dipole transitions would not change the obtained results qualitatively, as the structure of the system Hamiltonian is essentially unchanged. It is only the combination of magnetic and electric field interactions in a chiral setup that gives rise to different results.

The chapter is structured as follows. First, in Sec. 5.2, we define and analyze chiral media in terms of parity transformations, and discuss their linear response. The following Sec. 5.3 analyzes light propagation in chiral media. In particular, we setup wave equations for the electric and magnetic field component, and we analytically solve these equations in slowly varying envelope approximation (SVEA). The last Sec. 5.4 discusses possible implementations of chiral media in atomic systems.

5.2 Chiral cross coupling

An object is defined to be chiral if it cannot be brought into coincidence with its mirror image. This implies the absence of any rotation-reflection symmetry axis and the object cannot be invariant under parity transformation. Since classical electrodynamics is is known to be a parity invariant theory, the question arises how chirality manifests itself in the electrodynamic description of a medium.

As a basis for our following analysis, we start from the two inhomogeneous macroscopic Maxwell's equations [3],

$$\nabla \times \mathbf{E} = -\partial_t \mathbf{B}\,, \tag{5.1a}$$

$$\nabla \times \mathbf{H} = \partial_t \mathbf{D}\,, \tag{5.1b}$$

with the electric field $\mathbf{E}$, the magnetic field $\mathbf{B}$, the electric displacement field $\mathbf{D}$, and the magnetizing field $\mathbf{H}$. The medium is described by its polarization $\mathbf{P}$ and magnetization $\mathbf{M}$, which are related to the quantities entering the Maxwell's equations via the constitutive relations

$$\mathbf{D} = \varepsilon_0 \mathbf{E} + \mathbf{P}\,, \tag{5.2a}$$

$$\mathbf{H} = \frac{1}{\mu_0}\mathbf{B} - \mathbf{M}\,. \tag{5.2b}$$

Due to the used SI unit system, the permittivity ε_0 and the permeability μ_0 of free space occur. We do not consider the two homogeneous Maxwell's equations since with no external sources or currents and assuming transverse fields they are always fulfilled.

Since **E**, **P**, and **D** are polar vectors they change sign under a parity transformation. In contrast, **B**, **M** and **H** are unchanged, because they are axial vectors. Together with the sign change of the curl operator, this shows the invariance of Maxwell's equations Eqs. (5.1) as well as the constitutive relations Eqs. (5.2) under parity transformation. Assuming a homogeneous isotropic medium, we can define linear electric and magnetic susceptibilities χ_E and χ_H,

$$\mathbf{P}(t) = \int \varepsilon_0 \chi_E(\tau)\mathbf{E}(t-\tau)\mathrm{d}\tau\,, \tag{5.3a}$$

$$\mathbf{M}(t) = \int \chi_H(\tau)\mathbf{H}(t-\tau)\mathrm{d}\tau\,. \tag{5.3b}$$

These equations only relate quantities of the same, odd or even parity and we see that the coefficients χ_E and χ_H are scalars and thus unaffected by a parity transformation. From the perspective of an electrodynamic description, the corresponding medium cannot be chiral. A different situation arises, if a medium also exhibits cross couplings in a way that an electric field induces magnetization and a magnetizing field induces polarization. In that case Eqs. (5.3) have to be extended by two extra terms,

$$\mathbf{P}(t) = \int \varepsilon_0 \chi_E(\tau)\mathbf{E}(t-\tau) + \frac{1}{c}\xi_{EH}(\tau)\mathbf{H}(t-\tau)\mathrm{d}\tau, \tag{5.4a}$$

$$\mathbf{M}(t) = \int \chi_H(\tau)\mathbf{H}(t-\tau) + \frac{1}{c\mu_0}\xi_{HE}(\tau)\mathbf{E}(t-\tau)\mathrm{d}\tau, \tag{5.4b}$$

with the cross coupling coefficients ξ_{EH}, ξ_{HE}, and $c = 1/\sqrt{\varepsilon_0\mu_0}$ the speed of light in vacuum. Under a parity transformation, the cross coupling coefficients ξ_{EH} and ξ_{HE} must change sign, because of the different transformation properties of **P** and **H** in Eq. 5.4a and **M** and **E** in Eq. 5.4b. In contrast to χ_E and χ_H, they have pseudo-scalar character. With non-vanishing cross couplings the medium properties change under parity transformation such that this extended description can account for a chiral medium.

In Eqs. (5.4), we have assumed that the medium and light field configuration are such that the response coefficients are (pseudo-) scalar rather than tensorial as it is the case in general. It turns out that this is possible, e.g., if the probing light field is circularly polarized in the $x-y$ plane and propagates in $\pm z$ direction [32,33]. This configuration allows for a different perspective on chirality. A circularly polarized light wave is a chiral object itself, and a left circularly polarized light wave under parity transformation is mapped onto a right circularly polarized light wave and vice versa. Because of global parity invariance of electrodynamics, considering a medium interacting with a right circularly polarized light wave is equivalent to considering the inverted medium interacting with a left circularly polarized light wave. It follows that a chiral medium must have a different response to a left and right circularly polarized light wave. This difference manifests itself in the refractive index, which in a medium with response as in Eq. (5.4) was shown to evaluate to [32]

$$n_{\pm} = \sqrt{\varepsilon\mu - \frac{1}{4}(\xi_{EH} + \xi_{HE})^2} \mp \frac{i}{2}(\xi_{EH} - \xi_{HE})\,. \tag{5.5}$$

Here, $\varepsilon = 1 + \chi_E$ and $\mu = 1 + \chi_H$. The upper sign applies for left circularly polarized light and the lower sign for right circularly polarized light. We see that in Eq. (5.5) it is equivalent to change the sign due to selecting a different polarization or to change the sign of ξ_{EH} and ξ_{HE} due to inverting the medium. Nonzero cross coupling coefficients ξ_{EH} and ξ_{HE} in both cases can account for the chirality of the medium.

5.3 Light propagation in chiral media

In this section, we derive the wave equations for the electric and magnetic field components of a probe field propagating through a chiral medium. This is in contrast to the usual treatment in which a coupling to only the electric component is assumed. We apply SVEA in order to transform the second order wave equations to equations involving first order derivatives only. Using Fourier transformation techniques, we find the general solution to the first order wave equations, and compare the result to the index of refraction obtained from a single particle susceptibility analysis.

5.3.1 Wave equation for the electric and magnetic field component

From Eqs. (5.1) and (5.2), we can derive wave equations for $\mathbf{E}$ and $\mathbf{B}$ with sources described by $\mathbf{P}$ and $\mathbf{M}$ as,

$$\left[\Delta - \frac{1}{c^2}\partial_t^2\right]\mathbf{E} = \mu_0\partial_t^2\mathbf{P} + \mu_0\partial_t\nabla\times\mathbf{M}, \tag{5.6a}$$

$$\left[\Delta - \frac{1}{c^2}\partial_t^2\right]\mathbf{B} = \mu_0\Delta\mathbf{M} - \mu_0\partial_t\nabla\times\mathbf{P}. \tag{5.6b}$$

In the following, we specialize to the case of a one-dimensional propagation. We choose the positive z axis as the propagation direction and separate a complex envelope function $X_0(z,t)$ from the carrier wave,

$$\mathbf{X} = \frac{1}{2}X_0(z,t)\mathbf{e}_{\pm}e^{i(k_0 z - \omega_0 t)} + \text{c.c.}, \tag{5.7}$$

where $\mathbf{X}$ stands for $\mathbf{E}$, $\mathbf{B}$, $\mathbf{P}$, or $\mathbf{M}$. The complex unit vector for left or right circular polarized light is $\mathbf{e}_{\pm}$, and the wave number of the carrier wave in vacuum is k_0 with $\omega_0 = ck_0$ as the corresponding frequency. Assuming that variations in space and time of the envelope function are on a much larger scale than the wavelength $\lambda_0 = 2\pi/k_0$

and the oscillation period $T_0 = 2\pi/\omega_0$ of the carrier wave, we can apply the slowly varying envelope approximation (SVEA) [4]. In this approximation derivatives of the envelope function in space and time are neglected compared to derivatives of the carrier wave. As a consequence, SVEA reduces the wave equations Eqs. (5.6) to first order equations for the envelope functions,

$$\left[\partial_z + \frac{1}{c}\partial_t\right] E_0(z,t) = \frac{ik_0}{2\varepsilon_0} P_0(z,t) \mp \frac{k_0}{2\varepsilon_0 c} M_0(z,t)\,, \tag{5.8a}$$

$$\left[\partial_z + \frac{1}{c}\partial_t\right] B_0(z,t) = \frac{ik_0\mu_0}{2} M_0(z,t) \pm \frac{k_0}{2\varepsilon_0 c} P_0(z,t)\,. \tag{5.8b}$$

As before and in the following, the upper sign applies for left circular polarization whereas the lower sign applies for right circular polarization. Eqs. (5.8) are considerably simpler to solve analytically as well as numerically than the second order Eqs. (5.6) we derived initially . Yet, they still incorporate the essential physics of light propagation in one dimension for a chiral medium with a coupling to both the electric and the magnetic component of a weak probe field.

5.3.2 Solution of the wave equations

We will now solve the wave equations (5.8) in SVEA to a level that enables us to determine how the actual propagation dynamics depends on the four quantities χ_E, χ_H, ξ_{EH}, and ξ_{HE} characterizing the medium. First, we transform Eqs. (5.8) into Fourier space. To substitute P_0 and M_0 we also Fourier transform Eqs. (5.4) and to replace H_0 by B_0 we use the Fourier transform of Eq. (5.2b). Finally, we can combine both wave equations into a single matrix equation for the vector $\mathbf{F}(z,t) = (E_0(z,t), cB_0(z,t))^T$,

$$\partial_z\,\mathbf{F}(z,\Delta_p) = ik_0\,\mathcal{M}\,\mathbf{F}(0,\Delta_p)\,, \tag{5.9}$$

and the elements of the matrix $\mathcal{M}$ are given by

$$\mathcal{M}_{1,1} = \frac{\Delta_p}{\omega_o} + \frac{1}{2\mu}(\chi_E - \xi_{EH}\xi_{HE} \pm i\xi_{HE})\,, \tag{5.10a}$$

$$\mathcal{M}_{1,2} = \frac{1}{2\mu}(\xi_{EH} \pm i\chi_H)\,, \tag{5.10b}$$

$$\mathcal{M}_{2,1} = \frac{1}{2\mu}(\xi_{HE} \mp i\mu\chi_E \pm i\xi_{EH}\xi_{HE})\,, \tag{5.10c}$$

$$\mathcal{M}_{2,2} = \frac{\Delta_p}{\omega_0} + \frac{1}{2\mu}(\chi_H \pm i\xi_{EH})\,. \tag{5.10d}$$

In these equations, the detuning $\Delta_p = \omega - \omega_0$ accounts for the frequency distribution of the envelope functions around the carrier frequency. Applying the vacuum phase relation for circular polarized light, $cB_0 = \mp iE_0$, we find that the initial condition for the evolution Eq. (5.9),

$$\mathbf{F}(0,\Delta_p) = \begin{pmatrix} E_0(0,\Delta_p) \\ \mp iE_0(0,\Delta_p) \end{pmatrix}\,, \tag{5.11}$$

is an eigenvector to matrix $\mathcal{M}$ in Eq. (5.9). Therefore, the solution can be calculated with the help of the corresponding eigenvalue η. The solution reads

$$\mathbf{F}(z, \Delta_p) = e^{ik_0\eta z} \begin{pmatrix} E_0(0, \Delta_p) \\ \mp i E_0(0, \Delta_p) \end{pmatrix} , \tag{5.12}$$

and the frequency dependence is contained in the eigenvalue

$$\eta = \frac{\Delta_p}{\omega_0} + \frac{1}{2\mu} \left[\chi_E \, \mu + \chi_H - \xi_{EH}\xi_{HE} \mp i(\xi_{EH} - \xi_{HE}) \right] . \tag{5.13}$$

This result can be compared to the refractive index Eq. (5.5) in a chiral medium obtained from a single-particle susceptibility analysis. The application of SVEA is equivalent to the condition $|n_\pm - 1| \ll 1$, such that we can perform a first order Taylor expansion of the square root contribution in Eq. (5.5). Keeping terms linear in the response coefficients we find

$$n_\pm = 1 + \frac{1}{2}(\chi_E + \chi_H) \mp \frac{i}{2}(\xi_{EH} - \xi_{HE}) . \tag{5.14}$$

Linearizing Eq. (5.13) and taking into account the contribution of the carrier wave, we find the same result as in Eq. (5.14). This demonstrates the consistency of our solution with the previously calculated chiral index of refraction. Our result based on the solution of the wave equations, however, has the advantage that it offers the possibility to study propagation dynamics. Because of the simple formulas we have derived, analytical solutions become accessible. If for a specific system the frequency dependencies of χ_E, χ_H, ξ_{EH}, and ξ_{HE} are known, it can be used together with the solution in frequency domain Eq. (5.12) to calculate the actual dynamics in time domain.

5.4 Prerequisites for a chiral atomic medium

In this section we discuss the general conditions for realizing a chiral atomic medium in the form as introduced in Sec. 5.2. As a first condition, a medium in addition to an electric probe field transition should exhibit a near-degenerate transition coupling to the magnetic component of the probe field. A second condition is that, to enable chiral cross couplings, there must be a mechanism to allow for polarization [magnetization] to be induced by the magnetic [electric] probe field component.

The first condition can be difficult to fulfill in atomic media. A small frequency difference between electric and magnetic probe field transition could be removed by an external magnetic field leading to a Zeeman shift, but magnetic dipole transitions are usually found in a much smaller frequency range compared to electric dipole transitions. The reason is that due to selection rules imposed by the corresponding transition matrix element, magnetic dipole transitions can only occur between states of the same parity. This implies that magnetic dipole transitions only take place between states with the same angular momentum quantum number whereas electric dipole transitions connect states of different angular momentum. A possible solution are atomic species with a large spin-orbit coupling [39]. Then, states with the same angular momentum quantum number can display a large splitting and their transition frequency can become comparable to the transition frequency of an electric dipole transition. This could also help to realize a probe field transition frequency in the optical domain which is especially attractive for applications. Motivated by ideas like NRI, several atomic species have been investigated with respect to this condition. Dysprosium [32, 158], Hydrogen [22], metastable Neon and other noble gases [22,159] have been identified as promising candidates. An alternative approach could be to make use of non-resonant two-photon transitions in order to relax the requirement of having both electric and magnetic transitions at similar transition frequencies [33, 159].

The second condition can be implemented in closed-loop systems. In these systems the laser-driven transitions form a closed interaction contour such that photon emission and absorption can take place in a cycle [36, 37]. Because the closed interaction contour enables quantum mechanical pathway interference, it can render the system phase dependent. Closed-loop systems have mainly been investigated in non-chiral contexts [46, 48, 50, 51, 53–55]. Here, the closed interaction contour only includes the coupling to one (electric) probe field component. This is known to induce extra contributions to the medium response, but these cannot be utilized for light propagation of a pulsed probe field in a straightforward way. As we have seen in the first chapter, already without the probe field, such a configuration would give rise to parametric processes which scatter the control fields into the probe field mode [45,47,49,52]. We will see in the next chapter that this conclusion changes in the case of chiral closed-loop systems. There, we will find that the closed-loop phase can provide a convenient control parameter for light propagation in chiral media.

5.5 Conclusion

We defined and analyzed chiral media in terms of parity transformations, and discussed their linear response. Next, we derived wave equations for both the electric and the magnetic field component in a chiral medium, and using the slowly varying envelope approximation solved these equations in Fourier space. The solution elucidates the actual dependence of the propagation dynamics on the direct and chiral response functions in a macroscopic electrodynamic description. Based on these results, we discussed the general conditions necessary for realizing a chiral atomic medium.

Chapter 6

Chiral control of propagation dynamics

We study an explicit example for light propagation in chiral media. Applying the results from the previous chapters, we show that chiral interactions already become important at experimentally accessible parameter ranges in dilute vapors. The chirality renders the propagation dynamics sensitive to the phase of the applied fields, and we show that this phase-dependence enables one to control the pulse evolution during its propagation through the medium. Our results demonstrate that the magnetic field component of a probe beam can crucially influence the system dynamics even if it couples to the medium only weakly.

6.1 Introduction

In this chapter we turn to a specific example for light propagation in chiral media and apply the results obtained in the previous chapter. The atomic medium is modeled as the five level system shown in Fig. 6.1. It was first introduced in the context of generating atomic media exhibiting a negative index of refraction [32]. We study the light propagation through this medium, and find that chiral interactions become relevant already at low medium density. The closed interaction loop gives rise to a sensitivity of the system dynamics to the relative phase of the applied fields. We show that this dependence can be used to control the propagation dynamics of a probe pulse, even throughout the pulse propagation. The results are interpreted based on our analytical solution, and all conclusions are verified using a full numerical solution of the propagation equations.

In a broader context, our results demonstrate that the magnetic field component of the probe field can crucially influence the propagation dynamics of the light pulse, even though it couples to the medium only very weakly. This may pave the way to further applications of *magnetic quantum optics*, utilizing both electric and magnetic components of the applied laser fields. Also, it will turn out that the analysis of

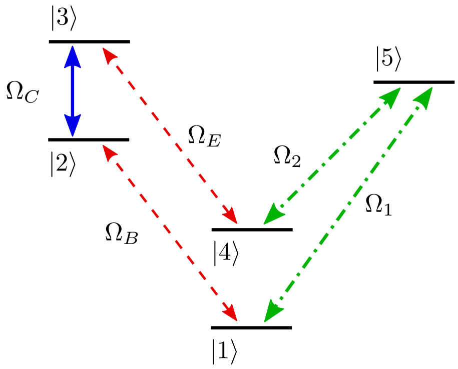

Figure 6.1: Atomic level scheme used to describe the chiral medium. Two strong control fields with Rabi frequencies Ω_1 and Ω_2 prepare a coherent superposition of states $|1\rangle$ and $|4\rangle$. The magnetic and electric probe beam components couple to two transitions with Rabi frequencies Ω_B and Ω_E, respectively. Ω_C describes an additional control field. The relative state parities are denoted by ±.

chiral media sheds light on the related so-called closed-loop systems [36,46]. We will find that chiral media are an ideal implementation of a closed-loop-phase control scheme of light propagation.

The chapter is organized as follows. First, in Sec. 6.2, we discuss our model system and derive analytic expressions for the medium response coefficients. Based on these results, we discuss pulse propagation of a slow light pulse, with the emphasis on phase control of the propagation dynamics (Sec. 6.3). Section 6.4 discusses and summarizes the results.

6.2 Model system

In zeroth order of the probe field, the atomic medium forms an effective three-level system in Λ-configuration consisting of states $|1\rangle, |4\rangle$ and $|5\rangle$. Two strong resonant control fields with Rabi frequencies Ω_1 and Ω_2 prepare the atoms in a dark state, i.e., a stable coherent superposition of states $|1\rangle$ and $|4\rangle$. The magnetic and electric probe field components couple to degenerate magnetic and electric dipole transitions with Rabi frequencies Ω_B and Ω_E, and the upper levels of these two dipole transitions are coupled by an additional resonant control field with Rabi frequency Ω_C. We assume that state $|1\rangle$ and $|4\rangle$ have the same parity. Because the electric probe field transition couples states of different parity whereas the magnetic probe field transition couples states of the same parity, the additional control field couples to an electric dipole transition. Note that the Rabi frequencies $\Omega_i = |\Omega_i| \exp[i(\vec{k}_i \vec{r} + \varphi_i)]$ are complex, and contain the wave vector $\vec{k}_i$ and the absolute phase φ_i $(i \in \{1, 2, C, E, B\})$.

6.2.1 Chiral enhancement of magnetic response

As discussed in Sec. 5.1, the linear response of the chiral atomic medium is characterized by two contributions. First, direct contributions arise from the polarization [magnetization] induced by the electric [magnetic] probe field component. It turns out that the direct contribution to the magnetic response is typically small. The reason is that magnetic dipole couplings usually are much weaker than electric dipole couplings,

$$m/d \sim \alpha c \quad \Rightarrow \quad |\Omega_B| \sim \alpha |\Omega_E| \,, \tag{6.1}$$

with magnetic dipole moment m, electric dipole moment d, and fine structure constant α. Therefore, in comparison to the direct electric response, the direct magnetic response is parametrically suppressed by two powers of the fine structure constant [38],

$$\chi_H \sim \alpha^2 \chi_E \,. \tag{6.2}$$

The other contributions to the medium response are cross couplings, which arise due to polarization [magnetization] induced by the magnetic [electric] probe field component. They lead to nonzero values for ξ_{EH} and ξ_{HE} and thus render the medium chiral. A magnetic response arising from such a cross coupling is only suppressed by one power of α [32, 38],

$$\xi_{EH} \sim \alpha \chi_E \quad \text{and} \quad \xi_{HE} \sim \alpha \chi_E \,. \tag{6.3}$$

Furthermore, it is proportional to the strength of the ground state coherence of state $|1\rangle$ and $|4\rangle$ and the control field Ω_C which allows for an additional enhancement proportional to the control field strength.

6.2.2 Phase dependence

The Hamiltonian of the system in Fig. 6.1 in a suitable interaction picture is given by [4]

$$\begin{aligned} H_I = &- \hbar \Delta_p (A_{22} + A_{33}) \\ &- \frac{\hbar}{2} \left(\Omega_B \, A_{21} + \Omega_E \, A_{34} + \Omega_C \, A_{32} + \Omega_1 \, A_{51} + \Omega_2 \, A_{54} + H.c. \right) \,, \end{aligned} \tag{6.4}$$

where Δ_p is the probe field detuning and atomic transition operator is defined as $A_{jk} = |j\rangle\langle k|$. An interesting insight into the involved physics can be gained by applying a further unitary transformation to the Hamiltonian

$$\begin{aligned} \bar{H}_I = &- \hbar \Delta_p (A_{22} + A_{33}) \\ &- \frac{\hbar}{2} \big(|\Omega_B| \, A_{21} + |\Omega_E| \, A_{34} + |\Omega_C| \, e^{i\Phi} A_{32} + |\Omega_1| \, A_{51} + |\Omega_2| \, A_{54} + H.c. \big) \,. \end{aligned} \tag{6.5}$$

It can be seen that H_I contains a phase contribution

$$\Phi = (\varphi_2 - \varphi_1 + \varphi_c) + (\vec{k}_2 - \vec{k}_1 + \vec{k}_C)\vec{r}\,, \tag{6.6}$$

which cannot be removed entirely via unitary transformations. The origin of this phase dependence is the closed-loop structure of the considered level scheme. Starting from $|1\rangle$, the system can evolve in a non-trivial loop sequence $|1\rangle \to |5\rangle \to |4\rangle \to |3\rangle \to |2\rangle \to |1\rangle$ back to the initial state. This enables pathway interference, e.g., from $|1\rangle$ to $|3\rangle$ either via $|5\rangle$ and $|4\rangle$, or via $|2\rangle$. The phase difference between these two interfering pathways is equivalent to the phase difference given by Eqs. (6.5) and (6.6). It is interesting to note that the closed-loop phase Φ does not contain properties of the probe field, which is due to the fact that a closed transition loop involves both an absorption and an emission of a probe field photon. Furthermore, Φ does not depend on time, because of the cancellation of the probe field and because the three control fields $\Omega_1, \Omega_2, \Omega_C$ are applied on resonance.

We are now also in the position to understand why a phase-control of light propagation is possible in chiral closed-loop media, in contrast to closed-loop media coupling only to one (electric) component of the probe field. From Fig. 6.1, it can be seen that in the presence of the probe field, a closed loop is established, such that the medium becomes sensitive to the closed-loop phase Φ. But in the absence of the probe field two transitions in the closed loop structure are undriven. It follows that parametric processes scattering the control fields into the probe field mode cannot occur, independent of the phase matching condition assumed for the wave vectors of the probe and driving fields. This crucial difference to closed-loop media coupling to one (electric) probe field component only enables the phase control of light propagation that we will find in Sec. 6.3.

In the following, we continue our analysis based on the Hamiltonian H_I in Eq. (6.4) and assume that the laser configuration satisfies the usual phase matching condition $\vec{k}_2 - \vec{k}_1 + \vec{k}_C$, such that the system dynamics only depends on the relative phase

$$\Phi_0 = \varphi_2 - \varphi_1 + \varphi_c\,. \tag{6.7}$$

6.2.3 Medium response coefficients

In zeroth order of the probe fields, the equations of motion (EOM) governing the dynamics of the atomic degrees of freedom can easily be solved. The non-vanishing density matrix elements are

$$\rho_{11}^{(0)} = \frac{|\Omega_2|^2}{|\Omega_1|^2 + |\Omega_2|^2}\,, \tag{6.8a}$$

$$\rho_{44}^{(0)} = \frac{|\Omega_1|^2}{|\Omega_1|^2 + |\Omega_2|^2}\,, \tag{6.8b}$$

$$\rho_{41}^{(0)} = -\frac{\Omega_1 \Omega_2^*}{|\Omega_1|^2 + |\Omega_2|^2}\,. \tag{6.8c}$$

The linear response to a weak probe field does not disturb this dark state prepared by Ω_1 and Ω_2, and can thus be calculated on the basis of the lowest order populations. To take into account local field effects (LFC) in a dense gas a generalized form of the Clausius-Mossotti equation [3] has been used to numerically extract χ_E, χ_H, ξ_{EH}, and ξ_{HE} from the steady state solution to linear order in the local fields E_{loc} and B_{loc} in [32]. We pursue a different strategy here which provides us with an analytic solution including dipole-dipole interactions as addressed in chapter 4. We directly replace the local fields in the EOM by the external fields E_{ext} and B_{ext} with the help of the Lorenz-Lorentz relations

$$E_{\text{loc}} = E_{\text{ext}} + \frac{1}{3\varepsilon_0}P\,, \tag{6.9a}$$

$$B_{\text{loc}} = B_{\text{ext}} + \frac{\mu_0}{3}M\,. \tag{6.9b}$$

This leads to nonlinear EOM if the polarization P and the magnetization M are expressed by microscopic expectation values of the electric and magnetic dipole density containing elements of the atomic density matrix. Since we are interested in linear response, we expand the EOM up to linear order in the probe field, and solve for the steady state. From this steady state solution, we find for the response coefficients

$$\chi_E = \frac{3L\gamma_{34}\rho_{44}^{(0)}\frac{i}{2}\Gamma_{24}}{\Gamma_{34}\Gamma_{24} + \frac{|\Omega_C|^2}{4}}\,, \tag{6.10a}$$

$$\chi_H = \frac{3L\gamma_{34}\alpha^2\rho_{11}^{(0)}\frac{i}{2}\Gamma_{31}}{\Gamma_{21}\Gamma_{31} + \frac{|\Omega_C|^2}{4}}\left(1 - \frac{\xi_{EH}|\rho_{41}^{(0)}|\,\frac{|\Omega_C|}{4}\,e^{-i\Phi_0}}{3\alpha\,\rho_{11}^{(0)}\,\frac{i}{2}\Gamma_{31}}\right), \tag{6.10b}$$

$$\xi_{EH} = \frac{3L\gamma_{34}\alpha\,|\rho_{41}^{(0)}|\,\frac{|\Omega_C|}{4}}{\Gamma_{34}\Gamma_{24} + \frac{|\Omega_C|^2}{4}}\,e^{i\Phi_0}, \tag{6.10c}$$

$$\xi_{HE} = \frac{3L\gamma_{34}\alpha\,|\rho_{41}^{(0)}|\,\frac{|\Omega_C|}{4}}{\Gamma_{21}\Gamma_{31} + \frac{|\Omega_C|^2}{4}}\left(1 + \frac{\chi_E}{3}\right)e^{-i\Phi_0}, \tag{6.10d}$$

where $L = N\lambda^3/4\pi^2$ includes the dependence on the number of particles $N\lambda^3$ per wavelength λ cubed. The decay rate and the detuning including the typical LFC shift for the electric and magnetic probe field transitions are given by

$$\Gamma_{34} = \gamma/2 + \gamma_{\text{dec}} - i(\Delta_p + \rho_{44}^{(0)}L\gamma_{34}/2)\,, \tag{6.11a}$$

$$\Gamma_{21} = \gamma_{21}/2 + \gamma_{\text{dec}} - i\Delta_p\,, \tag{6.11b}$$

where $\gamma = \gamma_{31} + \gamma_{32} + \gamma_{34}$ is the overall decay rate of state $|3\rangle$ and γ_{dec} accounts for additional decoherence induced by atomic collisions.

Interpreting the dark state of $|1\rangle$ and $|4\rangle$ as a single quantum state characterized by the coherence between the two states, both probe field transitions can be viewed as being part of a three level electromagnetically induced transparency (EIT) system [36, 37]. The electric probe field and the control field Ω_C form a Λ-system for which

$$\Gamma_{24} = \gamma_{21}/2 - i\Delta_p \tag{6.12}$$

contains the ground state decoherence and the two-photon detuning. No additional decoherence γ_{dec} besides the decay of the magnetic probe field transition has to be included if we assume that levels $|2\rangle$ and $|4\rangle$ are nearly degenerate, as then phase-perturbing collisions in the medium lead to random, but correlated phase shifts of the two states [32]. The magnetic probe field and the control field Ω_C form a ladder system in which the decoherence and two-photon detuning relevant for EIT is described by

$$\Gamma_{31} = \gamma/2 + 2\gamma_{\text{dec}} - i\Delta_p\,. \tag{6.13}$$

By inspection of the structure of the solution for χ_E and χ_H, we find that the direct electric and magnetic responses of the EIT system are amended by LFC. The electric response features the usual EIT transparency window which is only degraded by a weak ground state decoherence given by γ_{21}, the linewidth of the magnetic probe field transition. The transparency window of the direct magnetic response on the other hand is not as prominent due to strong decoherence $\gamma/2+2\gamma_{\text{dec}}$ in the ladder system. But this does not affect the propagation dynamics much since χ_H is suppressed by a factor α^2 compared to χ_E as discussed above. In particular for propagation dynamics at densities corresponding to $L \leq 1$, it can be neglected. On the contrary, the chiral cross couplings are only suppressed by a factor of α and do influence the propagation dynamics. As expected, they are proportional to $|\rho_{41}^{(0)}|$, $|\Omega_C|$, and depend on the relative closed-loop phase Φ_0. At first glance it might look like a phase dependence is also induced to χ_H by LFC because it depends on Φ_0. But a closer look reveals that this phase dependence is exactly canceled by the factor ξ_{EH}. From these solutions we expect a propagation with a reduced group velocity and with a phase dependent refractive index induced by the chiral cross couplings.

One further observation about the chirality of the medium can be made. In the sense of a macroscopic electrodynamic description, the control fields Ω_C, Ω_1, and Ω_2 are part of the medium. Thus, they change sign when the medium is inverted and lead to the expected chiral behavior of ξ_{EH} and ξ_{HE} as described in Sec. 5.2.

With the analytic solution for χ_E, χ_H, ξ_{EH}, and ξ_{HE} at hand, we can now proceed to study propagation effects in a chiral medium, focusing on control of the propagation dynamics via the closed-loop phase as concrete application.

6.3 Pulse propagation with phase control

6.3.1 Reduced group velocity

In this Section we study the propagation dynamics of a pulsed probe field in the chiral medium discussed in Sec. 6.2. Due to the direct electric response, the probe

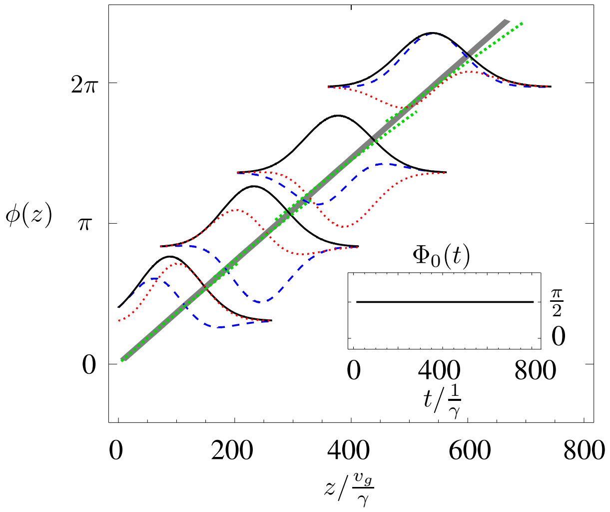

Figure 6.2: Propagation dynamics in a chiral medium. The closed-loop phase $\Phi_0 = \pi/2$ is kept constant, see inset. The absolute value (solid black lines), the real part (dashed blue lines), and the imaginary part (dotted red lines) of the probe pulse envelope are plotted for successive propagation times. Arbitrary, but consistent units are used and successive plots are vertically offset by the overall phase at the center of the pulse. The spatial phase dependence of each pulse (dashed green straight lines) is compared to the value expected from the analytical solution (thick gray straight line).

pulse propagates with a reduced group velocity, as it is the case in a usual EIT system. If we write the group velocity

$$v_g = \frac{c}{1 + n_g}, \tag{6.14}$$

the group index n_g it is given by

$$n_g = \frac{3L\omega\gamma_{34}\rho_{44}^{(0)}}{|\Omega_C|^2}. \tag{6.15}$$

This is the standard expression in a EIT system, except for the scaling by the population fraction $\rho_{44}^{(0)}$ in the ground state of the electric probe field transition. The direct magnetic response can be neglected and all additional influence of the medium on a probe pulse is due to the chiral cross coupling of the electric and magnetic probe field components.

The chiral cross coupling is mediated by the closed interaction loop and depends on the relative phase Φ_0 between the three control fields. Since the probe field propagates with strongly reduced group velocity whereas the control field Ω_C propagates at speed of light, a phase change of Φ_0 during the propagation of the probe pulse changes the frequency dependent refractive index for the probe field nearly

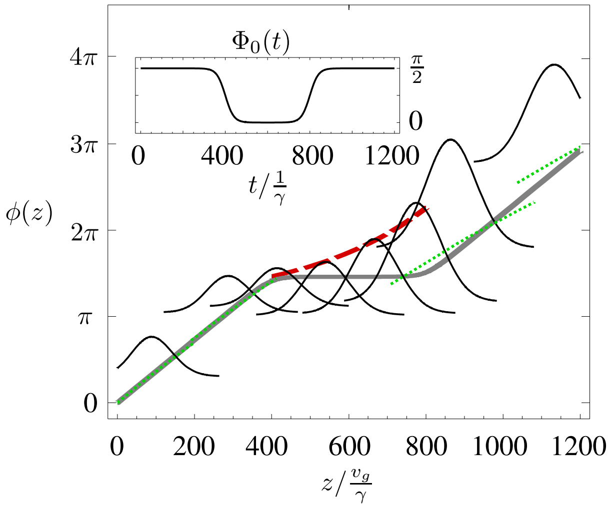

Figure 6.3: Propagation dynamics in a chiral medium with phase modulation. The closed-loop phase is switched from $\pi/2$ to zero and back to $\pi/2$ throughout the propagation, as shown in the inset. The absolute value (black solid lines) of the probe pulse envelope is plotted for successive propagation times. The scaling and offsets are used as in Fig. 6.2. At the beginning and at the end of the propagation the spatial phase dependence of each pulse (dashed green straight lines) is compared to the value expected from the analytical solution (thick gray line). During the time period of zero control phase, probe pulse envelope phase does not change and the pulse experiences gain instead, as indicated by the thick dashed red line.

instantaneously. In a similar fashion as a light pulse can be slowed down, stored, and retrieved by changing the amplitude of the control field [125], the phase of the control field can be used as a tool to control the refractive index for the probe pulse.

To clarify this idea further, in the following, we present two exemplary results from a numerical solution of the atomic EOM coupled to the wave equations for the two probe field components and the control field. We assume a medium with a density corresponding to $L = 0.01$. For $\lambda = 795\text{nm}$, this translates to $N \sim 8 \times 10^{11}\text{cm}^{-3}$. The control field strength is chosen as $|\Omega_C| = 2\gamma$, and the dark state as symmetric, $|\Omega_1| = |\Omega_2|$, such that $\rho_{11}^{(0)} = \rho_{44}^{(0)} = 0.5$ and $\rho_{41}^{(0)} = -0.5$. In both cases, we propagate a Gaussian probe pulse with a width in time of $\sigma = 50/\gamma$. Its spectrum is well contained in the EIT transparency window such that it suffers very little absorption and broadening. We use a collisional decoherence of $\gamma_{dec} = 0.5\gamma$ and for the probe field we assume left circular polarization.

6.3.2 Constant phase

In the first example, the phase Φ_0 is chosen constant as $\pi/2$. In Fig. 6.2, we show the corresponding propagation dynamics. The envelope of the electric probe field component is depicted for four successive propagation times, together with the real and imaginary part of the envelope and the pulse phase. The group velocity observed in the numerical calculation is consistent with Eqs. (6.14) and (6.15). We find that throughout the propagation, the phase of the pulse increases linearly. Thus, the real and imaginary parts of the envelope interchange while the absolute value of the envelope remains constant. This dynamics is due to a positive real index of refraction at resonance. Its theoretical value can be deduced from the solutions given in Secs. 5.3.2 and 6.2. Neglecting χ_H, the eigenvalue Eq. (5.13) reduces to

$$\eta = \frac{\Delta_p}{\omega_0} + \frac{1}{2}\left[\chi_E \mp i(\xi_{EH} - \xi_{HE})\right] \, . \tag{6.16}$$

The term linear in Δ_p arising from χ_E leads to the reduced group velocity given in Eq. (6.14). We approximate ξ_{EH} and ξ_{HE} by the constant term at resonance leading to a constant refractive index. Fourier transforming Eq. (5.12) back into time domain, we find

$$\begin{pmatrix} \Omega_E(z,t) \\ \Omega_B(z,t) \end{pmatrix} = \begin{pmatrix} \Omega_E\left(0, t - z/v_g\right) \\ \Omega_B\left(0, t - z/v_g\right) \end{pmatrix} e^{i\beta k_0 z} \, , \tag{6.17}$$

in which the polarization-dependent β is given by

$$\beta = \mp i\alpha \frac{n_g|\rho_{41}^{(0)}||\Omega_C|}{2\omega\rho_{44}^{(0)}} \left(e^{i\Phi_0} - \frac{|\Omega_C|^2 e^{-i\Phi_0}}{2\gamma_{\text{dec}}\gamma + 8\gamma_{\text{dec}}^2 + |\Omega_C|^2} \right) \, , \tag{6.18}$$

where we neglected the radiative decay of the magnetic probe field transition γ_{21} which is small compared to γ_{dec}.

Inserting the parameters chosen in Fig. 6.2, we obtain a positive real value of β such that the phase of the envelope increases constantly with propagation distance. In Fig. 6.2, we compare this phase dependence obtained from our approximate analytical model with the phase from the numerical propagation of the pulse at different propagation distances. At the center of the pulse the agreement between numerical and analytical solution is very good. Away from the center there are small deviations that increase with propagation distance. These deviations can be attributed to the neglected frequency dependence of ξ_{EH} and ξ_{HE}.

6.3.3 Phase switching

In a second example, the phase Φ_0 is changed during the propagation. Initially, it is set to $\pi/2$ as in the first example. During the course of propagation, it is switched to zero for an intermediate period of time and finally, it is switched back to $\pi/2$. The numerical results for the corresponding propagation dynamics are shown in Fig. 6.3, and the time-dependent value of the phase is shown as inset in Fig. 6.3. In the initial and final part of the propagation with phase $\pi/2$, we find the same propagation dynamics as in Fig. 6.2, with reduced group velocity v_g and with a linear increasing of the phase. But during the period with control phase switched to zero, the phase of

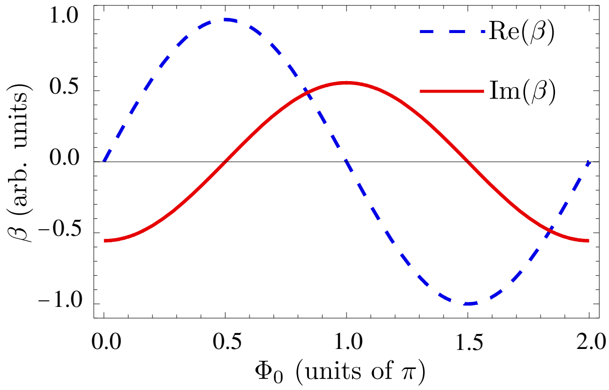

Figure 6.4: Real (dashed blue line) and imaginary (solid red line) part of β against the closed-loop phase Φ_0.

the pulse envelope remains approximately constant. Instead, its amplitude increases exponentially. As in the first example, this dynamics can be explained based on the index of refraction at resonance. Calculating β for $\Phi_0 = 0$ in the analytical solution, we find a negative imaginary value corresponding to gain. Again, we compare the analytical solution to the numerical data. The phase dependence is given by a linear increase with a plateau in between, whereas the increase in amplitude follows an exponential function, see Fig. 6.3. Both analytical solutions agree reasonably well with the numerical data, given that the finite switch period with the corresponding transient dynamics is not taken into account in the analytical calculation.

These examples show that by changing the relative control field phase Φ_0, the dynamics of the probe field can be substantially influenced throughout the propagation. In the second example, the refractive index experienced by a pulsed probe field with left circular polarization was changed from a positive real value $n \geq 1$ to an imaginary value representing gain and back. With different values for the control phase, also $n \leq 1$, absorption, or intermediate cases are possible. This is illustrated in Fig. 6.4, which depicts the real and the imaginary part of the index of refraction obtained from our analytical calculation against the control phase.

6.4 Conclusion

In summary, we discussed light propagation dynamics in a chiral atomic medium. The chirality arises from a cross coupling of the electric and the magnetic component of a probe field induced by the medium. We analytically determined the response functions for a specific chiral model system from the microscopic quantum mechanical EOM. As our main result, we demonstrated that chiral effects can crucially influence the propagation dynamics already at experimentally accessible parameter ranges. As a specific example, we showed that the chiral couplings render the medium sensitive to the relative phase of the applied fields. By changing the relative phase of one of the applied coupling fields, the propagation of a probe pulse can be controlled dynamically during its passage through the medium. From this, we concluded that chiral media are an ideal implementation of closed-loop phase control of light propagation. In a broader context, it is remarkable that the magnetic field component of the probe field can substantially modify the probe pulse propagation dynamics, despite the weak coupling of the magnetic field to the medium. It remains to be seen if such magnetic field couplings may also find other applications in quantum optics.

Conclusion

In this thesis, we have show the feasibility of the idea to realize an atomic medium with simultaneous coupling to the electric and magnetic component of a probe field. Based on the proposal of using high density and inducing chirality to obtain the necessary magnetic response, we have studied light propagation in dense and chiral media. As a key result, we have demonstrated that in a chiral medium the magnetic component of a probe field can become relevant already at low densities, accessible to current experiments.

We divided the analysis into different parts and considered several aspects of light propagation in dense and chiral media separately. In the first part, we started with aspects accessible to a single atom analysis. First, in chapter 1, we studied a closed-loop system. We calculated the medium response to a pulsed probe field and found a corresponding physical interpretation in term of scattering processes. On the one hand, this allowed us to identify the contributions linear and nonlinear in the probe field and we showed that the system can exhibit a strong intensity-dependent index of refraction with low absorption. On the other hand, the analysis gave us first insight into the processes relevant for a chiral medium induced by a closed interaction loop. More specifically, it became clear that there exist scattering processes into the probe field mode which are important for light propagation dynamics.

In chapter 2, we put forward a scheme to control the group velocity in the ultraviolet domain. The chosen level structure in mercury required an approach different from electromagnetically induced transparency (EIT) and we employed interacting dark state resonances to induce a high contrast resonance structure. Applying an additional incoherent pump field, we found that sub- and superluminal propagation as well as a negative group velocity, all without absorption can be achieved in the system. This is a starting point for applications like a controllable pulse delay line which are otherwise hard to realize in the ultraviolet domain. Moreover, the proposed scheme might be suitable to coherently store a light pulse [125]. Compared to standard light storage schemes based on EIT, it offers additional control parameters and it would be interesting to further explore these degrees of freedom in a full propagation analysis.

In the second part we extended our theoretical description by using the Maxwell-Bloch equations and considered aspects of light propagation in which a spatial dependence of the fields is important. Due to the more complex equations of motion, we augmented our analytical considerations with numerical solutions. In chapter 3, we analyzed a system in which absorption of the control fields and the generation of an additional field via four-wave mixing lead to strong propagation dynamics. We found that during propagation a closed interaction loop is established due to the newly generated field and that parametric processes typical for a closed-loop system modify the probe field. In spite of this dynamics, we were able to show that a smooth and controllable probe field response arises. To give an example, we showed that the medium is suitable for the phase-compensation mechanism in a white-light cavity which enhances the cavity bandwidth without reducing the intensity buildup. The fact that a system inherently relying on propagation dynamics can be used to prepare a medium response compatible with a given task, is supprising and calls for further attention. Based on the single atom picture in chapter 1, it seemed that in this respect parametric processes due to their rigid frequency constraints are mainly a disturbing factor. However, when one of the fields is only generated as soon as the probe field is applied, parametric processes can influence the probe field over a broader range of frequencies. In such a situation, the propagation dynamics can be advantageous for the medium response and indeed, we were able to demonstrate an additional enhancement of the cavity bandwidth in our example. The analysis also encourages one to consider a broader class of systems for light propagation in general. Here, our results are a proof of concept and also other schemes with strong propagation dynamics could benefit. For example, in nonlinear interactions where a closed-loop transition includes more than one probe field transition, a comparable mechanism could relax the frequency constraint as well.

In chapter 4, we analyzed the influence of high atomic density on light propagation. Since the densities required for a direct magnetic response different from $\mu \approx 1$ are not accessible for present experiments, we focused on a density regime at the onset of cooperative effects. In this regime, we studied the propagation dynamics of a slow light pulse in an EIT setup. We found that the phase of the pulse is strongly modulated by the dipole-dipole interactions of neighboring atoms. The phase modulation leads to a linear frequency chirp over the total extend of the pulse and is independent of the probe field intensity. This distinguishes our results from the frequency chirp obtained by self-phase modulation in a nonlinear medium. In addition, we were able to reveal the underlying physical mechanism leading to the phase modulation. We showed that dipole-dipole interactions lead to an energy transfer between neighboring atoms which follows the same principles as the interaction of the atoms with the light field. This observation gives both an explanation for the form of the phase modulation as well as an intuitive picture of dipole-dipole interactions in a dense medium in general. Intuitive insight is a necessary first step to advance light propagation into the regime of truly dense media. It should be noted that theoretical models which take into account the atom-atom interactions to all orders in the particle density do exist [27]. However, they are too complex to provide any physical insight and also a numerical treatment is not feasible in most cases. Clearly, more work needs to be done to gain an intuitive understanding of the involved physics. Besides the dipole-dipole interaction we focused on, this is also applies to quantum statistical effects or higher-order processes like multiple scattering. Here, especially radiation trapping, the enclosure of spontaneously emitted photons inside a medium due to multiple scattering, is one of the main obstacles in current experiments both with atomic vapors as well as ultracold gases. It leads to strong decoherence and prevents established optical preparation techniques to be applicable at higher density. A better understanding would guide the efforts to overcome these limitations and facilitate the way to light propagation experiments at higher density. Apart from the limitations due to radiation trapping, there are possibilities to study the effects of high density in current experiments, for example in doped crystal systems or Rydberg gases. Doped crystals can be coherently prepared by optical methods in spite of high density and in addition offer the possibility to actively enhance their coherence properties [160–162]. In Rydberg atoms the valence electron is highly excited, thus very loosely bound, and very sensitive to external electric fields. As a result, Rydberg atoms can exhibit extremely large dipole moments such that Rydberg gases are an ideal system to study dipole-dipole interactions at lower densities [163].

In the third part we addressed light propagation in chiral media. In chapter 5, we distinguished the different types of electromagnetic response and showed that a response due to an electric [magnetic] dipole moment induced by the magnetic [electric] field causes a cross coupling of the field components and renders a medium chiral. We derived the wave equations for both field components in such a medium and solved them in the slowly-varying envelope approximation. The solution is expressed in terms of general response coefficients and apart from the cross coupling no further specifications regarding the medium were made until this point. Hence, at the end of the chapter we discussed the prerequisites for an implementation.

In chapter 6, we turned to a specific example and presented a level scheme suitable to implement light propagation with chiral interactions. Applying the different concepts studied in the other chapters, we demonstrated how a closed interaction loop including both an electric and a magnetic probe field transitions can be used to implement a chiral medium. We found that the chiral cross coupling arises from a mechanism quite similar to the propagation dynamics discussed in the third chapter. Also here, the scattering processes due to the closed interaction loop can only occur as soon as the probe field is applied, but with the difference that the transition loop is closed by the other probe field component instead of a newly generated field. Therefore, the chiral interaction arises instantaneously instead of building up over the course of propagation. Based on the numerical solution of the Maxwell-Bloch equations in a chiral medium, we showed that the dynamics of a slow light pulse can be substantially influenced by the chiral interactions already at low densities. Using the closed-loop phase as a control parameter, we changed the refractive index for the light pulse from a positive real value to a negative imaginary value leading to gain and back, all during the propagation time. We were also able to derive analytic expressions for the medium response coefficients. These expressions very well describe the dynamics observed in the numerical solution and in particular made it possible to determine a parameter quantitatively characterizing the chiral interactions and its effect on the propagation dynamics in our system.

In conclusion, we have shown the feasibility of using induced chirality to realize an atomic medium with a simultaneous coupling to the electric and magnetic component of a probing light wave. We have demonstrated that in a chiral medium the necessary magnetic response can be achieved in a density regime realistic for current experiments. In contrast to using chirality, the proposal of increasing the density to a level where the direct magnetic response without chiral cross coupling is enhanced far enough to become relevant for light propagation, seems impracticable at the moment. Not only are the densities of current light propagation experiments orders of magnitude away from this regime, but also a lot of work remains to be done to improve the physical understanding of the processes relevant in a truly dense medium. Our results on dipole-dipole interactions in an EIT medium provided an intuitive picture for the density regime at the onset of cooperative effects and investigations including higher order processes are needed to test and increase the range of validity of such a picture.

Regarding the simultaneous coupling of both probe field components by induced chirality, of course an experimental verification would be highly desirable. To facilitate a practical implementation, it would be helpfull to relax the requirement of a degenerate electric and magnetic dipole transition in the optical domain. Some possible setups include replacing one electric transition with a two-photon resonance or to use a medium combining two different atomic species. In principle one could also try to use a cross coupling on a single optical transition as present in chiral molecules. As we have discussed, due to symmetry properties this is not possible for transition in free atoms. But in setups like doped crystals, the influence of the solid state host changes the symmetry properties which could make such a scheme possible. Another idea to promote the magnetic response is based on coupling a medium to both components of a single cavity mode. The standing wave inside an optical cavity gives rise to a position dependent coupling strength which is different for the electric and the magnetic field. A fixed position closed to a maximum in the intensity of the magnetic field could thus increase the magnetic coupling compared to the electric coupling. In combination with the strong feedback achievable in a high quality cavity, a simultaneous coupling to both field components could be possible.

A quantum optical experiment where both the electric and magnetic component of light are critical for the interaction with matter would certainly open a new and fascinating research perspective. The field of metamaterials has shown the power of the idea to treat both the electric and magnetic aspects on an equal footing and in quantum optics one could certainly hope for a similar boom. Apart from possible applications, a realization of such a concept would surely also be of interest from a fundamental point of view. For the first time in quantum optics, one would be able to control both aspects of light, the electric and the magnetic field, on the level of fundamental interaction processes, leading one to a vision of a *magnetic quantum optics*, i.e. a quantum optics where the interaction of light and matter rests on both facets of light.

Appendix A

Numerical algorithm

In this appendix, we describe the algorithm that has been used to obtain the numerical solution of the Maxwell-Bloch equations. It was applied to numerically calculate the light propagation dynamics that was discussed in chapters 3, 4, and 6. In particular, it is suitable to solve the Maxwell-Bloch equations in a chiral medium.

A.1 Equations of motion in dimensionless form

The Maxwell-Bloch equations combine the time evolution of the atomic degrees of freedom with a one-dimensional propagation of the electromagnetic fields. As a result, we deal with two coordinates, the time t and the position z. For the numerical treatment, we define a dimensionless time t' and position z' by

$$t' = t\gamma \quad \text{and} \quad z' = z\gamma/v\,, \tag{A.1}$$

where γ is a characteristic time scale for the atomic evolution and v is the expected propagation velocity. More specifically, for γ we used the fastest decay rate appearing in the respective level scheme and v is estimated from the analytical formula for the group velocity (see e.g. Eq. 6.14).

With this scaling the equations of motion (EOM) can be brought into a dimensionless form. The atomic degrees of freedom are governed by a master equation which reads

$$\partial_{t'}\varrho(z',t') = f(\varrho,\Omega_i)\,, \tag{A.2}$$

where ϱ is the density matrix in the interaction picture and the Ω_i denote the Rabi frequencies of the different applied fields expressed in units of γ. The function f is defined by the right-hand side (RHS) of the master equation. Its exact form depends on the respective level scheme and is not important for the algorithm.

The spatial propagation of the applied fields is described by a one-dimensional wave equation in slowly-varying envelope approximation. For each Ω_i we have an equation,

$$[\partial_{z'} + u\,\partial_{t'}]\,\Omega_i = g_i(\varrho_{mn})\,, \tag{A.3}$$

where $u = v/c$ is the expected velocity divided by the velocity of light c and the source function g_i includes the dependence on the polarization and magnetization of the medium expressed by the corresponding elements of the density matrix ϱ_{mn}. For a coupling of only the electric field component g is simply

$$g = i\kappa\varrho_d \,, \tag{A.4}$$

where $\kappa = 3\pi L v/\lambda\gamma$ is the dimensionless coupling constant, L was defined in Eq. 4.3, λ is the transition wave length, and ϱ_d is the density matrix element describing the coherence of the transition. In a chiral medium both the electric and magnetic field component couple to the polarization and magnetization of the medium. This results in two equations (see Eqs. 5.8), where the source function takes the form

$$g_E = \kappa(i\varrho_d \mp \alpha\varrho_m) \quad \text{and} \quad g_B = \kappa(i\alpha^2\varrho_m \pm \alpha\varrho_d) \,. \tag{A.5}$$

Here, ϱ_d and ϱ_m denote the coherence of the electric and magnetic probe field transition and we have assumed that the coupling strength of the magnetic transition is suppressed by a factor of the fine structure constant α. The different signs apply to a left- or right-circularly polarized probe field.

A.2 Discretization scheme

The numerical integration of the EOM (Eqs. A.2 and A.3) is performed on a two-dimensional grid with M grid points in space direction and N grid points in time direction. The value of the density matrix, and the fields at a grid point is denoted by

$$\varrho_j^k := \varrho(j\,\Delta z, k\,\Delta t) \quad \text{and} \quad \Omega_j^k := \Omega(j\,\Delta z, k\,\Delta t) \,, \tag{A.6}$$

where j and k are the indices for space and time direction, Δz and Δt are the respective stepsize, and we have simplified the description to one Rabi frequency Ω for notational clarity. In the same way, we denote the space and time dependence of the RHS of the master equation by f_j^k and of the source function in the wave equation by g_j^k.

The master equation (Eq. A.2) is evolved in time by a standard Adams-predictor formula of second order accuracy,

$$\varrho_j^{k+1} = \varrho_j^k + \frac{\Delta t}{2}\left(3f_j^k - f_j^{k-1}\right) + \mathcal{O}[\Delta t^3] \,. \tag{A.7}$$

For the first time step ($k = 1$), the values of ϱ_j^{k-1} and Ω_j^{k-1} are outside the numerical grid boundaries and we use a first order formula instead,

$$\varrho_j^2 = \varrho_j^1 + \Delta t\, f_j^1 + \mathcal{O}[\Delta t^2] \,. \tag{A.8}$$

To evolve the wave equation, we use a second order Lax-Wendroff scheme [123], modified to also include a source term [164]. First, Eq. A.3 is discretized with a leap frog method centered around the grid point $(j+1/2, k)$,

$$\frac{\Omega_{j+1}^{k} - \Omega_{j}^{k}}{\Delta z} = -u \frac{\Omega_{j+1/2}^{k+1/2} - \Omega_{j+1/2}^{k-1/2}}{\Delta t} + g_{j+1/2}^{k} \,. \tag{A.9}$$

Then, the unknown grid points $\Omega_{j+1/2}^{k-1/2}$ and $\Omega_{j+1/2}^{k+1/2}$ are calculated from a Lax scheme centered at $(j, k-1/2)$ and $(j, k+1/2)$,

$$\frac{\Omega_{j+1/2}^{k-1/2} - \frac{1}{2}(\Omega_{j}^{k-1} + \Omega_{j}^{k})}{\Delta z/2} = -u \frac{\Omega_{j}^{k} - \Omega_{j}^{k-1}}{\Delta t} + g_{j}^{k-1/2} \,, \tag{A.10a}$$

$$\frac{\Omega_{j+1/2}^{k+1/2} - \frac{1}{2}(\Omega_{j}^{k} + \Omega_{j}^{k+1})}{\Delta z/2} = -u \frac{\Omega_{j}^{k+1} - \Omega_{j}^{k}}{\Delta t} + g_{j}^{k+1/2} \,. \tag{A.10b}$$

The unknown grid points at half integer steps of the source function g in Eqs. A.9 and A.10 are replaced by the mean value of the nearest neighbors,

$$g_{j+1/2}^{k} = \frac{1}{2}(g_{j}^{k} + g_{j+1}^{k}) \,, \quad g_{j}^{k-1/2} = \frac{1}{2}(g_{j}^{k-1} + g_{j}^{k}) \,, \quad g_{j}^{k+1/2} = \frac{1}{2}(g_{j}^{k} + g_{j}^{k+1}) \,. \tag{A.11}$$

Using Eqs. A.9, A.10, and A.11, we finally arrive at the formula for a space step,

$$\begin{aligned} \Omega_{j+1}^{k} = \Omega_{j}^{k} &+ \frac{u\,\Delta z}{2\Delta t}\left[\Omega_{j}^{k-1} - \Omega_{j}^{k+1} + \frac{u\,\Delta z}{\Delta t}(\Omega_{j}^{k+1} - 2\Omega_{j}^{k} + \Omega_{j}^{k-1})\right] \\ &+ \frac{u\,\Delta z^{2}}{4\Delta t}(g_{j}^{k-1} - g_{j}^{k+1}) + \frac{\Delta z}{2}(g_{j}^{k} + g_{j+1}^{k}) \,. \end{aligned} \tag{A.12}$$

At the initial time $k = 1$, Ω_{j}^{k-1} is outside the numerical grid boundaries. To still use Eq. A.12 we replace it by the known vacuum value. At the final time $k = N$, however, Ω_{j}^{N+1} and ϱ_{j}^{N+1} are not known. Here, Eq. A.12 cannot be applied and we use a nearly identical scheme centered around $(j+1/2, N-1/2)$ to derive

$$\Omega_{j+1}^{N} = \frac{1}{1 + \frac{u\,\Delta z}{2\Delta t}}\left[\Omega_{j}^{N} + \frac{u\,\Delta z}{2\Delta t}(\Omega_{j+1}^{N-1} + \Omega_{j}^{N-1} - \Omega_{j}^{N}) + \frac{\Delta z}{2}(g_{j}^{N} - g_{j+1}^{N})\right] \,. \tag{A.13}$$

The initial state of the density matrix determines the value of ϱ_{j}^{1} for $j = 1 \ldots M$ and the time dependence of the fields at the medium entrance fixes Ω_{1}^{k} for $k = 1 \ldots N$. Based on these initial conditions, the value of ϱ and Ω is iteratively calculated at all other grid points. First, Eq. A.7 is used to calculate ϱ_{1}^{k} for $k = 2 \ldots M$. Then, Eq. A.12 is used to calculate Ω_{2}^{1}. Before Ω_{2}^{2} can be calculated, we have to use Eq. A.7 again to calculate ϱ_{2}^{2} which is necessary for the source function g_{2}^{2}. In this manner, Eqs A.12 and A.7 are used in alternation until the last space step at $k = N$ is performed by Eq. A.13. Repeating this procedure iteratively for $j = 3 \ldots M$, finally yields the solution for ϱ and Ω at all other grid points.

Bibliography

[1] J. C. Maxwell, *A Dynamical Theory of the Electromagnetic Field* (Philosophical Transactions of the Royal Society of London **155**, p. 459-512, 1864).

[2] H. R. Hertz, *Ueber die Beziehungen zwischen Licht und Elektricität* (Lecture at 62. Versammlung deutscher Naturforscher und Ärzte, Heidelberg 1889, published by E. Strauß, 1890).

[3] J. D. Jackson, *Classical Electrodynamics* 3rd ed. (Wiley, New York, 1998).

[4] M. O. Scully and M. S. Zubairy, *Quantum Optics* (Cambridge University Press, Cambridge, 1997).

[5] R. Loudon, *The Quantum Theory of Light* 3rd ed. (Oxford University Press, Oxford, 2000).

[6] V. G. Veselago, Sov. Phys. Usp. **10**, 509 (1968).

[7] J. B. Pendry, Phys. Rev. Lett. **85**, 3966 (2000).

[8] D. R. Smith, D. Schurig, M. Rosenbluth, S. Schultz, S. A. Ramakrishna, and J. B. Pendry, Appl. Phys. Lett. **82**, 1506 (2003).

[9] R. Merlin, Appl. Phys. Lett. **84**, 1290 (2004).

[10] V. A. Podolskiy and E. E. Narimanov, Opt. Lett. **30**, 75 (2005).

[11] J. B. Pendry, D. Schurig, and D. R. Smith Science **312**, 1780 (2006).

[12] U. Leonhardt, Science **312**, 1777 (2006).

[13] J. B. Pendry, A. J. Holden, D. J. Robbins, W. J. Stewart, IEEE Trans. Microwave Theory Tech. **47**, 2075 (1999)

[14] D. R. Smith, W. J. Padilla, D. C. Vier, S. C. Nemat-Nasser, and S. Schultz, Phys. Rev. Lett. **84**, 4184 (2000).

[15] R. A. Shelby, D. R. Smith, and S. Schultz, Science **292**, 77 (2001).

[16] T. J. Yen, W. J. Padilla, N. Fang, D. C. Vier, D. R. Smith, J. B. Pendry, D. N. Basov,and X. Zhang, Science **303**, 1494 (2004).

[17] S. Linden, C. Enkrich, M. Wegener, J. F. Zhou, T. Koschny, and C. M. Soukoulis, Science **306** 1351 (2004).

[18] C. Enkrich, M. Wegener, S. Linden, S. Burger, L. Zschiedrich, F. Schmidt, J. F. Zhou, T. Koschny, and C. M. Soukoulis, Phys. Rev. Lett. **95**, 203901 (2005).

[19] V. G. Veselago and E. E. Narimanov Nature Materials **5**, 759 (2006).

[20] H. J. Lezec, J. A. Dionne, and H. A. Atwater, Science **316**, 430 (2007).

[21] M. Ö. Oktel and Ö. E. Müstecaplıoğlu, Phys. Rev. A **70**, 053806 (2004).

[22] Q. Thommen and P. Mandel, Phys. Rev. Lett. **96**, 053601 (2006).

[23] S. E. Harris, Phys. Today **50**, 36 (1997).

[24] M. Fleischhauer, A. Imamoglu, and J. P. Marangos, Rev. Mod. Phys **77**, 633 (2005).

[25] W. Demtröder, *Laser Spectroscopy: Basics Concepts and Instrumentation* (Springer, Berlin, 1996).

[26] R. W. Boyed, *Nonlinear Optics* (Academic Press Limited, London, 1992).

[27] J. Ruostekoski and J. Javanainen, Phys. Rev. A **55**, 513 (1997).

[28] R. H. Dicke, Phys. Rev. **93**, 99 (1954).

[29] T. Hollstein, Phys. Rev. 72, 1212 (1947).

[30] J. B. Pendry, Science **306**, 1353 (2004).

[31] C. Monzon and D. W. Forester, Phys. Rev. Lett. **95**, 123904 (2005).

[32] J. Kästel, M. Fleischhauer, S. F. Yelin, and R. L. Walsworth, Phys. Rev. Lett. **99**, 073602 (2007).

[33] P. P. Orth, J. Evers, and C. H. Keitel, arXiv:0711.0303 (2008).

[34] E. Hecht, *Optics* (3rd Ed., Addison-Wesley, 1998).

[35] D. P. Craig and T. Thirunamachandran, *Molecular Quantum Electrodynamics* (Dover Publications, Mineola, 1998).

[36] S. J. Buckle, S. M. Barnett, P. L. Knight, M. A. Lauder, and D. T. Pegg, Opt. Acta **33**, 1129 (1986).

[37] D. V. Kosachiov, B. G. Matisov, and Y. V. Rozhdestvensky, J. Phys. B **25**, 2473 (1992).

[38] B. Jungnitsch and J. Evers, Phys. Rev. A **78**, 043817 (2008).

[39] H. Haken and H. C. Wolf, *The Physics of Atoms and Quanta* (Springer, 7th ed., Berlin, 2005).

[40] Y. Ralchenko, A. E. Kramida, J. Reader, and NIST ASD Team, *NIST Atomic Spectra Database*, (version 3.1.5, http://physics.nist.gov/asd3, 2008).

[41] G. Alzetta, A. Gozzini, L. Moi, and G. Orriols, Nuovo Cimento B **36**, 5 (1976).

[42] E. Arimondo, in: *Progress in Optics XXXV*, edited by E. Wolf (Elsevier, Amsterdam, p. 257, 1996).

[43] O. Kocharovskaya, Phys. Rep. **219**, 175 (1992).

[44] Z. Ficek and S. Swain, *Quantum coherence and interference: Theory and Experiments* (Springer, Berlin 2005).

[45] W. E. van der Veer, R. J. J. van Diest, A. Donszelmann, and H. B. van Linden van den Heuvell, Phys. Rev. Lett. **70**, 3243 (1993).

[46] W. Maichen, F. Renzoni, I. Mazets, E. Korsunsky, and L. Windholz, Phys. Rev. A **53**, 3444 (1996).

[47] S. A. Babin, S. I. Kablukov, U. Hinze, E. Tiemann and B. Wellegehausen, Opt. Lett. **26**, 81 (2001).

[48] E. A. Korsunsky and D. V. Kosachiov, Phys. Rev. A **60**, 4996 (1999).

[49] A. J. Merriam, S. J. Sharpe, M. Shverdin, D. Manuszak, G. Y. Yin, and S. E. Harris, Phys. Rev. Lett. **84**, 5308 (2000).

[50] G. Morigi, S. Franke-Arnold, and G. L. Oppo, Phys. Rev. A **66**, 053409 (2002).

[51] V. S. Malinovsky and I. R. Sola, Phys. Rev. Lett. **93**, 190502 (2004).

[52] M. Mahmoudi and J. Evers, Phys. Rev. A. **74**, 063827 (2006).

[53] S. Kajari-Schröder, G. Morigi, S. Franke-Arnold, and G. L. Oppo, Phys. Rev. A **75**, 013816 (2007).

[54] A. F. Huss, R. Lammegger, C. Neureiter, E. A. Korsunsky, and L. Windholz, Phys. Rev. Lett. **93**, 223601 (2004).

[55] H. Shpaisman, A. D. Wilson-Gordon, and H. Friedmann, Phys. Rev. A **71**, 043812 (2005).

[56] S. E. Harris, J. E. Field, and A. Imamoglu, Phys. Rev. Lett. **64**, 1107 (1990).

[57] P. R. Hemmer, D. P. Katz, J. Donoghue, M. Cronin-Golomb, M. S. Shariar, and P. Kumar, Opt. Lett. **20**, 769 (1995).

[58] D. A. Braje, V. Balic, S. Goda, G. Y. Yin, and S. E. Harris, Phys. Rev. Lett. **93**, 183601 (2004).

[59] M. D. Lukin, P. R. Hemmer, and M. O. Scully, Adv. At. Mol. Opt. Phys. **42**, 347 (2000).

[60] J. E. Bjorkholm and A. A. Ashkin, Phys. Rev. Lett. **32**, p129 (1974).

[61] H. Friedmann and A. D. Wilson-Gordon, Phys. Rev. A **52**, 4070 (1995).

[62] A. B. Matsko, I. Novikova, G. R. Welch, and M. S. Zubairy, Opt. Lett. **28**, 96 (2003).

[63] H. Schmidt and A. Imamoglu, Opt. Lett. **21**, 1936 (1996).

[64] S. E. Harris and L. V. Hau, Phys. Rev. Lett. 82, 4611 (1999).

[65] T. Nakajima, Opt. Lett. **25**, 847 (2000).

[66] Y. P. Niu and S. Q. Gong, Phys. Rev. A **73**, 053811 (2006).

[67] T. N. Dey and G. S. Agarwal, Phys. Rev. A **76**, 015802 (2007).

[68] R. H. Dicke, Phys. Rev. **89**, 472 (1953).

[69] D. A. Steck, *Sodium D Line Data* (Los Alamos, 2000/2003).

[70] A. Sommerfeld, Z. Phys. **8**, 841 (1907).

[71] L. Brillouin, *Wave propagation and group velocity* (Academic Press, New York 1960).

[72] S. E. Harris, J. E. Field, and A. Kasapi, Phys. Rev. A **46**, R29 (1992).

[73] A. Kasapi, M. Jain, G. Y. Yin, and S. E. Harris, Phys. Rev. Lett. **74**, 2447 (1995).

[74] O. Schmidt, R. Wynands, Z. Hussein, and D. Meschede, Phys. Rev. A **53**, R27 (1996).

[75] G. Müller, A. Wicht, R. Rinkleff, and K. Danzmann, Opt. Commun. **127**, 37 (1996).

[76] J. E. Field, H. Hahn, S. E. and Harris, Phys. Rev. Lett. **67**, 3062 (1991).

[77] M. Xiao, Y. Q. Li, S. Z. Jin, and J. Gea-Banacloche, Phys. Rev. Lett. **74**, 666 (1995).

[78] D. Budker, D. F. Kimball, S. M. Rochester, and V. V. Yashchuk, Phys. Rev. Lett. **83**, 1767 (1999).

[79] G. S. Agarwal and T. N. Dey, Phys. Rev. Lett. **92**, 203901 (2004).

[80] A. E. Patnaik, F. L. Kien, and K. Hakuta, Phys. Rev. A **69**, 035803 (2004).

[81] L. V. Hau, S. E. Harris, Z. Dutton, and C. H. Behroozi, Nature (London) **394**, 594 (1999).

[82] M. M. Kash, V. A. Sautenkov, A. S. Zihrov, L. Hollberg, G. R. Welch, M. D. Lukin, Y. Rostovtsev, E. S. Fry, and M. O. Scully, Phys. Rev. Lett. **82**, 5229 (1999).

[83] S. B. Ham, P. R. Hemmer, and M. S. Shahriar, Opt. Commun. **144**, 227 (1997).

[84] A. M. Steinberg and R. Y. Chiao, Phys. Rev A **49**, 2071 (1994).

[85] E. L. Bolda, J. C. Garrison, and R. Y. Chiao, Phys. Rev. A **48**, 2938 (1994)

[86] A. M. Akulshin, A. Cimmino, A. I. Sidorov, P. Hannaford, and G. I. Opat, Phys Rev A **67**, 011801(R) (2003).

[87] M. Bigelow, N. Lepeshkin, and R. Boyd, Science **301**, 200 (2003).

[88] E. E. Mikhailov, V. A. Sautenkov, I. Novikova, and G. R. Welch, Phys. Rev. A **69**, 063808 (2004).

[89] C. Goren, A. D. Wilson-Gordon, M. Rosenbluh, and H. Friedmann, Phys. Rev. A **68**, 043818 (2003).

[90] G. S. Agarwal, T. N. Dey, and S. Menon, Phys. Rev. A **64**, 053809 (2001).

[91] D. Han, H. Guo, Y. Bai, and H. Sun, Phys. Lett. A **334**, 243 (2005).

[92] H. Tajalli, and M. Sahrai, J. Opt. B: Quantum Semiclassical Opt. **7**, 168 (2005).

[93] D. Bortman-Arbiv, A. D. Wilson-Gordon, and H. Friedmann, Phys. Rev. A **63**, 043818 (2001).

[94] L. J. Wang, A. Kuzmich, and A. Dogariu, Nature (London) **406**, 277 (2000).

[95] A. Kuzmich, A. Dogariu, L. J. Wang, P. M. Millonni, and R. Y. Chiao, Phys. Rev. Lett. **86**, 3929 (2001).

[96] J. Zhang, G. Hernandez, and Y. Zhu, Opt. Lett. **31**, 2598 (2006).

[97] C. Affolderbach, S. Knappe, R. Wynands, A. V. Taichenachev, and V. I. Yudin, Phys. Rev. A **65**, 043810 (2002).

[98] A. M. Akulshin, S. Barreiro, and A. Lezama, Physical Review A **57**, 2996 (1998).

[99] M. Mahmoudi, M. Sahrai, and H. Tajalli, J. Phys. B **39**, 1825 (2006).

[100] M. Mahmoudi, M. Sahrai, and H. Tajalli, Phys. Lett. A **357**, 66 (2006).

[101] R. Y. Chiao and A. M. Steinberg, in: *Progress in Optics XXXVII*, ed. E. Wolf (Elsevier, Amsterdam, p. 345, 1997).

[102] M. Stenner, D. Gauthier, and M. Neifeld, Nature (London) **425**, 695 (2003).

[103] K. Kim, H. S. Moon, C. Lee, S. K. Kin, and J. B. Kin, Phys. Rev. A **68**, 013810 (2003).

[104] M. D. Lukin, S. F. Yelin, M. Fleischhauer, and M. O. Scully, Phys. Rev. A **60**, 3225 (1999).

[105] E. S. Fry, M. D. Lukin, T. Walther, and G. R. Welch, Opt. Commun. **179**, 499 (2000).

[106] A. N. Nesmeyanov, *Vapor Pressure of the Chemical Elements* (Elsevier, Amsterdam, 1963).

[107] Y. C. Chen, Y. A. Liao, H. Y. Chiu, J. J. Su, and I. A. Yu, Phys. Rev. A **64**, 053806 (2001).

[108] X. G. Wei, J. H. Wu, H. H. Wang, A. Li, Z. H. Kang, Y. Jiang, and J. Y. Gao, Europhys. Lett. **78**, 44002 (2007).

[109] M. Yan, E. G. Rickey, and Y. Zhu, Phys. Rev. A **64**, 013412 (2001).

[110] B. E. A. Saleh and M. C. Teich, *Fundamentals of Photonics* (Wiley, New York, 1991).

[111] P. Aufmuth and K. Danzmann, New J. Phys. **7**, 202 (2005).

[112] A. Wicht, K. Danzmann, M. Fleischhauer, M. Scully, G. Müller, and R. H. Rinkleff, Opt. Commun. **134**, 431 (1997).

[113] S. Wise, G. Müller, D. Reitze, D. B. Tanner, and B. F. Whiting, Classical Quantum Gravity **21**, S1031 (2004).

[114] S. Wise, V. Quetschke, A. J. Deshpande, G. Mueller, D. H. Reitze, D. B. Tanner, B. F. Whiting, Y. Chen, A. Tünnermann, E. Kley, and T. Clausnitzer Phys. Rev. Lett. **95**, 013901 (2005).

[115] R. H. Rinkleff and A. Wicht, Phys. Scr. T **118**, 85 (2005).

[116] A. Dogariu, A. Kuzmich, and L. J. Wang, Phys. Rev. A **63**, 053806 (2001).

[117] G. S. Pati, M. Salit, K. Salit, and M. S. Shahriar, Phys. Rev. Lett. **99**, 133601 (2007).

[118] H. Wu and M. Xiao, Phys. Rev. A **77**, 031801 (R) (2008).

[119] A. A. Savchenkov, A. B. Matsko, and L. Maleki, Opt. Lett. **31**, 92 (2006).

[120] M. Jain, H. Xia, G. Y. Yin, A. J. Merriam, and S. E. Harris, Phys. Rev. Lett. **77**, 4326 (1996).

[121] S. Babin, U. Hinze, E. Tiemann, and B. Wellegehausen, Opt. Lett. **21**, 1186 (1996).

[122] B. Lü, W.H. Burkett, and M. Xiao, Opt. Lett. **23**, 804 (1998).

[123] W. H. Press, B. P. Flannery, S. A. Teukolsky, and W. T. Vetterling, *Numerical Recipes* (Cambridge University Press, Cambridge, 1992).

[124] P. W. Milonni, *Fast Light, Slow Light and Left-Handed Light* (Institute of Physics, 2005).

[125] C. Liu, Z. Dutton, C. H. Behroozi, and L. V. Hau, Nature (London) **409**, 490 (2001).

[126] D. A. Braje, V. Balic, G. Y. Yin, and S. E. Harris, Phys. Rev. A **68**, 041801(R) (2003).

[127] S. Barreiro and J. W. R. Tabosa, Phys. Rev. Lett. **90**, 133001 (2003).

[128] H. Kang and Y. Zhu, Phys. Rev. Lett. **91**, 093601 (2003).

[129] C. W. Chou, S. V. Polyakov, A. Kuzmich, and H. J. Kimble, Phys. Rev. Lett. **92**, 213601 (2004).

[130] D. N. Matsukevich, A. Kuzmich, Science **306**, 663 (2004).

[131] T. Chanelière, D. N. Matsukevich, S. D. Jenkins, S. Y. Lan, T. A. B. Kennedy, and A. Kuzmich, Nature (London) **438**, 833 (2005).

[132] A. T. Black, J. K. Thompson, V. Vuletić, Phys. Rev. Lett. **95**, 133601 (2005).

[133] D. N. Matsukevich, T. Chanelière, S. D. Jenkins, S.-Y. Lan, T. A. B. Kennedy, and A. Kuzmich, Phys. Rev. Lett. **96**, 033601 (2006).

[134] J. K. Thompson, J. Simon, H. Loh, V. Vuletić, Science **313**, 74 (2006).

[135] S. Chen, Y. Chen, B. Zhao, Z. Yuan, J. Schmiedmayer, J. Pan, Phys. Rev. Lett. **99**, 180505 (2007).

[136] K. S. Choi, H. Deng, J. Laurat, H. J. Kimble, Nature (London) **452**, 67 (2008).

[137] R. Newell, J. Sebby, and T. G. Walker, Opt. Lett. **28**, 1266 (2003).

[138] J. Sebby-Strabley, R. T. R. Newell, J. O. Day, E. Brekke, and T. G. Walker, Phys. Rev. A **71**, 021401(R) (2005).

[139] M. Fattori, C. D'Errico, G. Roati, M. Zaccanti, M. Jona-Lasinio, M. Modugno, M. Inguscio, and G. Modugno, Phys. Rev. Lett. **100**, 080405 (2008).

[140] M. Fleischhauer and S. F. Yelin, Phys. Rev. A **59** 2427 (1999).

[141] G. Morigi and G. S. Agarwal, Phys. Rev. A **62**, 013801 (2000).

[142] O. Morice, Y. Castin, J. Dalibard, Phys. Rev. A **51**, 3896 (1995).

[143] M. Born and E. Wolf, *Principles of Optics* (Mac Millam, New York, 1964).

[144] M. Fleischhauer, Opt. Exp. Vol. **4**, 107 (1999).

[145] A. B. Matsko, I. Novikova, M. O. Scully, and G. R. Welch, Phys. Rev. Lett. **87**, 133601 (2001).

[146] G. Labeyrie, R. Kaiser, and D. Delande, Appl. Phys. B **81**, 1001 (2005).

[147] I. M. Sokolov, M. D. Kupriyanova, and D. V. Kupriyanov, Phys. Rev. A **79**, 053405 (2009).

[148] C. M. Bowden and J. P. Dowling, Phys. Rev. A **47**, 1247 (1993).

[149] C. R. Stroud, Jr., C. M. Bowden, and L. Allen, Opt. Commun. **67**, 387 (1988).

[150] I. V. Jyotsna and G. S. Agarwal, Phys. Rev. A **53**, 1690 (1996).

[151] J. P. Dowling and C. M. Bowden, Phys. Rev. Lett. **70**, 1421 (1993).

[152] J. Q. Shen and S. He, Ann. Phys. **16**, 364 (2007).

[153] H. Li, T.S. Varzhapetyan, V.A. Sautenkov, Y.V. Rostovtsev, H. Chen, D. Sarkisyan and M.O. Scully, Appl. Phys. B **91**, 229 (2008).

[154] N. Wang and H. Rabitz, Phys. Rev. A **51**, 5029 (1995).

[155] J. Tidström, P. Jänes, and L. M. Andersson, Phys. Rev. A **75**, 053803 (2007).

[156] A. V. Gorshkov, A. Andre, M. Fleischhauer, A. S. Sorensen, and M. D. Lukin, Phys. Rev. Lett. **98**, 123601 (2007).

[157] V. A. Sautenkov, Y. V. Rostovtsev, H. Chen, P. Hsu, G. S. Agarwal, and M. O. Scully, Phys. Rev. Lett. **94**, 233601 (2005).

[158] A. J. Flikweert, T. Nimalasuriya, C. H. J. M. Groothuis, G. M. W. Kroesen, and W. W. Stoffels, J. Appl. Phys. **98**, 073301 (2005).

[159] P. P. Orth, *Losless negative refraction in dense atomic gases*, Master thesis (University of Heidelberg, 2007).

[160] E. Fraval, M.J. Sellars, and J.J. Longdell, Phys. Rev. Lett. **92**, 077601 (2004).

[161] E. Fraval, M.J. Sellars, and J.J. Longdell, Phys. Rev. Lett. **95**, 030506 (2005).

[162] J. J. Longdell, E. Fraval, M. J. Sellars, and N. B. Manson Phys. Rev. Lett. **95**, 063601 (2005).

[163] T. F. Gallagher, *Rydberg Atoms* (Cambridge University Press, Cambridge, 1994).

[164] K. R. Hansen, *Standing Wave Electromagnetically Induced Transparency*, Master thesis (University of Aarhus, 2006).

Danksagung

Nach nunmehr fast drei Jahren, die ich als Doktorand am Max-Planck-Institut für Kernphysik in Heidelberg verbracht habe, habe möchte ich mich bei allen bedanken, die mich in dieser Zeit unterstützt haben und zum Gelingen dieser Doktorarbeit beigetragen haben.

Mein erster Dank gilt Prof. C. H. Keitel für die Aufnahme in seine Arbeitsgruppe und für die guten Rahmenbedingungen die er für die Forschungsarbeit schafft.

Ganz besonderen Dank verdient meinem Betreuer PD Dr. J. Evers. Zum einen für die Vergabe des Forschungsthemas, und das Vertrauen, das er in mich gesetzt hat, als er mich als Doktorand an nahm. Zum anderen für die stete Unterstützung meiner Forschungsarbeit, die vielen Dinge, die ich von ihm gelernt habe, seine unmittelbare Erreichbarkeit bei großen und kleinen Anliegen, seine pragmatische Art, mit der er mich durch die Unwägbarkeiten des wissenschaftlichen Publizierens lotste und für den Ansporn und die Hilfe, die er mir bis zum Schluss gegeben hat und ohne die diese Arbeit sicher nicht so weit gekommen wäre.

Ganz herzlich möchte ich mich bei Prof. M. Weidemüller für die Übernahme des Zweitgutachtens bedanken.

Die Gelegenheit zum wissenschaftlichen Austausch war mir sehr wichtig und hat mir oft neue Perspektiven und Inspirationen ermöglicht. Deshalb möchte ich mich dafür bedanken, das ich durch die Teilnahme an mehreren Konferenzen und Doktorandenschulen oft die Möglichkeit dazu hatte.

Ein Highlight der Doktorandenzeit war sicher mein dreimonatiger Forschungsaufenthalt an der der University of Auckland. Hier möchte ich mich besonders bei PD Dr. J. Evers und Prof. C. H. Keitel für die persöhnliche Unterstützung und die Finanzierung im Rahmen der Heidelberg Graduate School of Fundamental Physics sowie der International Max Planck Research School for Quantum Dynamics bedanken. Dank gilt weiterhin Prof. H. Carmichael und A. Prof. S. Parkins für die nette Aufnahme in ihre Arbeitgruppe in Auckland, die gute Betreuung vor Ort und ihre finanzielle Beihilfe.

Bei A. Prof. T. Dey möchte ich mich für die gute Zusammenarbeit während seiner mehrmaligen Gastaufenthalte in Heidelberg bedanken. Unser gemeinsames Forschungsprojekt hat mir viel Freude gemacht. Thank you very much, Tarak, for the good collaboration during your visits in Heidelberg and in between. I really enjoyed our joint research project and it was a pleasure to work with you!

Bedanken möchte ich mich auch bei Juniorprof. S. Jochim, der meine Theoretikerfragen an Experimentalphysiker immer Ernst genommen hat und auch bei seiner Arbeitsgruppe, die mir während der ein oder anderen Partie Tischfußball in der Mittagspause interessante Einblicke in Experimente mit ultrakalten Gasen geben konnte.

Meinen BürokollegInnen Sandra Schmid und Varun Kapoor haben mit ihrer Rücksichtsvolle Art immer eine angenehme und konzentrierte Arbeitsatmosphäre ermöglicht. Vielen Dank dafür.

Zum Schluss möchte ich mich bei allen Kollegen und Freunden der letzten drei Jahre für die gemeinsame Zeit bedanken. Besonders mit Peter Orth und Ben King habe

ich, neben dem Go-Spiel, sowohl in Heidelberg als auch über die Distanz interessante Diskussionen über die Wissenschaft und das Leben im Allgemeinen geteilt.
Mein ganz persöhnlicher Dank gilt meinen Eltern und meinen Geschwister, die immer für mich da sind und mich in jeder Phase dieser Arbeit bestärkt haben.

Heidelberg im August 2009,

Robert Fleischhaker